Dissertation

submitted to the

Combined Faculties for the Natural Sciences and for Mathematics

of the Ruperto-Carola University of Heidelberg, Germany

for the degree of

Doctor of Natural Sciences

presented by

Diplom-Biologist Jana Maurer

born in: Lahr/Schwarzwald

Oral-examination: 04.12.2017

VEGFD Downregulation in Hippocampal Area CA1: Effects on Dendritic Morphology of Pyramidal Neurons and Network Activity

Referees:	Prof. Dr. Andreas Draguhn
	Prof. Dr. Hilmar Bading

Declarations according to §8 (3) c) and d) of the doctoral degree regulations:

c) I hereby declare that I have written the submitted dissertation myself and in this process have used no other sources or materials than those explicitly indicated.

d) I hereby declare that I have not applied to be examined at any other institution, nor have I used the dissertation in this or any other form at any other institution as an examination paper, nor submitted it to any other faculty as a dissertation.

Heidelberg, 05.10.2017

Jana Maurer

Contents

Abstract I

Zusammenfassung III

Abbrevations V

List of Figures VII

Contribution of others IX

1 Introduction 1

- 1.1 The Hippocampal Formation and its Proposed Functions 1
  - 1.1.1 The Hippocampal Architecture and Circuitry 2
  - 1.1.2 Pyramidal Cells within the Layers of CA1 4
- 1.2 Influence of VEGFD on Dendritic Morphology and Long-Term Memory 7
- 1.3 Hippocampal Network Oscillations 9
  - 1.3.1 Theta Oscillations 10
  - 1.3.2 Gamma Oscillations 12
  - 1.3.3 Cross-Frequency Coupling of Theta and Gamma 13
  - 1.3.4 Sharp Wave Ripples 14
- 1.4 Aims of this Study 16

2 Materials and Methods 17

- 2.1 Animal Ethical Approval and Housing 17
- 2.2 Plasmids and Recombinant Adeno-Associated Viruses 17
- 2.3 Chemicals and Solutions 18
- 2.4 Animal Surgery 19
  - 2.4.1 Stereotaxic Virus Injection 20
  - 2.4.2 Chronic Implantation of Electrodes 20
- 2.5 In vitro Patch Clamp Recordings 21
  - 2.5.1 Acute Hippocampal Slice Preparation 21
  - 2.5.2 Patch Clamp 21
- 2.6 In vivo Recordings of Local Field Potentials and Evoked Potentials 23
  - 2.6.1 Head-Fixed Experiments in Awake Animals 23
  - 2.6.2 Recordings in Freely Moving Animals 24
- 2.7 Stainings and Microscopy 24
  - 2.7.1 Fluorescence Staining and Spine Imaging 24
  - 2.7.2 DAB Staining and Neuron Reconstruction 24
  - 2.7.3 Histology for Verification of in vivo Electrode Position 25

2.8 Data Analysis 27
2.8.1 Morphometric Analysis of Dendrites 27
2.8.2 Morphometric Analysis of Dendritic Spines 29
2.8.3 In vitro Patch Clamp Recordings 30
2.8.4 In vivo Recordings 31
2.9 Statistics 34
3 Results 35
3.1 Morphometric Data and Single Cell Recordings 35
3.1.1 Changes in Dendritic Geometry following VEGFD Knockdown 35
3.1.2 Spine Density after VEGFD Downregulation 37
3.1.3 Passive and Active Functional Single Cell Properties in vitro Following VEGFD Knockdown 39
3.2 Recordings of Network Oscillations in vivo 42
3.2.1 LFP and CSD Depth Profiles of Theta and Gamma Oscillations in VEGFD Knockdown Mice in vivo 43
3.2.2 Measurements of Theta and Gamma Oscillatory Strength in VEGFD Knockdown Mice in vivo 48
3.2.3 Cross-Frequency Coupling of Theta and Gamma Oscillations in VEGFD Knockdown Mice in vivo 52
3.2.4 Sharp Wave-Ripple Analysis in VEGFD Knockdown Mice in vivo 57
3.2.5 Current Source Density Analysis of Evoked Potentials in VEGFD Knockdown Mice in vivo 61
4 Discussion 64
4.1 Morphological Changes of Apical and Basal Dendrites in CA1 Pyramidal Cells after VEGFD Downregulation 65
4.2 No Implications of VEGFD Knockdown on Spine Density 68
4.3 Functional Effects of VEGFD Knockdown at the Cellular Level 69
4.4 Functional Effects of VEGFD Knockdown on Network Oscillations 71
4.5 Outlook 75
Acknowledgements 77
References 79

Abstract

Neurons constitute the cellular basis of the nervous system and their activity generates most functions of the brain. Although, neurons exhibit highly diverse structures, their morphology comprises three main functional compartments. Dendrites are ramified structures and the major input side of neurons. Different input signals converge at the soma in order to generate action potentials. This output is transmitted through the axon to other neurons, thus creating complex neuronal networks. The morphology of dendritic arbors has a high impact on the connectivity and the electrical properties of neurons, determining input signals and their transmission and integration. It is therefore of great importance to study the link between dendritic morphology, electrical properties of single neurons and functions on the network level. By studying neurodegenerative diseases, it becomes clear that particularly the maintenance of the neuronal morphology is crucial for proper cognitive performance. Previous studies demonstrated that the growth factor VEGFD regulates the maintenance of the dendritic length in cultured neurons and of basal dendrites in the mouse hippocampus. Furthermore, VEGFD deficient mice show a long-term memory deficit, suggesting a link between altered dendritic morphology and cognitive function deficits. In this study, the regulatory effect of VEGFD on the branching of distinct dendritic compartments and the functional consequences of VEGFD loss both on a single cell level and on the level of network oscillations were investigated.

Following the suppression of VEGFD in CA1 pyramidal neurons *in vivo*, detailed morphometric analyses, including basal and apical dendrites as well as spine density, confirmed that basal dendrites loose length and overall complexity. Interestingly, the apical dendrites increased in length and size. This elongation occurred in areas with a high density of synaptic inputs. The spine density in all areas remained unaltered, indicating a shift in input ratio between longer apical and smaller basal dendritic trees. Furthermore, the functional consequences of VEGFD loss on single cell level and on network oscillations were investigated. Single cell patch clamp recordings revealed no changes in passive membrane properties and action potential firing properties, apart from an increased input resistance. The *in vivo* electrical stimulation of two distinct input pathways to CA1 revealed no alterations in the synaptic input strength. The comparison of several network oscillations between knockdown mice and control animals revealed no differences. These surprising results indicate that changed dendritic morphology due to the loss of VEGFD has no impact on network oscillations, such as theta, gamma and SPW R, in different behavioral states like running, immobility and sleep.

In conclusion, these findings show that the morphology of the dendritic tree is modulated by VEGFD. Interestingly, functional analysis at the cellular level revealed only minimal changes, and network-level analysis revealed no significant changes. The general stability of the size of the dendritic tree (basal + apical) and the unaltered electrical signatures suggest a homeostatic mechanism to compensate alterations in dendritic geometry *in vivo*. This emphasizes the importance of network stabilization in the adult mouse hippocampal network.

Zusammenfassung

Neurone sind die zelluläre Basis des Nervensystems und ihre physiologischen Eigenschaften liegen vielen Funktionen des Gehirns zugrunde. Der Aufbau von Neuronen ist sehr vielfältig, allerdings weisen sie drei gemeinsame Hauptkomponenten auf. Dendriten sind verzweigte Strukturen welche die Eingangssignale empfangen. Diese konvergieren im Zellkörper und generieren im Axonhügel einen digitalen Output in Form von Aktionspotentialen. Diese Ausgangssignale werden dann über das Axon an anderen Neurone übertragen. Dadurch bildet sich ein komplexes neuronales Netzwerk. Die Morphologie der Dendriten hat einen großen Einfluss auf die Verbindungen und die elektrischen Eigenschaften von Neuronen und daher auch auf die Eingangssignale, sowie deren Weiterleitung und Integrierung. Deshalb ist die Verknüpfung zwischen Dendritenmorphologie, elektrischen Eigenschaften von Einzelzellen und die Funktion auf Netzwerkebene wichtig um kognitive Funktionen und Dysfunktionen zu verstehen. Neuronale Krankheiten zeigen die Notwendigkeit der Aufrechterhaltung der neuronalen Morphologie für die kognitive Leistungsfähigkeit ist. So wurde zum Beispiel gezeigt, dass der Wachstumsfaktor VEGFD die Länge der Dendriten von kultivierten Neuronen und von basalen Dendriten im erwachsenen Maushippokampus regulieren kann. Zudem weisen VEGFD Knockdown Mäuse ein Defizit in ihrem Langzeitgedächtnis auf. Die genaue kausale Verbindung zwischen veränderter Dendritenmorphologie und mangelnder kognitiver Funktion ist jedoch bisher unbekannt. In der vorliegenden Studie wurden die regulatorischen Auswirkungen von VEGFD auf die Dendritenverzweigungen in verschiedenen zellulären Bereichen und die Konsequenzen für die Funktion sowohl auf Einzelzelleben als auch auf Netzwerkebene untersucht.

VEGFD wurde mittels RNA Interferenz in CA1 Pyramidenneuronen herunterreguliert. Daraufhin wurden detaillierte morphometrische Analysen der basalen und apikalen Dendritenmorphologie durchgeführt. Wie zuvor berichtet, war die Länge und Komplexität der Basaldendriten verringert. Bisher unbekannt war jedoch das der Apikaldendrit ein genau entgegengesetztes Verhalten zeigt und damit die Größe des neuronalen Dendritenbaums insgesamt unverändert bleibt. Des Weiteren, konnten die Veränderungen der Dendriten in den Bereichen festgestellt werden, in denen Eingangssignale verstärkt ankommen. Die Spinedichte in diesen Bereichen war dagegen nicht verändert. Dies legt nahe, dass in Bereichen mit kürzeren Dendriten weniger synaptische Eingänge zur Verfügung stehen und umgekehrt. Des Weiteren wurden die Auswirkungen einer reduzierter VEGFD Expression auf die Funktion von Einzelzellen und auf Netzwerkebene untersucht. Einzelzellmessungen mittels der Patch Clamp Technik zeigten keine Veränderung der passiven und aktiven Eigenschaften, bis auf einen erhöhten Eingangswiderstrand. Die elektrische Stimulation zweier Eingänge *in vivo* zeigte, dass der synaptische Eingang in CA1 Pyramidenzellen nicht verändert ist. Auf Netzwerkebene wurden verschiedene Oszillationen zwischen VEGFD Knockdown

Tieren und Kontrolltieren im Maushippokampus verglichen. Die Ergebnisse zeigten keine Veränderungen in Theta, Gamma und SPW-R Oszillationen in verschiedenen Verhaltenszuständen, wie Bewegung, Reglosigkeit und Schlaf.

Zusammenfassend zeigen diese Ergebnisse, dass die Morphologie der Dendriten von VEGFD reguliert wird. Nachdem VEGFD in CA1 Pyramidenzellen herunterreguliert wurde, konnte eine Verkürzung der basalen und eine Verlängerung der apikalen Dendriten festgestellt werden. Dagegen blieben die grundlegenden elektrischen Eigenschaften der Zellen intakt. Ebenso wenig wirkten sich die Veränderungen der Dendritenlänge auf die untersuchten Netzwerkoszillationen aus. Insgesamt bleibt die Länge des Dendritenbaums stabil (basal + apikal), was einen homöostatischen Mechanismus vermuten lässt. Dies zeigt wie wichtig ein stabiles neuronales Netzwerk im erwachsen Maushippokampus ist.

Abbrevations

A.U.	Arbitrary Units
ACSF	Artificial Cerebrospinal Fluid
AMPA-R	α-amino-3-hydroxy-5-methyl-4-isoxazolepropionic acid receptor
AP	Action Potential
BDNF	Brain-Derived Neurotrophic Factor
CA1, 2, 3	Cornu ammonis areas 1, 2, and 3
CaM kinase	Calcium/calmodulin-dependent kinases
CBP	CREB binding protein
CFC	Cross-frequency coupling
CF$_{\mathrm{PA}}$	Cross-frequency phase-amplitude coupling
CF$_{\mathrm{P\text{-}PA}}$	Cross-frequency phase-phase/amplitude coupling
CNS	Central Nervous System
CREB	cAMP response element binding
DAB	3,3‘-Diaminobenzidin
DG	Dentate Gyrus
EC	Entorhinal Cortex
EEG	Electroencephalogram
E-I	Excitation-inhibition model
EPSP	Excitatory Postsynaptic Potential
ERK-MAPK	Extracellular signal-regulated Mitogen-activated protein kinase
GABA	γ-Aminobutyric acid
gamma$_{\mathrm{f}}$	Fast gamma
gamma$_{\mathrm{m}}$	Middle gamma
gamma$_{\mathrm{s}}$	Slow gamma
HCN channels	Hyperpolarization-activated Cation channels
HEK cells	Human Embryonic Kidney cells

HRP	Horseradish Peroxidase
I_h	h-current
I-I model	Inhibitory-inhibitory model
LFP	Local Field Potential
LTM	Long-term Memory
L-type VGCC	L-type voltage-gated calcium channel
MI	Modulation Index
NMDAR	N-methyl-D-aspartate Receptor
NonREM sleep	Non Rapid Eye Movement sleep
OLM	Oriens lacunosum-moleculare
PBS	Phosphate Buffered Saline
PFA	Paraformaldehyde
PSD	Power Spectral Density
PSF	Point Spread Function
rAAV	Recombinant Adeno-Associated Virus
REM sleep	Rapid Eye Movement sleep
RNAi	Ribonucleic Acid interference
s. lacunosum-moleculare	Stratum lacunosum-moleculare
s. oriens	Stratum oriens
s. pyramidale	Stratum pyramidale
s. radiatum	Stratum radiatum
shSCR	Short hairpin RNA (Scrambled)
shVEGFD	Short hairpin RNA (Vascular endothelial growth factor D)
STM	Short-term Memory
SWR	Sharp Wave-Ripples
VEGFD	Vascular endothelial growth factor D
VEGFR-3	VEGF Receptor-3

List of Figures

Figure 1-1. Circuitry of the hippocampal formation and laminar architecture of CA1. 3

Figure 1-2. Nuclear calcium VEGFD signaling pathway. 8

Figure 1-3. The theta-gamma neuronal code. 11

Figure 1-4. Theta-phase precession of hippocampal place cell spikes and replay. 15

Figure 2-1. Stereotaxic surgery and surgery map. 19

Figure 2-2. Verification of 16-Channel probe position and co-localization with mCherry expression. 26

Figure 2-3. Reconstruction of CA1 pyramidal neurons and analysis of dendritic length by Sholl analysis. 27

Figure 2-4. Hippocampal dimensions and normalization of Sholl spheres to the s. radiatum boarder. 28

Figure 2-5. Analysis of dendritic complexity by the fractal index method. 29

Figure 3-1. VEGFD downregulation causes a decrease of length and complexity of basal dendrites and increase of length and complexity of apical dendrites in CA1 pyramidal cells. 36

Figure 3-2. Spine density is not altered by VEGFD downregulation. 39

Figure 3-3. Passive and active membrane properties of shSCR and shVEGFD expressing neurons. 41

Figure 3-4. Depth profile of theta and gamma LFP recordings and CSD depth profile during voluntary running on a treadmill reveals no change following VEGFD downregulation. 46

Figure 3-5. Depth profile of theta and gamma LFP recordings and CSD depth profile during REM sleep reveals no change following VEGFD downregulation. 47

Figure 3-6. No changes in theta power spectral density (PSD) following VEGFD downregulation during voluntary running on a treadmill. 49

Figure 3-7. No changes in theta power spectral density (PSD) following VEGFD downregulation during REM sleep. 50

Figure 3-8. Gamma amplitude during running in VEGFD knockdown mice. 51

Figure 3-9. Gamma amplitude during REM sleep in VEGFD knockdown mice. 52

Figure 3-10. Cross-frequency phase-amplitude coupling of theta and gamma during running. 54

Figure 3-11. Cross-frequency phase-amplitude coupling of theta and gamma during REM sleep....................55

Figure 3-12. Cross-frequency phase-phase/amplitude coupling of theta and gamma during running. 56

Figure 3-13. Cross-frequency phase-phase/amplitude coupling of theta and gamma oscillations during REM sleep. 57

Figure 3-14. Sharp-wave ripple analysis during voluntary immobility under head-restrained condition *in vivo*. 59

Figure 3-15. Sharp-wave ripple analysis during nonREM sleep *in vivo*....................60

Figure 3-16. Current source density analysis following electrical stimuli of commissural fibers and temporoammonic pathway fibers *in vivo* reveals no difference in VEGFD knockdown mice. 63

Contribution of others

The following scientists and institutions contributed to this work:

- Prof. Dr. Daniela Mauceri and Prof. Dr. Hilmar Bading (Department of Neurobiology, University of Heidelberg) kindly provided plasmids and recombinant adeno-associated viruses (rAAVs).
- shVEGFD silencing efficiency was tested by qPCR by Prof. Dr. Daniela Mauceri (Department of Neurobiology, University of Heidelberg).
- Antonio Yanez (Institute of Physiology and Pathophysiology, University of Heidelberg) supported significantly the analysis of the sag amplitude and capacitance of CA1 pyramidal cells.
- The *in vivo* analysis was performed with custom written Matlab scripts regularly used in the lab of Prof. Dr. Andreas Draguhn (Institute of Physiology and Pathophysiology, University of Heidelberg). Persons involved in programming are Dr. Martin Both (Institute of Physiology and Pathophysiology, University of Heidelberg), diplom-physicist Valeriy I. Kukushka (Dnipro, Ukraine) and Prof. Dr. Adriano Tort (Brain Institute - Federal University of Rio Grande do Norte, Brazil). However, Dr. Martin Both was mostly involved in this project.
- Dr. Kevin Allen (DKFZ, Heidelberg) kindly provided his sharp wave-ripple online detection script. Dr. Martin Both and Matthias Klumpp modified this script for offline detection.
- Spine imaging was performed at the Nikon Imaging Center (NIC), Heidelberg

1 Introduction

1.1 The Hippocampal Formation and its Proposed Functions

The hippocampal formation is a paired structure in the left and right hemisphere of the brain, belonging to the medial temporal lobe. The medial temporal lobe includes further the perirhinal, entorhinal and parahippocampal cortices, which are tightly connected (Squire, Stark, and Clark 2004). The hippocampal formation itself consists of several brain areas, namely the dentate gyrus (DG), the hippocampus proper, subiculum, presubiculum, parasubiculum and entorhinal cortex (EC). Two findings are the basis for the theories on the hippocampal function: (1) Declarative amnesia after hippocampal damage and (2) the discovery of place cells in the hippocampus.

Declarative Memory Theory. At the beginning of the 20th century, von Bechterew suggested a link between the medial temporal lobe and memory formation (von Bechterew 1900). However, the involvement of these structures in the formation of declarative memory (conscious memory for facts and events) became more clear and famous with the systematical studies performed by Brenda Milner on the patient H.M. (Scoville and Milner 1957). H.M. suffered from epileptic seizures. His treatment involved the removal of both hippocampi and related structures. Afterwards, he was not able to produce new declarative memories. At the same time, his short-term memory, procedural memory and long-term memory for events before the surgery were still intact. This led to the proposal that encoding of new memories and the storage into long-term memory is hippocampus-dependent. However, the retrieval of consolidated memories is independent of hippocampal functions. It is still under debate whether consolidated semantic memory becomes at some point hippocampus-independent or it remains hippocampus-dependent forever (György Buzsáki and Moser 2013). Furthermore, it has been proposed that the hippocampus is not only a brain area for memory consolidation but is also an area where different information converges. One fundamental property of episodic memory is the association between several items. An event usually consists of multimodal information, such as sensory, olfactory and spatial information. The hippocampus was suggested as the brain area where information items converge together to form a new memory trace. The ability to complete a whole memory by the recall of only one cue is referred to as pattern completion. Additionally, neurons representing different events need to be separated (pattern separation) for the proper function of pattern completion. The mechanisms for pattern separation and completion are additional described functions of the hippocampus (Rolls 2016).

Spatial Navigation and the Cognitive Map Theory. A prominent discovery in hippocampal research was the observation of the correlation of neuronal spiking activity with the current position of the rat (J. O'Keefe and Dostrovsky 1971). When an animal is moving through space these "place cells" fire at a particular location, the "place field". Hence different place cells respond to different place fields and therefore it was suggested that the collective firing of distinct place cell ensembles forms a neuronal representation of different environments (O'keefe and Nadel 1978). According to their activity pattern, more cells possibly involved in navigation were identified. These grid cells, head-direction cells, and border cells can form together with place cells the neuronal basis of a "cognitive map" (E. I. Moser, Kropff, and Moser 2008; Hafting et al. 2005). Additionally, a replay of the spiking pattern of place cells in awake animals was found during consummatory behaviors, like immobility and slow wave sleep. It was proposed that this replay indicates memory transfer and consolidation during sleep. This hypothesis is supported by the "two-stage model" of G. Buzsáki (1989).

These two theories do not necessarily exclude each other because navigation might use the same encoding mechanism as semantic and episodic memories (e.g. a sequential organization). The technique called "method of loci" used by many memorizers uses visualization to recall information. The person imagines a familiar path and along the path the information to be remembered. In order to recall the information, one imagines walking along the path. The method might work because it is possible to encode item information in sequentially organized place cells (J. Lisman 2015).

In summary, the theories about the function of the hippocampal formation follow mainly two concepts: Involvement in the formation of declarative memory and spatial navigation (Squire, Cohen, and Zouzounis 1984; John. O'Keefe and Nadel 1978).

1.1.1 The Hippocampal Architecture and Circuitry

The hippocampal formation consists of several brain areas, namely the dentate gyrus (DG), the hippocampus proper, subiculum, presubiculum, parasubiculum and entorhinal cortex (EC). The basic structure was first described by Ramón y Cajal (Ramón y Cajal 1911). His student Lorente de Nó further subdivided the hippocampus proper into the cornu ammonis areas 1-3 (CA1-3; Lorente de Nó 1934). All sub-regions of the hippocampal formation are anatomically and functionally strongly connected. A prominent connection is the trisynaptic loop. It starts with projections from the entorhinal cortex layer II to granule cells in the DG (perforant pathway). The axons of the granule cells innervate CA3 pyramidal cells and CA3 neurons project via the Schaffer collaterals to CA1 pyramidal neurons (Figure 1-1; Andersen 2007). Although the trisynaptic loop suggests a serial information flow, parallel projections and recurrent connections are also present, which demonstrates complex circuitries within the hippocampus formation. If not otherwise indicated the reference for this section is Andersen (2007).

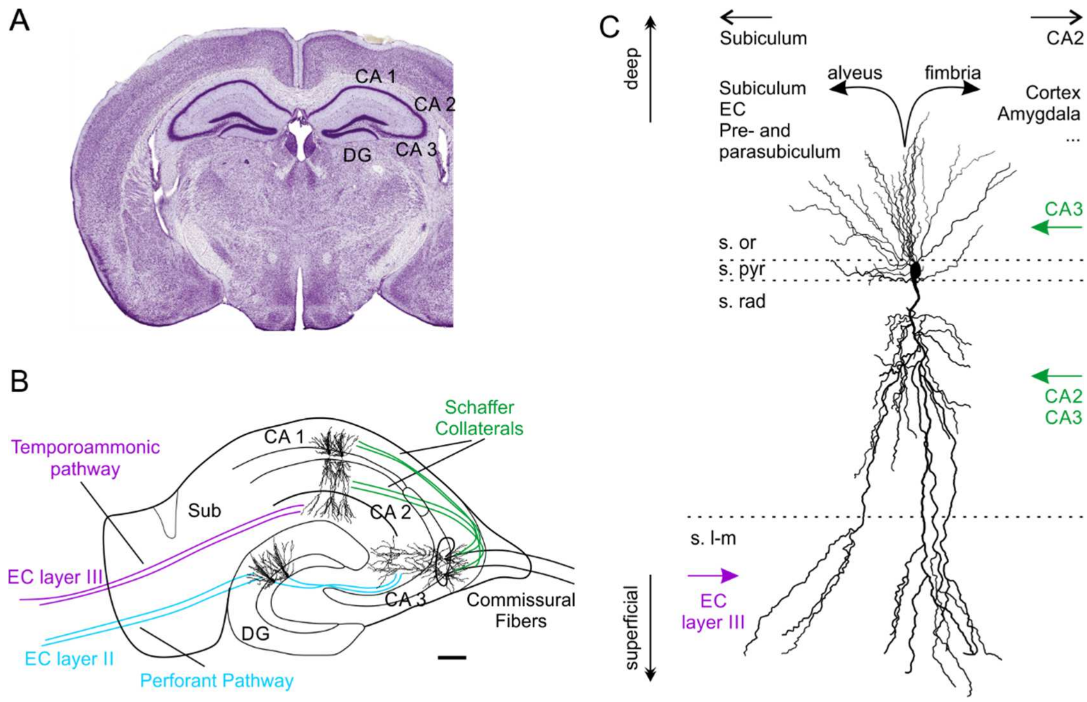
A
CA 1
CA 2
CA 3
DG
B
Schaffer Collaterals
Temporoammonic pathway
CA 1
Sub
CA 2
EC layer III
EC layer II
CA 3
Commissural Fibers
DG
Perforant Pathway
C
deep
Subiculum
CA2
alveus
fimbria
Subiculum
EC
Pre- and parasubiculum
Cortex
Amygdala
...
CA3
s. or
s. pyr
s. rad
CA2
CA3
s. l-m
EC layer III
superficial

Figure 1-1. **Circuitry of the hippocampal formation and laminar architecture of CA1. (A)** Coronal slice from an adult mouse brain. Neurons are visualized by Nissl staining. The hippocampus formation is nicely visible, because of the densely packed somata in DG and CA1-3. Image from the mouse brain atlas (Paxinos and Franklin 2004). **(B)** Schematic drawing of the hippocampal formation and local circuits. The trisynaptic loop is indicated: EC → DG (Synapse 1) DG → CA3 (Synapse 2) CA3 → CA1 (Synapse 3). Scale bar = 200 µm. **(C)** CA1 pyramidal cell in the distinct layers. Input and output targets are indicated (arrows). Modified from Andersen 2007. (CA 1, 2, 3 = Cornu ammonis 1, 2, 3, DG = Dentate Gyrus, Sub = Subiculum, EC = Entorhinal cortex, s. or = stratum oriens, s. pyr = stratum pyramidale, s. rad = stratum radiatum, s. l-m = stratum lacunosum-moleculare).

Dentate Gyrus. The DG consist of three cell layers: Granule cell layer, molecular layer, and hilus. The principal neurons in the DG are called granule cells and their somata are located in the granule cell layer. They are organized in a C-shape around the beginning of CA3 (also called CA3c). Granule cells exhibit no basal dendrites and their apical dendritic trees point away from CA3 in the molecular layer. Their axons project towards the hilus and stratum lucidum of CA3, forming the mossy fibers. These innervate CA3 pyramidal neurons. Afferents from the EC terminate in the outer layer of the molecular layer. They innervate mainly distal apical dendrites of granule cells and a lower number of GABAergic interneurons. They form excitatory synapses with granule cells. The DG is one of the few mammalian brain areas with active neurogenesis (Cameron and Mckay 2001).

CA3. The other type of principal neurons can be found in the three CA areas and the subiculum. Pyramidal cells of CA3 receive input from the DG and from the contralateral CA3. The contralateral fibers cross the midline in the ventral hippocampal fissure. Furthermore, CA3 pyramidal neurons form recurrent connections between each other.

These associational projections are a crucial feature of CA3, involved e.g. in SPW-R generation (section 1.3.4). The axons of CA3 pyramidal cells project via the Schaffer collaterals to the ipsilateral CA1, the ipsilateral CA2 and to the contralateral CA1.

CA2. The narrow zone between CA3 and CA1 is called CA2. CA3 pyramidal cells form synapses with the pyramidal neurons of CA2. In addition, it has recently been shown that DG granule cells send inputs to CA2 pyramidal cells through an alternative route to the trisynaptic loop. Furthermore, contrary to previous knowledge, EC layer III does not project to CA2 (Kohara et al. 2014).

CA1. Pyramidal cells in CA1 receive input from CA3 through the Schaffer collaterals to basal and proximal apical dendrites. This input is part of the trisynaptic loop. Axons from EC layer III terminate onto distal apical dendrites. This is called the temporoammonic pathway and it is the direct input to CA1 from the EC (Doller and Weight 1982). CA1 together with the subiculum are considered as the output regions of the hippocampus formation. Target areas in the inter-hippocampal circuitry are the subiculum, pre- and parasubiculum and lateral and medial EC areas. Furthermore, CA1 innervates moderately the retrosplenial area, visual, auditory, somatosensory, gustatory, olfactory and visceral areas, as well as the basolateral amygdalar complex and the agranular insular and orbital areas and through the fornix the tenia tecta along with the anterior cingulate, prelimbic, infralimbic, and orbital areas (Cenquizca and Swanson 2007).

Subiculum. The axons from EC layer III innervate the subiculum, as well. Furthermore, the subiculum receives input from CA1 neurons. Since it sends projections to many brain regions, it is regarded as the major output region of the hippocampus. Target areas are pre- and parasubiculum, EC, lateral septal complex, hypothalamus, prefrontal and retrosplenial cortical regions, nucleus accumbens, and amygdalar region (Naber, Lopes da Silva, and Witter 2001).

In summary, the hippocampal formation shows a unidirectional, serial and parallel information flow with high inter-hippocampal connectivity (Schacter and Tulving, 1994). Clearly segregated input and output areas make the hippocampal formation a good model region to study signal integration in a defined neuronal circuitry and gain more insight into the brains function.

1.1.2 Pyramidal Cells within the Layers of CA1

The areas CA1-3 of the hippocampus display a mostly uniform laminar pattern. This section focuses on the laminated organization of CA1. If not otherwise indicated the reference for this section is Andersen (2007). The CA1 layers are organized in the following way (from deep to superficial layers; Figure 1-1): alveus, stratum oriens, stratum pyramidale, stratum radiatum, stratum lacunosum and stratum moleculare (often stratum lacunosum-moleculare). Pyramidal neurons stretch vertical through all CA1 layers. Their somata reside in the stratum pyramidale (s. pyramidale). The axon emanates either from the soma or from a basal dendrite mostly towards the s. oriens, as well (Thome et al. 2014). They have several basal dendrites emerging from the soma into the stratum oriens (s. oriens) and one apical dendrite reaches from the soma into stratum radiatum (s. radiatum) and stratum lacunosum-moleculare (s. lacunosum-moleculare). Most of the synaptic input arrives at the dendrites of neurons. The activation of synapses along the dendritic tree generates a potential, which propagates to the soma and axon. There, all signals converge in order to generate a single output, the action potential. However, synaptic potentials must overcome filtering and attenuation caused by the cable properties of the dendrites. The impact of dendritic filtering increases with distance from the soma (Williams and Stuart 2003). In contrast to the classical view, dendrites do not just receive information and passively propagate it to the soma, but they play an important role in signal computation themselves (Branco and Häusser 2011). The complex morphology of CA1 pyramidal neurons might create biological compartments that subdivide the cell into spatially distinct signaling domains (Spruston 2008).

The alveus contains axons from the hippocampus proper. It borders the lateral ventricle, "covering" the hippocampus proper. The alveus is a complex fiber system, consisting not only of fibers originating from inter-hippocampal circuitries (e.g. CA1→EC, CA1→Subiculum, EC→CA1) but also from external areas. It fuses first with the fimbria and later with the fornix.

The s. oriens contains basal dendrites and axons of the pyramidal cells and several interneuron classes (e.g. Oriens Lacunosum-Moleculare (OLM) cells, axo-axonic cells, basket cells; Klausberger 2009). Several basal dendrites form bifurcations and are innervated by Schaffer collaterals from CA3. Further, they receive input from the contralateral commissural fibers and local interneurons. Although less than in CA3, some CA1 pyramidal cell form associational collaterals, projecting to local CA1 interneurons and to the basal dendrites of other CA1 pyramidal cells in s. oriens. Axons from CA1 pyramidal cells emerge into the alveus or in the s. oriens and project towards the subiculum and towards the fimbria/fornix.

The s. pyramidale contains the somata of the pyramidal neurons. It is relatively narrow compared to the other layers and tightly packed, compared to CA3 and CA2. Pyramidal neurons have several basal dendrites and only one apical tree, both descending from the base and the apex of the soma, respectively. The basal dendrites are shorter than the large apical dendrite. Pyramidal neurons located closers to the subiculum receive more input from distal CA3 and cells closer to CA3 receive input from CA2 and proximal CA3 areas.

The s. radiatum is located superficially to s. pyramidale. The proximal apical dendrites of the pyramidal cells emerge in this layer. Oblique dendrites branch from the main apical trunk at various angles. The Schaffer collaterals from CA3 are the main excitatory input onto CA1 cells in this layer. Interestingly, the Schaffer collateral input to s. oriens and s. radiatum originates from pyramidal cells located in distinct areas within CA3. Pyramidal cells from proximal CA3 (closer to DG) innervate preferentially the CA1 apical dendrites and neurons from distal CA3 (closer to CA1) project rather to basal dendrites.

The most superficial layers of CA1 are stratum lacunosum and moleculare, mostly combined as s. lacunosum-moleculare. The distal apical dendrites form oblique branches here and they receive direct excitatory input from fibers originating in EC layer III via the temporoammonic pathway. Additionally, they receive input from the OLM interneurons, which have their soma and basal dendrites in s. oriens and perpendicular axonal projections to the s. lacunosum-moleculare. They inhibit the distal apical tuft of pyramidal cells and thereby they facilitate the CA3 inputs (intra-hippocampal) and inhibiting the EC layer III input (inter-hippocampal; Leão et al. 2012). Dendritic compartments show specific expression pattern of surface and channel. One example is the distally enriched expression of hyperpolarization-activated cation channels (HCN 1 and 2). These channels are non-selective cation channels and they mediate the h-current (I_h). HCN channels become slowly activated by hyperpolarization and depolarization from the resting membrane potential deactivates them. Pyramidal cells in the subiculum and CA1 show this somatodendritic gradient of channels, which enables the neurons to selectively regulate the synaptic responses to the EC layer III input (Lörincz et al. 2002; Magee 1998).

Dendritic Spines. Spines are small protrusions arising along the dendritic shaft. Synapses are located in the spine head, which is typically connected through a thin, long neck to the dendrite. The spine morphology can be very dynamic as they undergo plasticity dependent changes (J. N. Bourne and Harris 2008). Synapses are the major side of information input onto neurons. In the hippocampus and the cortex, the majority of excitatory synapses are located at spines, which is why spine density is often used to get a rough estimate of excitatory input. In contrast, inhibitory synapses are mostly located at the soma or the dendritic shaft. Postsynapses contain the postsynaptic density (PSD), which is the machinery necessary to respond to neurotransmitters and convey information towards the soma. Most spines contain only one synapse. However, in CA1 pyramidal neurons, 10-30 % of the spines contain multiple synapses with perforated PSDs (Harris and Stevens 1989). They are called perforated synapses, are larger and have more AMPA-R compared to a single synapse. The number of perforated synapses in CA1 pyramidal cells increases with distance to the soma and their AMPA-R expression is the highest in the distal s. radiatum and the lowest in s. lacunosum-moleculare. This suggests compartment specific mechanisms to minimize the influence of distance to the synaptic efficacy (D. A. Nicholson et al. 2006). Spine density varies along the dendritic tree and in brain areas. In CA1 pyramidal cells, the spine density is higher in s. radiatum and s. oriens compared to s. lacunosum-moleculare. Often, spines are considered as dendritic sub-compartments for signaling on their own (Colgan and Yasuda 2014).

Spines and synapses are crucial for synaptic plasticity. It has been proposed that spatial learning correlates with a general increase in spine density and thereby an increase of excitatory input in CA1 pyramidal cells (M. B. Moser, Trommald, and Andersen 1994). Not only spine density but also the size and shape are very dynamic during synaptic plasticity (Fortin, Srivastava, and Soderling 2012). It has been suggested that thin spines are more dynamic and thus contribute to learning processes, whereas thicker spines are less plastic and contribute more to memory storage (J. Bourne and Harris 2007). Repeated activation of small spines can convert them into stable spines, promoted by AMPA and NMDA receptors. Spine and synapse pathology is often observed in neurodegenerative diseases, e.g. Alzheimer's disease (Yu and Lu 2012).

In summary, distinct dendritic morphology, synaptic inputs and protein expression patterns separate the dendritic tree of CA1 pyramidal cells into different sub-compartments. The variation in structure and molecular compositions allows neurons to perform different functional tasks. Interesting questions remain. How close are the functional properties linked to the morphology of pyramidal cells? Do more dendrites lead to a higher output or do cells try to keep the status quo by homeostatic mechanisms? Is there a hierarchy between adaptive and maintenance mechanisms?

1.2 Influence of VEGFD on Dendritic Morphology and Long-Term Memory

Dendrites represent the main input site of neurons and dendritic geometry influences the connectivity of neurons. The formation, adaption, and maintenance of dendritic branches are important for learning and memory processes (Koleske 2013). Many extrinsic and intrinsic molecular mechanisms are involved to regulate the establishment and the maintenance of the dendritic tree, including secreted molecules, cell surface receptors, cell adhesion molecules, PSD proteins, signaling molecules, regulators of the actin cytoskeleton, Golgi trafficking molecules, transcription factors and calcium signaling (Arikkath 2012).

The communication between synapses and nucleus is crucial to ensure an activity dependent regulation of dendritic morphology. Calcium signals from the synapse to the nucleus couple synaptic activity to gene transcription (Bading, Ginty, and Greenberg 1993; Hardingham, Arnold, and Bading 2001). This communication influences neuronal survival, long-term memory formation and more (Hagenston and Bading 2011).

Calcium enters the cell through N-methyl-D-aspartate receptors (NMDARs) or L-type voltage-gated calcium channels (VGCCs; Bading, Ginty, and Greenberg 1993; Bading et al. 1995). Intracellular calcium itself can spread through the cytosol by diffusion or active waves until the nucleus. Calcium binding proteins, expressed in subcellular compartments regulate calcium signaling spatially, e.g. regulation of transcription in the cell nucleus (Schwaller 2009). Calcium signals can influence locally neuronal excitability for example through the regulation of associated synapses, spines or trafficking of proteins and organelles. Furthermore, calcium can activate signaling cascades, going from the synapse to the nucleus, and thus couple neuronal activity to transcriptional processes (Bloodgood and Sabatini 2007).

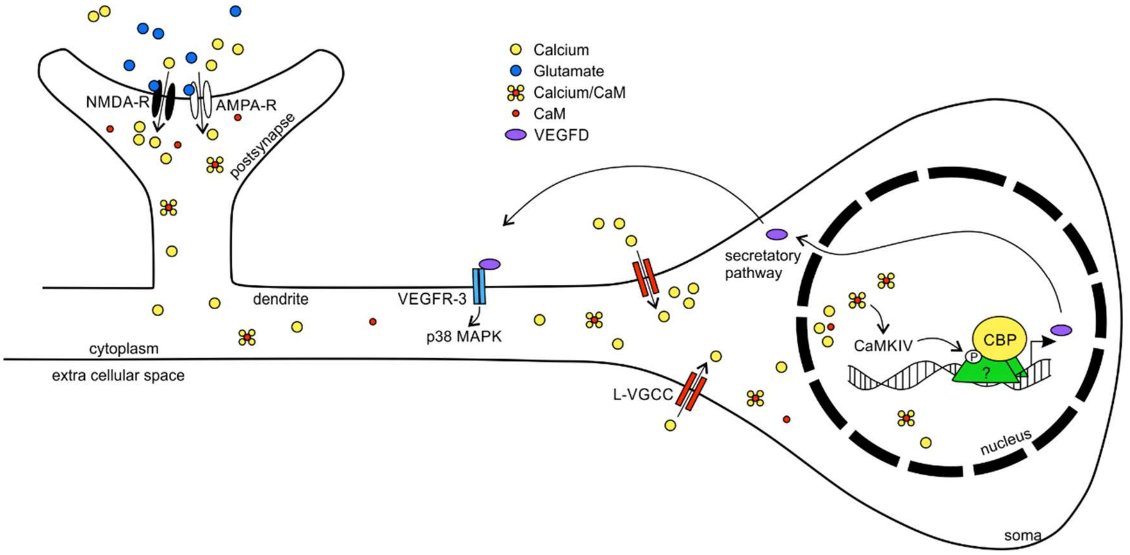

Figure 1-2. **Nuclear calcium VEGFD signaling pathway.** Schematic neuron with a postsynapse and nucleus in the soma. Presynaptic potentials cause the release of Glutamate, which binds to the postsynaptic NMDA and AMPA receptors. Calcium enters the cell, first through AMPA receptors. This causes a depolarization, which releases the magnesium block from NMDAR and calcium can enter the cell, as well. Furthermore, the depolarization also causes the calcium influx through L-VGCCs. Inside the cell, calcium binds to CaM kinases. Calcium and Ca^{2+}/CaM can activate several signaling cascades and thereby phosphorylate CBP in the nucleus. This leads to activity dependent gene transcription of VEGFD. VEGFD enters the Golgi apparatus and is released. In the extracellular space, VEGFD binds to the VEGFR-3 and p38 alpha MAP kinase becomes activated. (N-methyl-D-aspartate receptors (NMDARs), α-amino-3-hydroxy-5-methyl-4-isoxazolepropionic acid receptor (AMPAR), L-type voltage-gated calcium channels (L-VGCCs), calcium/calmodulin-dependent kinases (CaM kinase), cAMP response element binding (CREB), CREB binding protein (CBP), phosphorylation (P)). Modified from Bengtson and Bading 2012.

Several genes are regulated through nuclear calcium signaling. One example is the vascular endothelial growth factor D (VEGFD), known as a mitogen for endothelial cells and regulator of angiogenesis and lymphatic vascular system (Lohela et al. 2009). Additionally, VEGFD was identified as a factor involved in the control of dendritic arborization of neurons (Mauceri et al. 2011; Figure 1-2). Mauceri and colleagues showed that VEGFD expression requires basal neuronal activity, which activates calcium influx through NMDAR and L-type VGCCs. Intracellular signaling of calcium and calcium/calmodulin–dependent kinases (CaM kinases) is mediated through CaMKIV, which phosphorylates the CREB binding protein (CBP). CBP interacts with many possible transcription factors. However, the VEGFD signaling pathway does not involve the transcription factor cAMP response element binding protein (CREB). Interestingly, the calcium-binding protein parvalbumin regulates the calcium buffering capacity in the nucleus, influencing nuclear calcium signaling and VEGFD gene transcription (Daniela Mauceri et al. 2015).

Afterwards, VEGFD enters the Golgi apparatus, becomes further processed, packed into vesicles and segregated. The extracellular VEGFD binds to the VEGF-receptor 3 (VEGFR-3), which is a tyrosine kinase receptor. VEGFD controls dendritic arborization through an autocrine mechanism. Mauceri et al. showed that VEGFD shapes morphology through the p38 alpha mitogen-activated protein (MAP) kinase activation. However, the exact downstream signaling pathway of the VEGFR-3 is unclear. Patch clamp recordings of VEGFD downregulated cultured neurons revealed a smaller membrane capacitance and a reduced number of functional AMPA receptors, confirming the reduced dendritic surface area. Furthermore, it was shown that VEGFD knockout mice exhibit shorter and less complex basal dendrites of CA1 pyramidal cells. These mice show a spatial memory deficit in the Morris water maze and an impaired memory formation in the contextual fear conditioning (D Mauceri et al. 2011). Additionally, it has been shown that nuclear calcium VEGFD signaling is not only involved in memory consolidation, but also in extinction of fear memory (Hemstedt et al. 2017).

In summary, VEGFD was identified as a regulator of dendritic morphology in neurons. Nuclear calcium-VEGFD signaling mediates the maintenance of the dendritic arborization upon neuronal activity. Further, it was shown that a loss of VEGFD leads to shorter dendrites in cultured neurons and basal dendrites in the adult mouse hippocampus. The altered dendritic morphology causes a long-term memory deficit in hippocampus dependent tasks. The exact mechanism how different dendritic geometry leads to memory deficits remains unknown. However, the shape and expansion of the dendritic tree highly influences the synaptic connections of neurons. Therefore, it is possible that it affects the function of neuronal oscillations in CA1 that are crucial for memory formation and consolidation.

1.3 Hippocampal Network Oscillations

Neuronal networks exhibit synchronous activities resulting in oscillations at various frequencies (from 0.5–600 Hz). Distinct oscillatory frequency ranges are associated with different behavioral or perceptual states and were observed in various brain regions, including the hippocampus, olfactory bulb, thalamus, and neocortex. Oscillations can occur in single cells, within local networks and between brain areas (Hutcheon and Yarom 2000).

Oscillations have different functions, depending on the brain region and vigilance state they occur. In general, oscillations make it possible to predicted their time course and to reset their phase. They support input selectivity and plasticity, synchronization of cell assemblies, consolidation and combination of learned information and spike phase precession (Buzsaki and Draguhn 2004). Higher frequency oscillations are constraint to local networks and slower oscillations communicate often with neuronal networks further away. This allows the brain to carry out multiple operations at the same time at several temporal and spatial scales.

In the hippocampus, three major frequency ranges have been characterized: Theta oscillations (4-10 Hz), gamma oscillations (35-160 Hz) and sharp waves and associated ripples (140-200 Hz; G. Buzsáki et al. 2003; Csicsvari et al. 2003b). These frequency bands are in focus of this thesis and are addressed in more detail in the next sections.

1.3.1 Theta Oscillations

Theta waves (Greek letter: Θ) oscillate in the frequency range of 4-10 Hz in the hippocampus. They occur typically during rapid eye movement (REM) sleep and active, awake behavior (Vanderwolf 1969). In the hippocampus, theta is mostly present in the CA1 area. However, theta oscillations are also present in CA3 and DG. (G. Buzsáki et al. 1986). Two types of theta can be distinguished by their sensitivity to atropine, a muscarinic receptor blocker. The atropine sensitive or arousal theta (a-theta) occurs during arousal and attention. This depends on the cholinergic modulation of interneurons and the CA3 recurrent system. The translational-movement theta (t-theta) is atropine resistant and occurs during movement through space. T-theta is dependent on the EC input to CA1 and DG and NMDA receptor activation. Both theta types occur during REM sleep phases (Kramis, Vanderwolf, and Bland 1975).

The classical model for theta rhythm generation proposed that the minimum condition is the connection between the hippocampus and the medial septum-diagonal band of Broca (MS-DBB). It is not clear, whether the MS-DBB is the pacemaker or the rhythm depends on a reciprocal connection between the two areas (Petsche, Stumpf, and Gogolak 1962; Wang 2002). The extracellular field potential of theta in CA1 is generated by excitatory and inhibitory input. The excitatory drive comes from the EC onto distal dendrites of CA1 pyramidal cells. The GABAergic input from the MS-DBB rhythmically hyperpolarizes hippocampal inhibitory neurons (basket and chandelier cells) and the cholinergic input from MS-DBB depolarizes pyramidal neurons and interneurons producing inhibitory postsynaptic potentials at the soma (György Buzsáki, Lai-Wo S., and Vanderwolf 1983a). However, the inhibitory drive can also come from

CA3 and other interneurons. The current diploes across the layers cause the amplitude and phase versus depth profile (Leung 1984). This model of “rhythm and current generators” for theta generation might be oversimplified and has some inadequacies (György Buzsáki 2002).

Three functions of hippocampal theta have been suggested. First, theta might provide a global synchronization mechanism. This is supported by the fact that theta oscillations exist not only in the hippocampus but also in the septum, subiculum, amygdala, EC and more (Sirota et al. 2008). Furthermore, neurons in other subcortical regions are phase locked to the hippocampal theta (György Buzsáki 2002). By exchanging information in a phase-locked manner, theta could provide process to combine sensory and memory-activated neurons in time, e.g. the coupling of theta oscillation to locomotion (Fuhrmann et al. 2015).

Second, theta oscillations can provide a periodic temporal framework for spike timing of hippocampal neurons, called phase precession. The firing precession of a pyramidal cell varies from one theta cycle to the next (phase precession, Figure 1-4). While the animal is walking through the place field of a neuron, the cell fires spikes in a slightly higher frequency than the theta cycles. Consequently, the spikes occur on earlier points on the theta wave over the course of the place field. This conveys information about the animals’ position (O Jensen and Lisman 2000).

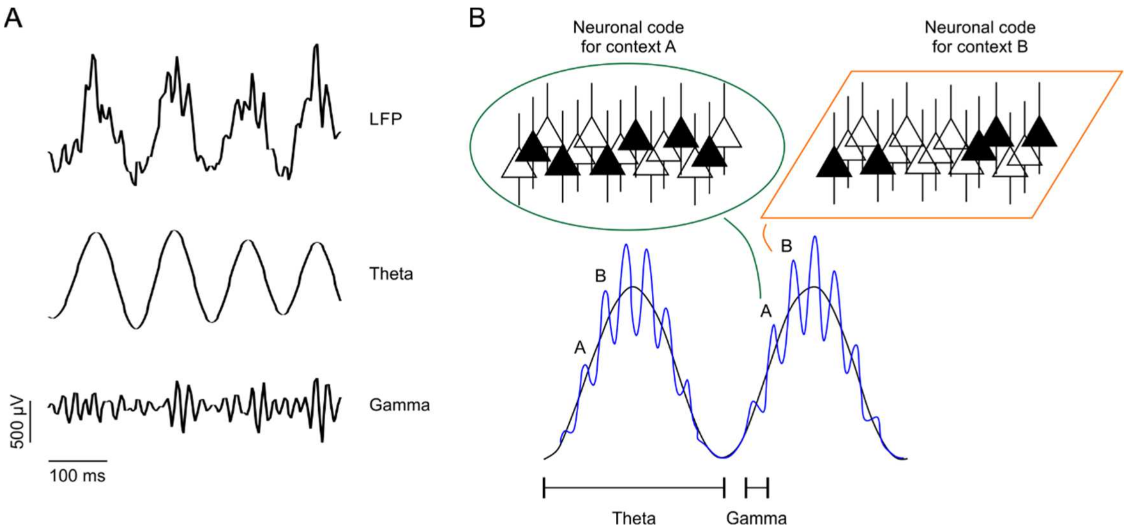

Figure 1-3. **The theta-gamma neuronal code.** (A) Local field potential (LFP) example trace of a theta nested gamma oscillation with four theta cycles. 4-10 Hz bandpass filtered theta oscillation and 35-70 Hz filtered gamma oscillation are shown below. **(B)** Schematic representation of two theta cycles with gamma oscillations. Individual memory representations, encoded by a different ensemble of cells (context A and B), are activated in different gamma cycles. Individual contexts are repeatedly activated in every theta cycle. Modified from Ole Jensen and Colgin 2007

Third, theta oscillations provide temporal control over the induction of plasticity and thus contribute to memory encoding and retrieval. For example, inputs arriving at the positive peak cause synaptic potentiation and inputs arriving at the negative peak cause synaptic depression. Therefore it was proposed that different theta phases represent different modes of operation (Hasselmo 2005). Hasselmo proposed that new information entering from the EC is encoded on the theta peak and during the trough, the retrieval of information from the hippocampus to the EC occurs. This was further confirmed by Schomburg et al., 2014.

1.3.2 Gamma Oscillations

Originally, the frequency band for gamma oscillations (Greek letter: γ) was proposed to be 35-85 Hz (Bressler and Freeman 1980). However, in the past years, it has been expanded to higher frequencies and three distinct sub-bands have been distinguished. The three gamma oscillations vary in their frequency, spatial distribution and theta phase correlation. Commonly, they are separated in a slow-frequency gamma, generated by CA3 input, a middle-frequency band, by entorhinal cortex inputs and a local in CA1 generated high-frequency gamma (Colgin et al. 2009; Schomburg et al. 2014; Belluscio et al. 2012). However, different frequency ranges have been reported. György Buzsáki and Wang (2012) separated the three gamma bands as follows: slow gamma (gamma$_s$ 30-50 Hz), mid-frequency gamma (gamma$_m$ 50-90 Hz) and fast gamma (gamma$_f$ 90-140 Hz). According to Lasztóczi and Klausberger (2016), hippocampal place cells in CA1 couple to gamma$_s$ 32-41 Hz, gamma$_m$ 57-86 Hz and gamma$_f$ 92-133 Hz. Scheffer-Teixeira et al. (2012a) define the oscillation occurring in CA1 in the frequency range of 60-100 Hz as high gamma and 120-160 Hz as high-frequency oscillations. There is a general agreement that different sub-bands of gamma oscillations can co-exist or occur in isolation.

Gamma oscillations have been described in the neocortex, entorhinal cortex, amygdala, thalamus, olfactory bulb and in the hippocampus DG and CA regions. In the DG they are generated by external input from EC layer II (Csicsvari et al. 2003a). In CA1-3 gamma oscillations do not necessarily require external inputs and they depend on the interaction of excitation and inhibition. Two models have been suggested to be relevant for gamma generation: the excitation-inhibition model (E-I model) and the inhibition-inhibition model (I-I). The I-I model is based on the synchronization by mutual inhibition between interneurons. In the E-I model synchronization is generated by an excitation-inhibition loop, through the reciprocal interaction of pyramidal neurons and interneurons (György Buzsáki and Wang 2012). The mechanism underlying gamma oscillation is mainly based on GABA$_A$ receptor mediated inhibition (Csicsvari et al. 2003; György Buzsáki and Wang 2012). Slow-gamma (gamma$_s$) oscillations in CA1 are generated by the gamma-phase locked discharge of CA3 pyramidal cells. CA3 is not the immediate cause of CA1 gamma, but feed-forward inhibition is involved through the activation of fast-spiking interneurons and parvalbumin-positive CA1 basket cells. Gamma$_s$ oscillations occur during the descending theta phase and are the strongest during memory recall (Colgin et al. 2009; Montgomery and Buzsáki 2007)). The middle gamma oscillation (gamma$_m$) is generated by the EC layer III input to the distal apical dendrites of CA1 pyramidal cells. This gamma band correlates with the theta peak. Fast gamma (gamma$_f$) oscillations are generated by a local network of pyramidal and interneurons in CA1 (Schomburg et al. 2014).

Gamma oscillations play a role in sensory binding, attention selection, conscious experience and especially in the hippocampus, encoding and retrieval of memory (Miltner et al. 1999; Ole Jensen, Kaiser, and Lachaux 2007). Gamma oscillations show a phase coherence in distinct networks, thereby functionally synchronizing and facilitating communication between brain regions (Sirota et al. 2008; Colgin et al. 2009). Gamma oscillations are coupled to other oscillations, like theta within or across structures and by this facilitate memory recall and working memory processes (Adriano B L Tort et al. 2008; Figure 1-3; sections 1.3.1 and 1.3.3).

1.3.3 Cross-Frequency Coupling of Theta and Gamma

Neighboring frequency bands within the same neuronal network are usually associated with different vigilance states and are in competition. However, rhythms do also co-exist and interact with each other (Figure 1-3). The interaction of different oscillation is called cross-frequency coupling (CFC) and can follow several principles: amplitude-amplitude, phase-phase, phase-frequency or phase-amplitude coupling (Ole Jensen and Colgin 2007). The modulation of the amplitude of a fast oscillation (gamma 35-160 Hz) by the phase of a slow oscillation (theta 4-10 Hz) in the hippocampus is a very prominent example of this phenomenon (Bragin et al. 1995).

A possible mechanism of cross-frequency coupling of phase and amplitude (CFC$_{P\text{-}A}$) could be the regulation of excitability of the neurons producing the gamma rhythm by the theta rhythm. By phase locking this, a fluctuation in the gamma rhythm locked to the theta rhythm occurs. One network model has been described in which concurrent theta and gamma oscillations are produced by slow and fast GABAergic feedback (White et al. 2000). Furthermore, it has been shown that synaptic inhibition onto parvalbumin-positive interneuron is required for theta-gamma coupling (Wulff et al. 2009).

Several theories have been proposed regarding the functional relevance of CFC. The coupling of gamma with a certain theta phase might recruit a cell assembly involved in the processing at that time (Figure 1-3; sections 1.3.1 and 1.3.2). Thus, theta provides a time frame along that several functional networks are integrated, each one associated with a certain gamma episode. Furthermore, CFC was proposed to be involved in working memory. The idea is that 7±2 gamma cycles separate the theta phase in distinct "time slots". Separate memory items are represented in separate gamma cycle and the number of gamma cycles per theta cycle could represent the span of working memory (J. E. Lisman and Idiart 1995). An interesting idea proposes, that during theta phase-precession (section 1.3.1) the phase-precession advances one gamma cycle per theta cycle, suggested by the fact that a place field is active for 5-10 theta cycles which corresponds to the gamma frequency (40-80 Hz). So basically, the same phase-precession mechanism for gamma as for place cell spikes (Ole Jensen and Colgin 2007).

In summary, CFC is an effective mechanism to functionally link active cortical circuits. Theoretical and practical work showed that CFCs play a role in sequential memory organization, maintenance of working memory and memory recall (J. Lisman 2005; A. B. L. Tort et al. 2009).

1.3.4 Sharp Wave Ripples

Sharp wave ripple (SPW-R) complexes are the most synchronous bursts in the hippocampus. They are associated with consummatory states, including immobility, behaviors and slow wave sleep. (John O'Keefe 1976; G Buzsáki et al. 1992). The SPW-R complex consists of two events, the population burst called sharp wave (SPW) and the fast ripple oscillations (R). The synchronous discharge of the recurrent connections in CA3 depolarizes the apical dendrites of 50,000 to 150,000 pyramidal cells in CA1 in the s. radiatum via the Schaffer collaterals, thereby generating the SPWs (Csicsvari et al. 2000). Because of this excitatory gain, SPW-R can drive neurons in downstream areas of the hippocampus. On the other side, inputs from slow oscillations from the neocortex, spindles from the thalamus and others can influence the SPW-R complexes (György Buzsáki 1986).

The strong excitatory drive form CA3 is compensated in CA1 by local circuits, resulting in the ripple events. Ripple oscillations are generated by the interaction between pyramidal neurons and perisomatic interneurons (Ylinen et al. 1995). The ripple troughs represent the action potentials of the synchronously discharging neurons. The ripple peaks reflect the outward membrane currents at the soma of pyramidal neurons, generated by the hyperpolarizing inputs from parvalbumin-positive basket cells and other interneurons. This interaction determines the ripple frequency of 150-250 Hz by the time constant of $\mathrm{GABA_A}$ receptors (Csicsvari et al. 1999). SPW-R complex terminate due to a hyperpolarization, which imposes a short refractory time after each event. This is also visible in the LFP as a negative event (English et al. 2014).

One very important feature of SPW-R complexes is that the neurons participating in the event are sequentially organized. This sequence reflects a temporally compressed version of the theta-phase precession firing pattern during awake periods (Figure 1-4). This led to the "two-stage model" hypothesis of memory formation (G. Buzsáki 1989). As proposed by this model, SPW-R complexes might be involved in the formation and consolidation of memory. The two-stage model suggests, that during learning the neocortex provides the hippocampus with new information, which results in transient synaptic reorganization of circuits (theta phase). This is temporally held in CA3. In the second stage, during consummatory behaviors associated with SPW-R, the CA3 recurrent network discharges, and the modified hippocampal content is transferred to the neocortex (SPW-R state; Figure 1-4). This theory suggests that SPW-R are important for memory transfer and consolidation. Further support for this comes from the selective perturbation of SPW-R in the hippocampus, which affects hippocampus-depended memories (Jadhav et al. 2012).

In summary, the complex mechanism underlying the network oscillations described above indicates the importance of a delicate physiological and morphological control of distinct somatodendritic domains of pyramidal cells. This is very crucial for the selection of assemblies, regulation of plastic processes and maintenance of input and output connections.

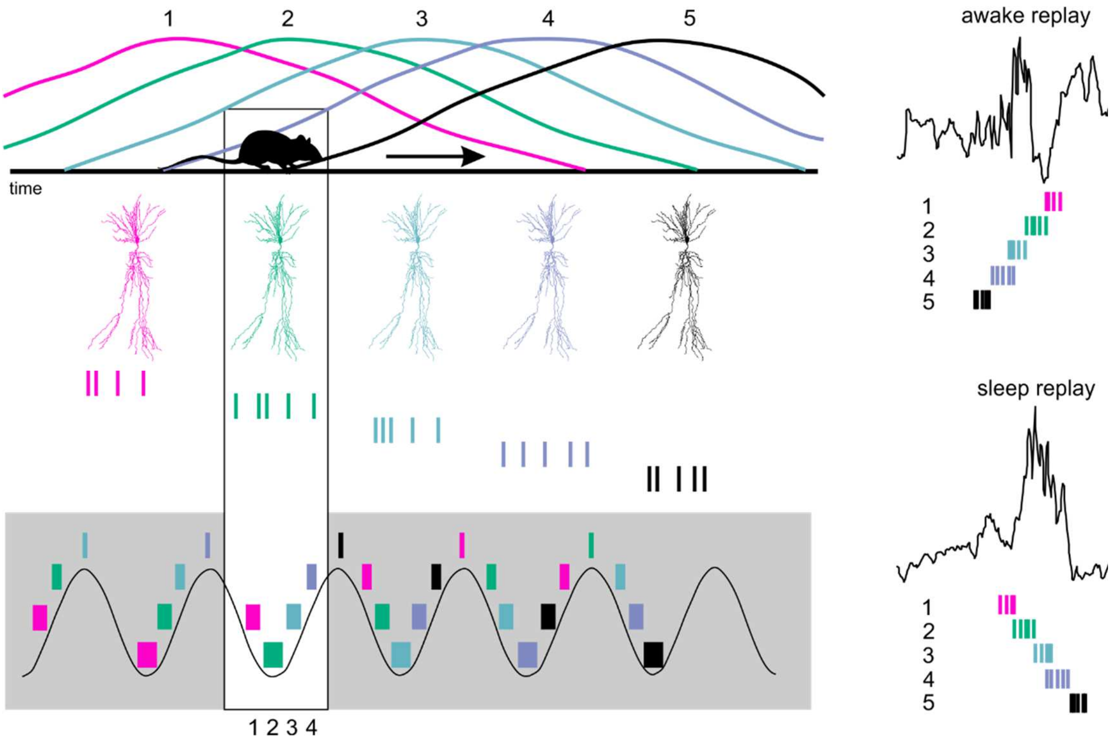

Figure 1-4. **Theta-phase precession of hippocampal place cell spikes and replay.** Place cells in the hippocampus encode the animals current location ("place field", No. 1-5) by their firing rate distribution. The firing of place cells exhibits a temporally and time-compressed organization within the theta-phase (theta-phase precession, grey area). Place cells with overlapping place fields tend to fire together, forming a cell ensemble. During subsequent consummatory behaviors, e.g. eating the reward, the spike sequence is replayed in reversed order during SPW-R (reversed replay). Afterwards, during slow-wave sleep, when the brain is isolated from external stimuli, the firing sequence is replayed in the same order (forward replay). Modified from Girardeau and Zugaro 2011 and Dragoi 2013.

1.4 Aims of this Study

Recent literature suggests that the vascular endothelial growth factor D (VEGFD) regulates dendritic morphology in neurons. RNAinterference (RNAi) mediated knockdown of VEGFD in cultured neurons as well as in murine CA1 pyramidal cells revealed shorter and fewer complex dendrites. However, this effect was only shown for the basal dendrites of pyramidal cells. Furthermore, changes in basal dendritic length were correlated with long-term memory deficits in the Morris water maze, in a fear conditioning and in a fear extinction task (D Mauceri et al. 2011; Hemstedt et al. 2017).

This study investigated the regulatory effect of VEGFD on the entire dendritic tree of CA1 pyramidal cells and potential functional consequences *in vivo*. It aimed to gain a better understanding of the regulatory effect of VEGFD on distinct dendritic compartments and finding a link between morphology changes and cognitive performance.

This involved the following aspects in particular:

- Analysis of morphology changes in the basal and apical dendritic tree upon VEGFD downregulation.
- The investigation of spine density along basal and apical dendrites in VEGFD deficient cells.
- Measurement of the functional consequences of dendritic morphology changes on a single cell level.
- Study of the effect on synaptic inputs in CA1 pyramidal cells upon VEGFD downregulation by electrical stimulation of two distinct pathways.
- Investigation of the impact of VEGFD downregulation on neuronal networks, in particular on network oscillations like theta, gamma and SPW-R under different vigilance stages.

2 Materials and Methods

2.1 Animal Ethical Approval and Housing

All experiments were conducted in accordance with the state government of Baden-Württemberg in Karlsruhe and in conformity with relevant regulations and guidelines of the University of Heidelberg (Tierversuchsantrag: 35-9185.81/G-121/13). Adult 8 weeks old, male C57BL/6 mice were purchased from Charles River Laboratories (Sulzfeld, Germany). They were housed in a ventilated Scantainer (Scanbur BK) under an inverted 12 hours light/dark cycle (light from 8 pm – 8 am) at a temperature of 22±2 °C and a relative humidity of 45 – 65%. Mice used for *in vivo* recordings were housed under a naturalistic light/dark cycle (light from 8 am – 8 pm). Food and water were provided ad libitum. All efforts were made to minimize the number of animals and their suffering.

2.2 Plasmids and Recombinant Adeno-Associated Viruses

Plasmids and recombinant adeno-associated viruses (rAAVs) were kindly provided by Prof. Dr. Daniela Mauceri and Prof. Dr. Hilmar Bading (Department of Neurobiology, University of Heidelberg, Im Neuenheimer Feld 364, 69120 Heidelberg, Germany).

The rAAV vectors for VEGFD downregulation were generated as described by Klugmann et al. (2005) and Mauceri et al. (2011). To produce the rAAV1/2 vector, human embryonic kidney (HEK) 293 cells were transfected with the AAV plasmid pACKmC176 together with the dFdelta6 (adenovirus helper plasmid), pNLrep (AAV2) and pH21 (AAV1) helper plasmids. The pACKmC176 plasmid contained the shRNA sequence and the mCherry sequence as reporter gene. Cells were harvested 60 hours after transfection and rAAVs were purified using a heparin column. VEGFD silencing efficiency was tested by qPCR. The efficacy of cell infection was determined by analyzing the mCherry expression and it ranged around 80±5% of the neuronal population.

U6 and CaMKII promoters were used to express shRNA and mCherry, respectively (Lau and Bading 2009). The following shVEGFD sequence was used: GGGCTTCAGGAGCGAACAT. A scrambled version of this sequence was used as a control (shSCR): GTGCCAAGACGGGTAGTCA (D Mauceri et al. 2011). In this thesis, the control group is referred to as shSCR and the VEGFD downregulated group is abbreviated by shVEGFD.

2.3 Chemicals and Solutions

All solutions were made with aqua bidest. (Millipore SAS, Milli-Q Reference Water Purification System).

PB buffer	0.2 M PB (pH = 7.4) with 10 M NaOH 28.5 g [NaH_2PO_4 x H_2O] 5.2 g [Na_2HPO_4 x $2H_2O$] In aqua bidest.
PBS buffer 10x	1.37 M NaCl 27 mM KCl 80 mM Na_2HPO_4 20 mM KH_2PO_4 In aqua bidest., no pH-value calibration
PFA 4% in 0.1 M PB buffer	0.2 M PB (pH = 7.4) 200 ml aqua bidest. 20 g paraformaldehyde (Sigma-Aldrich) Mixed at 60°C under constant stirring
Mowiol	6 g Glycerin 2.4 g Mowiol 4-88 (Carl Roth) 6 ml Aqua bidest. 12 ml 0.2 M Tris-HCl (pH = 8.5)
10% TritonX-100	10% TritonX-100 (Merck) in 1xPBS

2.4 Animal Surgery

The surgery was performed to deliver rAAV vectors for VEGFD downregulation and to implant chronically electrodes. The weight of the animals on surgery day was 22 – 25 g. The analgesic Buprenorphine – Hydrochloride (0.1 mg/kg, Temgesic pharmaceutical vial, Reckitt Benckiser Healthcare, UK) was administered subcutaneously before and 8 hours after the surgery. Anesthesia was induced with a mixture of 4% Isoflurane and 96% medical O_2 and maintained using 1.5 - 2.5% isoflurane (Baxter, Unterschleißheim, Germany). Subsequently, the animal was placed in a stereotaxic apparatus (Kopf Instruments). Body temperature was maintained at 36 - 37 °C by a small animal thermoregulation device (ATC-2000, World Precision Instruments) and constantly monitored throughout surgery. After head fixation onto the stereotaxic frame, the head was shaved and cleaned with distilled water and 70% ethanol (Figure 2-1,A).

Before starting the surgery anesthesia depth was verified by testing the toe pinch reflex. After the skin was opened with a scalpel, Bregma and Lambda were used as landmarks to calibrate the head. Bregma was used as zero point for desired coordinates. Holes were drilled in the skull at the desired positions (Figure 2-1,B; holes diameter 0.5 - 0.9 mm, driller: Foredom, drills: Hager & Meisinger). Coordinates were taken from Paxinos and Franklin (2004). Subsequently, virus injection was performed (section 2.4.1) for further *in vitro* or *in vivo* studies.

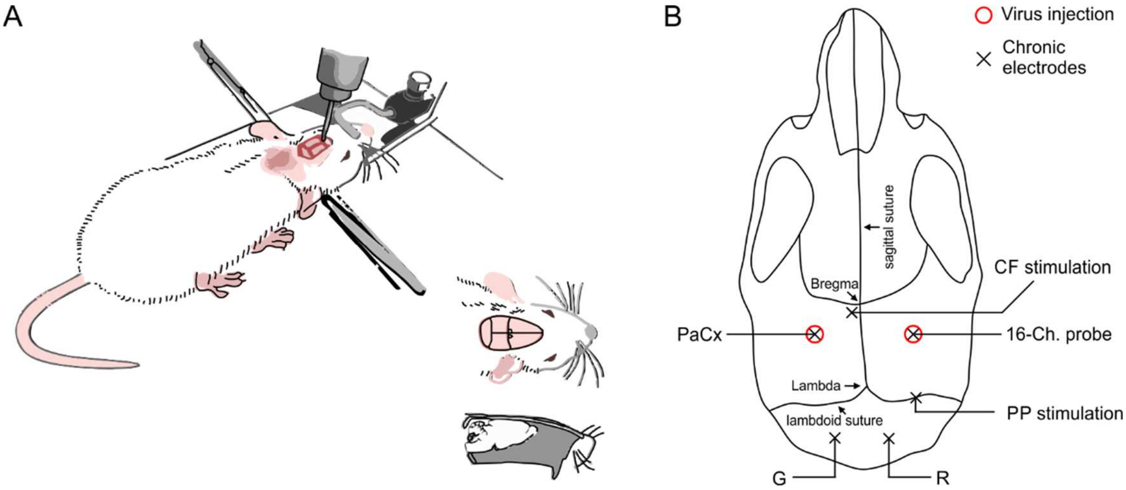

Figure 2-1. **Stereotaxic surgery and surgery map. (A)** Scheme of the stereotaxic surgery. Adapted from clodrosome.com. **(B)** Schematic representation of injection sites (red circles) and chronic electrode implantation (black crosses) relative to Bregma.

2.4.1 Stereotaxic Virus Injection

Viruses are commonly used to modulate specific genes in a desired area of the brain. In this study, rAAV1/2 subtypes were delivered by stereotaxic injection into the CA1 region of the hippocampus in both hemispheres (AP -2.0 mm, ML -1.5 mm, DV -1.3 mm (400 nl), -1.4 mm (300 nl), -1.5 mm (300 nl)). Either 1 µl shSCR or shVEGFD virus solution (1:2 in 1xPBS) was delivered to three different depths in CA1 at 200 nl/min speed. A Hamilton syringe with a 33 GA beveled needle was used (Nanofil Syringe, World Precision Instruments) and the delivery was regulated by a microprocessor controlled minipump (UMP3, World Precision Instruments). The needle was pulled back 10 minutes after injection, in order to allow a proper diffusion of the solution into the tissue.

Finally, the skin was sutured (Coated Vicryl, Ethicon) and the mouse was allowed to wake up under constant monitoring of temperature and breathing rhythm. If two mice were injected at the same day, they were held together. After three weeks, necessary for expression of the vector, it was possible to perform *in vitro* patch clamp recordings with subsequent stainings (sections 2.4.2, 2.5.2 and 2.6) or *in vivo* recordings (section 2.6). For *in vivo* recordings a 16-Channel silicon probe (NeuroNexus) was implanted in a second surgery.

2.4.2 Chronic Implantation of Electrodes

For chronic electrodes implantation, previously injected animals (shVEGFD-mCherry or shSCR-mCherry) were prepared for surgery as described in section 2.4. Holes for electrode implantation were drilled at desired positions as shown in Figure 2-1. For stimulation, two custom built, bipolar electrodes were used. They consisted out of twisted NiChrome wires (thickness: 100 µm, California Fine Wire Company) and exhibited a tip distance of appr. 50 µm and an angle of appr. 45° for increased stimulation area. One stimulation electrode was implanted in the left fimbria-fornix (AP -0.82 mm, ML -0.5 mm, DV -2.25 mm) for ventral commissural fiber inputs stimulation and the other one in the angular-bundle for activation of temporoammonic pathway inputs (AP -4.2 mm, ML +2.75 mm, DV -1.8 mm). One surface electrode (stainless steel watch screw, 1x3 mm) was placed over the left parietal cortex (AP -2.0 mm, ML -1.5 mm, DV -) for surface EEG recordings. Furthermore, two surface electrodes were implanted in the skull above the cerebellum for reference and ground.

One 16-Channel silicon probe (A1x16-5mm-100-703-CM16LP, 30x30, thickness: 15 µm, NeuroNexus, 100 µm distance between recording sides) was slowly inserted in the right hippocampus (AP -2.0 mm, ML -1.5 mm, DV -1.9±0.2 mm) in 10 - 50 µm steps using the Micropositioner 2660 (Kopf Instruments). Reference and ground of the 16-Channel probe were connected to the two surface electrodes in the cerebellum. LFPs were recorded online with the 16-Channel probe with an Intan evaluation board RHD2132

(Intan Technologies). To verify the position of the 16-Channel probe during surgery, the temporoammonic pathway was stimulated by a stimulus isolator (World Precision Instruments) using a current of 50 – 200 µA. A steel pin (2.1 mm diameter, 14 mm length) was glued to the skull at an angle of 75° to be able to restrain the mouse head during head-fixed experiments.

After implantation, the electrodes were fixed with a minimal amount of dental cement (Paladur, Heraeus) and the mouse was allowed to wake up under constant monitoring of temperature and breathing rhythm. Mice with implanted electrodes were held in individual cages and injected again with the analgesic Buprenorphine-hydrochloride (0.1 mg/kg) 8 hours after surgery.

2.5 *In vitro* Patch Clamp Recordings

2.5.1 Acute Hippocampal Slice Preparation

For patch clamp experiments, the three weeks previously injected mice were anesthetized with CO_2 and subsequently decapitated. The brain was gently removed from the skull and the cerebellum and the first third of the frontal lobe were discarded. The brain was glued to a cooled cutting chamber of a vibratom (LeicaVT1200S) and 300 µm thick horizontal hippocampal slices were prepared using ice cold (< 4°C) buffer containing the following (in mM): 140 potassium-gluconate, 10 HEPES, 15 sodium-gluconate, 0.2 EGTA, 4 NaCl and calibrated to pH=7.2 with KOH. Afterwards the hemispheres were separated and the slices were incubated for 30 min at 32°C in ACSF containing (in mM): 124 NaCl, 3 KCl, 1.25 NaH_2PO_4, 1.6 $CaCl_2$, 1.8 $MgSO_4$, 10 Glucose, 26 $NaHCO_3$ calibrated with carbogen gas (95 % O_2, 5 % CO_2) to a pH of 7.4 in a submerged slice holder.

After one hour resting time at room temperature, single slices were transferred to a submerged recording chamber, which was constantly perfused with ACSF (3 ml/min) and saturated with carbogen gas at room temperature. Slices were secured with a platinum harp.

2.5.2 Patch Clamp

Patch pipettes were pulled from borosilicate glass pipettes with an outer diameter of 2 mm (GB200F-10, Science Products, Hofheim, Germany) using a Flaming/Brown Micropipette Puller (Model P-1000, Sutter Instruments). The glass electrodes were filled with an artificial intracellular solution containing (in mM): 140 potassium-gluconate, 3 KCl, 4 NaCl, 10 HEPES, 0.2 EGTA, 2 Mg_2ATP, 0.1 Na_3GTP calibrated to pH=7.2 with KOH and with an osmolality of 279 mOsm. Daily prepared 3.0 mg/ml Biocytin (Sigma) was added to the intracellular solution for single cell filling and subsequent staining. The liquid junction potential was +13.5 mV. However, the values shown in this thesis were not corrected for the liquid junction potential. The bath and recording electrodes consisted of chlorided silver wires (Science Products, Hofheim, Germany). The pipette resistance was 2.5 to 4.5 MΩ measured in the bath. Series resistances were compensated by the bridge balance mode of the amplifier (ELC-03XS, npi).

CA1 pyramidal cells expressing either shSCR-mCherry or shVEGFD-mCherry were recorded in whole cell configuration. Their somata were approached under visual control through an upright epifluorescence microscope (BX51WI, Olympus) with a mCherry filter (CY3.5, Chroma) and a Dodt gradient contrast optic to improve the contrast. Cells were visualized with two different water immersion objectives (UMPlanFI 10x/0.30 W ∞/- and UMPlanFI 40x/0.8 W ∞/0/FN26.5 (Olympus)), combined with a Hamamatsu CMOS camera (Digital Camer C11440) using Hokawo 2.9 software. Furthermore, only neurons approximately 70-90 µm deep in the slice were considered in order to avoid a loss of dendrites by the slice cutting process.

In order to prevent clogging by debris, a positive pressure was applied to the patch pipette while moving through the slice. When the pipette was in close proximity of the soma, negative pressure was applied in order to make the cell membrane adhere to the opening of the glass pipette and obtain a giga-seal. The whole cell configuration was obtained by a slight increase in the negative pressure to remove the membrane patch blocking the pipette opening. This configuration produced a continuity between cell and pipette solution and thus allows a sufficient perfusion of the whole cell with Biocytin for subsequent morphological analysis. Pipette capacitance, series capacitance, and whole-cell capacitance were compensated in voltage clamp mode. After 5 min, passive and active membrane properties were measured by injecting different current steps through the patch pipette in current clamp mode. The current steps applied started from -200 pA to +400 pA in 25 pA steps. Close to AP threshold 2 to 5 pA steps were used. Sag amplitude resulting from open I_h channels was elicited by hyperpolarizing steps and action potential firing by depolarizing steps. Measurements were performed by holding the soma at -60 mV (not corrected for liquid junction potential, so in reality at -73.5 mV) via current injection.

The data were sampled at a sampling rate of 20 kHz and a low-pass filter at 8 kHz. All recordings were digitized (Power 1401mkII, Cambridge Electronic Design) and stored on a local computer for further analysis. Under the conditions described above, cells did not fire spontaneous action potentials. Furthermore, only cells with a stable input and access resistance ($\leq$ 15% variation) and an overshooting action potential were included into the analysis. Cells which required a holding current $<$ -200 pA and an access resistance $>$ 20 MΩ were also excluded from the analysis.

After the measurement in current clamp mode, the cell was clamped at -60 mV for 45 minutes to allow the dye to dispense. Then the pyramidal neuron was closed by slowly pulling back the patch pipette until the lipid bilayer closes again and thus a gigaseal was again obtained. Afterwards, the slice was transferred to a submerged slice holder filled with ACSF for 45 min before being fixed in 2% paraformaldehyde (PFA) overnight at 4°C on a shaker (Shaker DOS-10l, NeoLabs) for subsequent stainings (section 2.7).

2.6 *In vivo* Recordings of Local Field Potentials and Evoked Potentials

In vivo recordings were performed after one week from surgery, in order to allow the animal to recover and get used to the weight of the electrodes. During this time, the animals were handled 5 min in the morning and 5 min in the evening in order to habituate them to the experimenter, room, and setups. Recordings were carried out under two conditions: In the animal's homecage and in a custom made head-fixed setup. Prior to the actual recording, one habituation session (1h) in the homecage and in the head-fixed setup was done.

An Intan evaluation board RHD2132 (Intan Technologies) was used to amplify *in vivo* local field potentials (LFPs) and evoked potentials. The system uses three accelerometer channels in order to record the animal's movement in x, y, z-axis. Furthermore, the depth profile in CA1 was recorded (16 Channels) and the surface EEG of the parietal cortex. Data were digitized at 2.5 kHz sampling rate and bandpass filtered with 1-500 Hz. All data were stored on a local computer for further analysis.

2.6.1 Head-Fixed Experiments in Awake Animals

The head-fixed setup was custom built using a stereotaxic apparatus. The mice were fixed to the stereotaxic positioner using the steel pin implanted previously. The mice were placed above a plastic running wheel, which was connected to a sensor in order to measure the running speed. Under this experimental setup, the animals were able to run or stay immobile voluntarily. LFPs and evoked potentials (Stimulus Isolator, WPI) from stimulations of the commissural fiber inputs and the temporoammonic pathway were recorded in both conditions.

An input/output curve was performed to determine the minimum response recorded as a depth profile with the 16-Channel probe in CA1 for stimulations of both inputs separately. 170% of the minimal stimulation strength necessary to evoke a minimal response was used to stimulate commissural fiber and temporoammonic pathway inputs. Subthreshold stimulation was done in order to avoid induction of action potentials and thereby triggering feed-forward inhibition. Stimulation intensity was between 20 µA and 150 µA, depending on the individual animals. In one recording session, each pathway was stimulated every 30 sec for 30 min. Recordings were conducted on each mouse once a day for seven consecutive days Afterward the animals were recorded in their homecage.

2.6.2 Recordings in Freely Moving Animals

In order to record the neuronal activity during awake and sleep phases, recordings in the animal's homecage were conducted. Due to the no stressful condition, long daily recording sessions (3-5 hours) could be carried out while the mouse was able to freely move in its homecage. However, due to movement artefacts, the recordings during active states were not useful.

2.7 Stainings and Microscopy

2.7.1 Fluorescence Staining and Spine Imaging

For spine imaging confocal microscopy was necessary for sufficient resolution. Therefore, a fluorescence staining was performed. PFA fixed hippocampal slices were stained in free-floating conditions one day after patch clamp recordings (section 2.5.2). After being thoroughly rinsed in 1x phosphate buffered saline (PBS) (3x10 min), cells were stained using the Streptavidin-Alexa 488 antibody (1:500, Life Technologies). This was done in a blocking solution containing 0.2% Triton X-100 and 5% Normal goat serum (Vector Laboratories) in 1xPBS at room temperature for 2 hours. In addition, a DAPI staining (Carl Roth, 2 min, 1:10,000) was performed and the slices were mounted in Mowiol.

For spine imaging, a Nikon A1R point scanning confocal microscope (Nikon Imaging Center (NIC) in Heidelberg) with a Nikon N Apo 60x NA 1.4 λs oil immersion objective (working distance 0.14mm, FOV 0.21 x 0.21mm) was used. With an additional 5x digital zoom the x, y-resolution of 0.08 µm was obtained. The z-stacks were acquired with a step size of 0.15 µm. These parameters fulfill the Nyquist theorem and were thus sufficient for subsequent deconvolution of the images.

Spines were imaged in three regions of interest: s. oriens, s. radiatum and s. lacunosum-moleculare. A minimum of eight second or third-degree dendrites per stratum were imaged for further analysis (section 2.8.1).

2.7.2 DAB Staining and Neuron Reconstruction

After spine imaging, the same slices were used for 3,3`-Diaminobenzidine (DAB) staining. This method has several advantages over a fluorescence staining: The staining is very stable and not sensitive to light. Furthermore, this method enhances the signal generating a very high contrast. This allows an exact 3-D reconstruction of the whole neuron (Marx et al. 2012).

After pre-incubation with 2% TritonX-100 and 3% hydrogen peroxide (H_2O_2) for quenching of endogenous peroxidase activity, the avidin–biotinylated horseradish peroxidase (HRP) complex (ABC, Vector Laboratories) in combination with DAB as a chromogen was used. The turnover of the HRP substrates (here H_2O_2 and DAB) results in a brown, insoluble reaction product which is detectable by bright field microscopy. Furthermore, this reaction amplifies the detectable end products of the chromogen and therefore enhances the staining.

For imaging, an Olympus BX53 bright field microscope (camera: Retiga 2000R-F-CLR-12, QImaging, Surrey, Canada) with a Plan N 40x/0.65 ∞/0.17/FN22 objective and the Neurolucida 10 software (MicroBrightField) was used. Several partially obtained images, with a high resolution (0.184 µm x 0.184 µm, z-steps 1 µm) were stitched together to get a single image of the whole neuron. This image was used to manually reconstruct the cell in all three dimensions with the same Neurolucida software mentioned above. Damages of dendrites by the slicing process was clearly visible by blobs at the cutting side. These cells were excluded from the experiment.

Sholl analysis and fractal index analysis were performed on the 3-D model to obtain the length and complexity of apical and basal dendrites (section 2.8.1).

2.7.3 Histology for Verification of *in vivo* Electrode Position

After completion of the *in vivo* recordings, a lesion was performed in order to verify electrode positions in the later histochemical staining (Figure 2-2). The lesion caused a glial scar by the application of a current with a stimulus isolator to the deepest and the most superficial electrode of the 16-Channel probe. Lesioning was carried out under anesthesia with 4% isoflurane as described in section 2.4.

Three days after lesioning the animal was sacrificed using a perfusion protocol. The mice were deeply anesthetized with isoflurane and perfused transcardially starting with 1xPBS followed by 4% PFA. The brain was dissected and stored for three days in 4% PFA at 4°C on a shaker. 40 µm thick coronal slices were cut with a vibratome under light protection to preserve the fluorescence of mCherry (section 2.4.2). Slices were mounted on a microscope slide (Superfrost Plus, Thermo Scientific) and allowed to dry overnight at room temperature. The next day a DAPI staining was performed by using the DAPI containing histology mounting medium Fluoroshield (Sigma).

The position of the 16-Channel probe and stimulation electrodes were verified using an Olympus BX61 microscope with cellSens Dimension 1.7.1 software (Olympus). UPlanFI 4x/0.13 or UPlanFI 10x/0.3 objectives were used in combination with a CCD camera (F-View II, Soft Imaging System). For detection of excitation and emission of mCherry (ex = 552 nm em = 570 nm) and DAPI (ex = 359 nm, em = 461 nm) a Cy3.0 filter cube (Chroma) and U-MNUA2 (Olympus) filter cube were used.

For the *in vivo* experiments, three criteria had to be fulfilled for the electrodes position (Figure 2-2):

1. Location in CA1 of the (right) hippocampus
2. Covering all strata of interest in depth
3. Colocalization with mCherry expression and thus with VEGFD downregulation

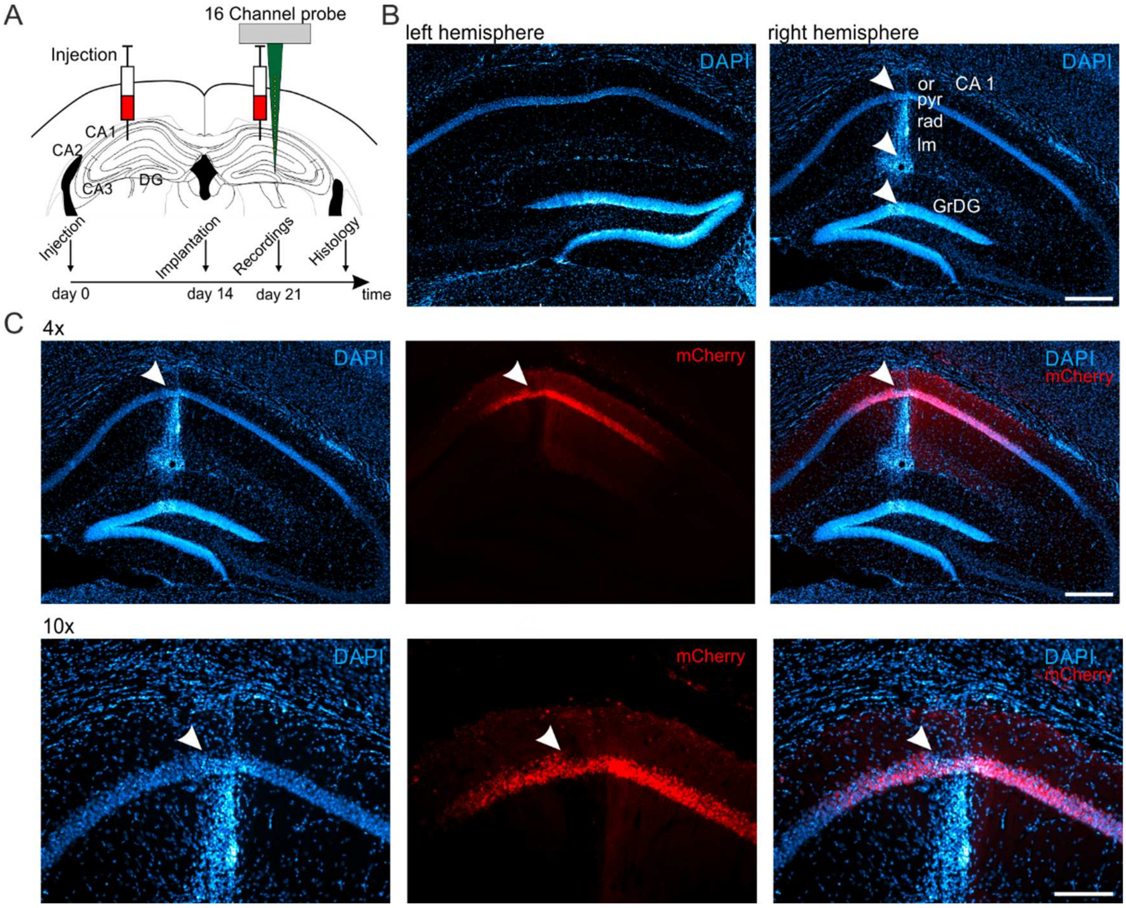
A
16 Channel probe
Injection
CA1
CA2
CA3
DG
Injection
Implantation
Recordings
Histology
day 0
day 14
day 21
time
B
left hemisphere
right hemisphere
DAPI
DAPI
or
CA 1
pyr
rad
lm
GrDG
C
4x
DAPI
mCherry
DAPI
mCherry
10x
DAPI
mCherry
DAPI
mCherry

Figure 2-2. **Verification of 16-Channel probe position and co-localization with mCherry expression. (A)** Schematic representation of *in vivo* experimental procedure. Injection side of either rAAV-shSCR-mCherry or rAAV-shVEGFD-mCherry in the hippocampi of both hemispheres is indicated by the two syringes. A 16-Channel probe was implanted in the right hemisphere 14 days after injection. Recordings started 21 days after injection. **(B)** DAPI staining of the nuclei of cells in coronal hippocampal slices of the left and right hemisphere. Images shown here were acquired after recording completion. The position of the multichannel electrode across the CA1-DG axis was verified in the right hemisphere (white arrowheads). Scale bar 300 µm **(C)** Co-localization of 16-Channel electrode with mCherry expression in CA1 was verified (white arrowheads). Scale bar in the upper panel (4x) = 300 µm, Scale bar in the lower panel (10x) = 150 µm. (or = stratum oriens, pyr = stratum pyramidale, rad = stratum radiatum, lm = stratum lacunosum-moleculare, CA1 = Cornu ammonis 1, GrDG = Granule cell layer of the dentate gyrus).

2.8 Data Analysis

2.8.1 Morphometric Analysis of Dendrites

Sholl analysis and fractal index analysis were performed with the Neuroexplorer 10 software (MicroBrightField).

Sholl Analysis. Sholl analysis is a well established quantitative technique to access morphological characteristics of neurons (Sholl 1953). Concentric spheres are drawn around the cell, starting from the soma (r_0 in Figure 2-3). The spheres increase in size by a constant value (r_Δ). A radius of $r_\Delta = 5$ µm was used in this study. The readout of the Sholl spheres describes the number, characteristics (e.g. diameter) or total length of objects in each shell. A shell does not contain the information from any smaller shell, hence the results are not cumulative.

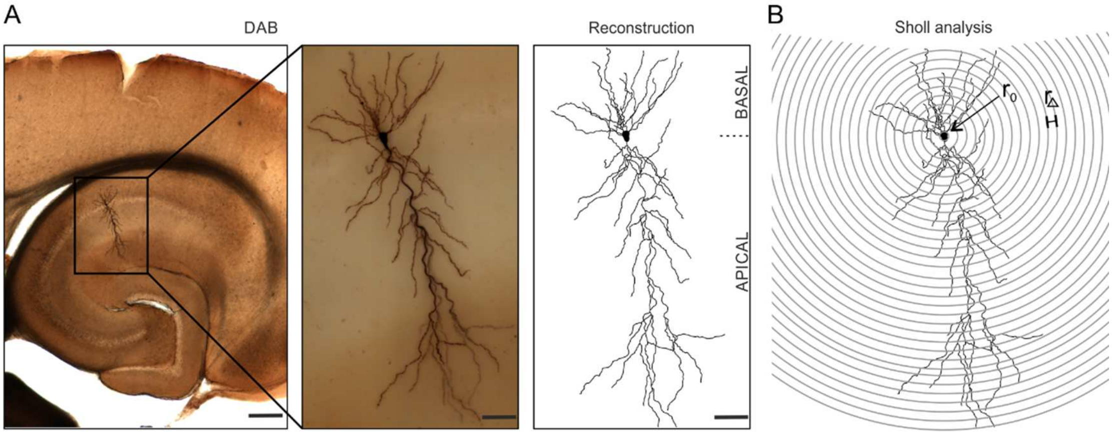

Figure 2-3. **Reconstruction of CA1 pyramidal neurons and analysis of dendritic length by Sholl analysis.** **(A)** Horizontal hippocampal slice with a pyramidal cell in CA1, Scale bar = 250 µm. The cell was filled with Biocytin through a patch pipette and subsequently stained by DAB staining method. This cell was then reconstructed (right panel), Scale bar 50 µm. **(B)** By applying the Sholl method to the reconstruction, dendritic length and other parameters can be analyzed. r_0 represents the starting point of the Sholl spheres. This is usually put in the soma of the cells. $r_\Delta = 5$ µm represents the radius of the single Sholl spheres.

For reliable comparison of apical dendritic structures between slices and animal in the s. radiatum and s. lacunosum-moleculare, cells were normalized to the respective hippocampal slice dimensions (Figure 2-4). Sholl proposed this adjusted method for analysis of the apical tree of pyramidal cells in a similar way (1953 in Text-fig. 3).

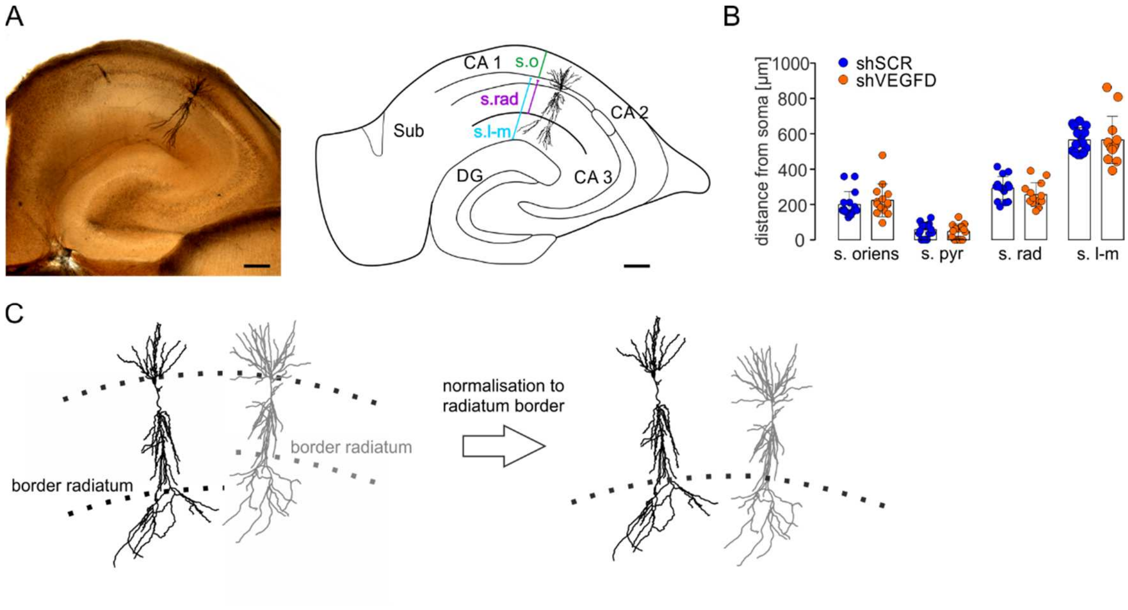

Figure 2-4. **Hippocampal dimensions and normalization of Sholl spheres to the s. radiatum boarder. (A)** Horizontal hippocampal slice with a pyramidal cell in CA1, Scale bar 200 µm. The cell was filled with Biocytin through a patch pipette and subsequently stained by DAB staining method. In the right panel, a schematic after drawing of the slice containing the reconstructed CA1 cell is shown. Subareas of the hippocampus and sublayers of CA1 are indicated (CA1 = Cornu ammonis 1, CA2 = Cornu ammonis 2, CA3 = Cornu ammonis 3, DG = Dentate Gyrus, Sub = Subiculum. or = stratum oriens, pyr = stratum pyramidale, rad = stratum radiatum, lm = stratum lacunosum-moleculare,). **(B)** Hippocampal dimensions are not significantly different between the two groups (SCR versus VEGFD). **(C)** The measured individual border between stratum radiatum and stratum lacunosum-moleculare from every slice and cell was used to compare the dendritic length from the Sholl analysis for stratum radiatum and stratum lacunosum-moleculare.

Fractal Index. The fractal analysis describes the way in which objects fill space. In this study, the objects are the 3-D reconstructed CA1 pyramidal cells. A fractal object reveals more details as the magnification of the view increases. Hence, fractal analysis addresses quantities being dependent on scale and the aim is to find a connection between the measured value and the scale at which the measurement is taken. Here the box counting method was applied. This method uses nested cubes. Any cube can be divided into 8 smaller cubes until infinity, therefore the number of cubes grows exponentially. At every stage of cube subdivision, the number of cubes that contain part of the object is counted (Figure 2-5,A). The log base 8 from the total number of cubes and of the number of cubes containing objects is taken. Plotting these values reveals a straight line for fractal objects. The slope of the straight line is the fractal dimension of the object and reveals how the object increases in detail as magnification increases (Panico and Sterling 1995; Figure 2-5,B).

The box counting method uses linear regression to calculate the fractal dimension:

$$k - \dim(X) = \lim_{q \to 0} \frac{log_2(Q_q(X))}{-log_2(q)} \qquad \text{Equation 2-1}$$

$Q_q(X)$ = number of boxes

$$k - \dim(X) = \frac{n * \sum_{i=1}^{n} x_i y_i - \sum_{i=1}^{n} x_i \sum_{i=1}^{n} y_i}{\left[\sum_{i=1}^{n} x_i\right]^2 - n * \sum_{i=1}^{n} x_i^2} \qquad \text{Equation 2-2}$$

x = base 2 log of q

y = number of boxes counted

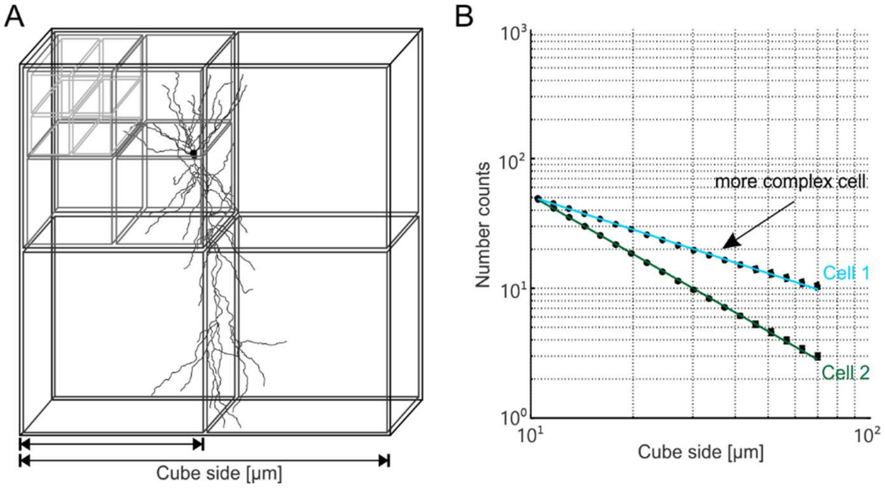

Figure 2-5**. Analysis of dendritic complexity by the fractal index method. (A)** A representative 3-D reconstruction of a CA1 pyramidal cell within a schematic representation of the box counting method, which was applied to calculate the Fractal index for every neuron. By making the cube side of the boxes smaller, the complexity of the neuron can be accessed. At every stage of cube subdivision (visualized by different shades of grey), cubes containing dendrites were counted. **(B)** Plotting the log base 8 from the total number of cubes against the number of cubes containing objects reveals a straight line for fractal objects. The slope of the straight line is the fractal dimension of the object and reveals how the object increases in detail as magnification increases.

2.8.2 Morphometric Analysis of Dendritic Spines

When an image is formed by an optical system like a microscope it suffers from degradation by noise and blurring. The degradation of an image by these physical processes is called convolution. Noise is mainly due to photon noise. Blurring is due to the diffraction pattern (=airy disc) of a point source. The diffraction pattern in 3-D is called point spread function (PSF). The PSF defines the resolution in x, y, and z. As a conclusion, in fluorescence microscopy, an image can be described by the sum of the

PSFs. That means, deconvolution restores the image, which is suffering from the PSF, by collecting the spread light and calculate the source of it in order to produce a better representation of the original image. In conclusion, deconvolution increases the signal to noise ratio, increases mainly the axial resolution and reduces background. A requirement for deconvolution is that images are Nyquist sampled in x, y, and z.

Increasing the resolution of the confocal images by deconvolution allowed the reliable detect, count and classify spines. Deconvolution was done with a theoretical PSF by using the Huygens software (Huygens Remote Manager v3.0.3, SVI, access provided by the NIC).

The analysis of the total spine density and the different spine types was done with NeuronStudio software (ver. 0.9.92, Computational Neurobiology and Imaging Center Mount Sinai School of Medicine, New York, NY). Spine density was calculated for 20 µm dendritic length. Spine density from the minimum of eight dendrites was averaged for every layer separately and displayed as mean±SD. The parameters to detect spines along the dendrites and classify them were the following:

Detection:	Min height: 0.25 µm Max height: 2 µm Max width: 2.5 µm
Classification:	Head/Neck $<$ 1.1 µm, Length/Head $<$ 2.5 µm Head/Neck $>$ 1.1 mm, length/head $>$ 2.5 µm Head Ø $>$ 0.35 µm

2.8.3 *In vitro* Patch Clamp Recordings

Signal (Version 4.11, Cambridge Electronic Design) and Python (Version 2.7) were used to analyze the data acquired by current clamp recordings in whole cell configuration (section 2.5.2).

For action potential firing threshold determination, the first action potential with the minimal current injection was analyzed. The first derivative was calculated from the voltage trace and action potential firing threshold was defined by a 10 mV/ms threshold for the first derivative (Henze and Buzsáki 2001).

The input resistance (R_{input}) of each cell was calculated applying Ohm`s law, which defines it as the quotient of the voltage deflection (U) divided by the current injection (I; Equation 2-3).

$$R_{input} = \frac{U}{I} \qquad \text{Equation 2-3}$$

The time constant tau (τ) describes the time (in seconds) it takes to adapt the membrane voltage to a current input. For a neuron, this parameter defines the time it takes for the current input to hyper/depolarize the cell to 1/e (~36.8%) or $1 - \frac{1}{e}$ (~63.2%) of the final voltage value. In this study, τ was derived from an exponential curve, fitted to the voltage responses to several current injection steps (Equation 2-4).

$$\tau = R * C \rightarrow C = \frac{\tau}{R} \qquad \text{Equation 2-4}$$

The capacitance (C) was calculated by the rate and amplitude changes of voltage responses to hyperpolarizing current steps (Equation 2-4).

For the analysis of the voltage sag, a depolarizing membrane response through activation of I_h, was elicited by hyperpolarizing current steps injected to the soma. Measurements were performed by holding the soma at -60 mV through somatic current injection. The ratio of V_{min} (maximum peak of voltage sag response (Figure 3-3,B) and V_{sag} was computed by calculating the slope of the regression line (Figure 3-3,E).

2.8.4 *In vivo* Recordings

Data was stored offline and analyzed using built-in and custom-written Matlab routines (Matlab 2011, The Mathworks Inc., Natick, MA). To compare recordings from the same layers between different animals, the channels were aligned by the pyramidale layer. The channel, positioned in s. pyramidale, was identified by the following criteria (J Brankack, Stewart, and Fox 1993; György Buzsáki 2002):

- Spontaneous LFP patterns (e.g. first theta phase reversal)
- Current sources and sinks identified by evoked potentials in response to stimulation of commissural fibers and temporoammonic pathway
- *Post hoc* histological identification of anatomical position
- Maximum ripple energy

From the channel located in s. pyramidale two more channels in the direction of the alveus were used for s. oriens analysis and four channels in the direction of the fissure for analysis of s. radiatum and s. lacunosum-moleculare. In summary, 16 channels were recorded, though, seven channels spanning through the entire CA1 were sufficient to capture network oscillations in all layers where dendritic changes occurred after the VEGFD knockdown. Data from all animals were structured starting from the deepest channel (s. oriens) towards the superficial channels (s. lacunosum-moleculare). The spacing of recordings sides was 100 µm. Data between recording sides were interpolated by a spline function. Z-scores were calculated by dividing the values by the mean values of each channel in each animal.

Behavioral Staging. Staging of vigilance states was done manually. 30 seconds of each vigilance state per animal were collected.

Under the head-fixed condition, running was identified by the sensor attached to the running wheel. Immobility in the head-restrained setup was defined as the absence of a running signal or movement signal recorded by the sensor or the accelerometers, respectively.

In the homecage the signal from the accelerometers was used to identify movement (waking > NonREM, REM). Furthermore, the amount of high amplitude slow wave activity (NonREM > REM) and the amount of regular theta activity (REM > NonREM) were used as parameters (Jurij Brankack et al. 2010). Due to high movement and cable artefacts, only sleep states were analyzed from freely moving animals in the homecage.

Theta and Gamma LFPs and CSD Depth Profiles. For depth profile recordings, theta cycles were aligned by their peak across the 16 channels of the probe. Recordings from the s. lacunosum-moleculare served as reference since theta oscillations are there most regular in frequency and large in amplitude (J Brankack, Stewart, and Fox 1993; György Buzsáki 2002). The peaks in the reference channel were used as a trigger to identify theta peaks in other channels. Theta amplitudes were then computed by a Hilbert transform using the Matlab built-in *hilbert.m* function. Next, theta peaks served as triggers to averaged n > 50 theta cycles in each channel. The averaged signals were plotted as voltage depth profiles.

Furthermore, the current source density (CSD) was computed from the voltage profiles. The one-dimensional CSD maps were calculated for one direction (depth) as the second local derivative from the LFP (C. Nicholson and Freeman 1975). The small resistance differences in the extracellular matrix between CA1 layers can be neglected since they do not influence the spatial distribution of sources and sinks and thus it can be assumed that the resistance of the extracellular matrix is homogeneous and isotropic (Holsheimer 1987). Both datasets were plotted as mean±SEM.

The same procedure was performed for gamma frequency (35-70 Hz).

Spectral Analysis. The power spectral density (PSD) of theta waves during REM sleep and running behavior was analyzed by the means of Welch periodogram method (50% overlapping, 4-s Hamming windows) using the *pwelch.m* function from the Signal Processing Toolbox in Matlab. Theta frequency band was defined as the highest power peak between 4-10 Hz. This was plotted as a function of depth as mean±SEM.

Gamma Amplitude. Based on the dataset, gamma bands were defined as follows: 35-70 Hz, 70-120 Hz and 120-160 Hz. First, the raw signal was filtered using this frequency bands. Next, the complex Hilbert transform was applied to extract the time series of the amplitude envelope of the three filtered signals. Finally, the mean amplitude as depth profile was computed.

Cross-Frequency Coupling (CFC) of Theta and Gamma. Neuronal oscillations can interact with each other in different ways. The interaction is called cross-frequency coupling (CFC). Two ways of modulation were analyzed: (1) The modulation of the amplitude of a fast oscillation (gamma) by the phase of a slow oscillation (theta, 4-10 Hz) and (2) the phase-phase/amplitude coupling between theta and gamma.

To measure the phase - amplitude coupling strength, the modulation index (MI) was computed as described by Adriano B. L. Tort et al. (2010). In short, this has been done as follows:

Raw signals were filtered for the slower, theta rhythm (4-10 Hz) and two distinct gamma bands (gamma$_s$ (35-70 Hz) and gamma$_f$ (120-160 Hz)). The time series of the filter signals for phase (theta) and amplitude (gamma) were computed by the complex Hilbert transform. The composite time series gives the amplitude of gamma at each phase of the theta rhythm. The phase of the slower frequency was binned in 18 intervals of 20° each and the mean amplitude of the fast frequency in the bins was determined. By normalizing the mean gamma amplitude in each phase bin, the sum over all phase bins equals one. This results in a phase – amplitude distribution. A uniform distribution means that the gamma amplitude is not modulated for all theta phases, so there is no coupling (MI value towards 0). The further away the distribution gets from the uniform distribution, the higher the coupling (MI value towards 1). The MI reflects the divergence of the phase-amplitude distribution from the uniform distribution. The MI of all frequency band values are plotted in a comodulogram. The cold pseudocolors show weak coupling, whereas warm colors represent strong coupling.

To calculate the phase-phase/amplitude coupling, the phase-amplitude distribution of theta and gamma was used to compute the mean angle of this distribution.

Sharp Wave-Ripple Analysis. Sharp wave-ripples (SWR) were detected as described elsewhere (Allen et al. 2012). Briefly, SWR epochs were detected on the one channel out of the 16 channel of the silicon probe located in the CA1 pyramidal cell layer. This channel was determined as described in section 2.8.4. Ripples were extracted from the raw LFPs with a bandpass filter in the frequency range of 120–250 Hz. A channel located outside the CA1 pyramidal cell layer served as a reference channel to eliminate contamination of the detection by muscle artifacts. The power (root mean square) was calculated in 20 ms time windows (10 ms between windows) and a window with a power larger than 4 SD above the mean was considered as part of a SWR epoch. The epoch extended in both directions until a time window with a power below 2 SD above the mean was encountered.

The detected ripple events were aligned by the troughs and averaged for analysis of the number of SPW events/second, the number of ripple cycles/SPW and the ripple energy/SPW. The ripple energy was calculated as the quadratic sum of all values within the ripple window. This was normalized by the sampling rate. Furthermore, a ripple LFP and the corresponding CSD depth profile were computed. The CSD maps were constructed by filtering the CSD signal (120–250 Hz) and then averaging this filtered CSD, triggering on the troughs of ripples.

Depth Profiles of Evoked Potentials. Data from the fifth head-fixed session was used from all animals (meaning day 12 after surgery). 30 − 60 events were aligned across channels by the stimulation artefact and averaged for every channel separately. From this voltage profiles, the second local derivation (Current source density analysis (CSD)) was computed. CSDs were computed as a function of depth to determine current sources and sinks in CA1 as response to the stimulation of either the temporoammonic pathway or the commissural fibers.

2.9 Statistics

Each set of experiments contained mice injected with either shSCR or shVEGFD viruses. Experiments, and as far as possible, data analysis were carried out in a blinded experimental design.

For the different parameters analyzed in the *in vivo* experiments, each animal contributed one LFP recording. To avoid bias by data length, 30 seconds of each vigilance state per animal were collected. The different behavior states had to be clearly staged (section 2.8.4) and the data were free of any artefacts.

Prism (GraphPad) was used for plotting data and statistical analysis. Depth profile data and Sholl analysis data were plotted as mean±SEM and a multiple Student`s t-test followed by a Sidak-Bonferroni test were applied. For the $\mathrm{CFC}_{\mathrm{P\text{-}P/A}}$ the statistics were computed by the circular statistics toolbox in Matlab. Here, the length of the mean vector was compared. Other data plots represent median±SD and an unpaired Student`s t-test was applied.

3 Results

3.1 Morphometric Data and Single Cell Recordings

3.1.1 Changes in Dendritic Geometry following VEGFD Knockdown

Mauceri et al. (2011) showed that the growth factor VEGFD is involved in the maintenance of the dendritic tree of pyramidal cells in cell culture. Furthermore, the authors showed the regulatory effect of VEGFD for basal dendrites of CA1 pyramidal cells in mouse hippocampal slices. In this study, the first step was to examine the regulatory effect of VEGFD on basal and apical dendritic trees in CA1 pyramidal cells in hippocampal slices. To investigate this, VEGFD was downregulated in both hemispheres of the hippocampus, as described by Mauceri et al. (2011) and in section 2.2 and 2.4 (Figure 3-1,A). In order to avoid any upstream network effect on the CA1 local network, e.g. by CA3 or DG, only mice expressing mCherry exclusively in CA1 were used for experiments (Figure 3-1,A). After filling mCherry positive cells with Biocytin through the patch pipette (section 2.5.2), the slices were post-processed for DAB staining and cells were manually reconstructed in 3-D (section 2.7.2). Representative cell reconstructions of the VEGFD downregulated group (shVEGFD) and the control group (shSCR) are depicted in Figure 3-1,B.

Basal (s. oriens) and apical (s. radiatum and s. lacunosum-moleculare) dendritic morphology was accessed in three ways. First, the total dendritic length was evaluated. Second, by the analysis of dendritic length as a function of distance from the soma and third by assessing the complexity of the dendrites using the fractal index. These analyses were performed for either of the two dendritic compartments (basal or apical) and for the entire dendritic tree (basal + apical).

Dendritic length of the basal and apical branches was investigated by Sholl analysis (Section 2.8.1). This morphometric analysis revealed a significant reduction of basal dendritic length after VEGFD downregulation compared to the control group (shSCR) when dendritic length was analyzed as a function of distance to soma. The reduction was most prominent 20 – 120 µm away from the soma (Figure 3-1,C). The total length of basal dendrites revealed a reduction in shVEGFD neurons, as well (mean shSCR = 2092.68 µm, mean shVEGFD = 1596.58 µm, Figure 3-1,D). The decrease in fractal index values for basal dendrites revealed a less complex basal dendritic tree of shVEGFD cells and thus further confirmed the Sholl analysis findings (mean shSCR = 1.19, mean shVEGFD = 1.08, Figure 3-1,F).

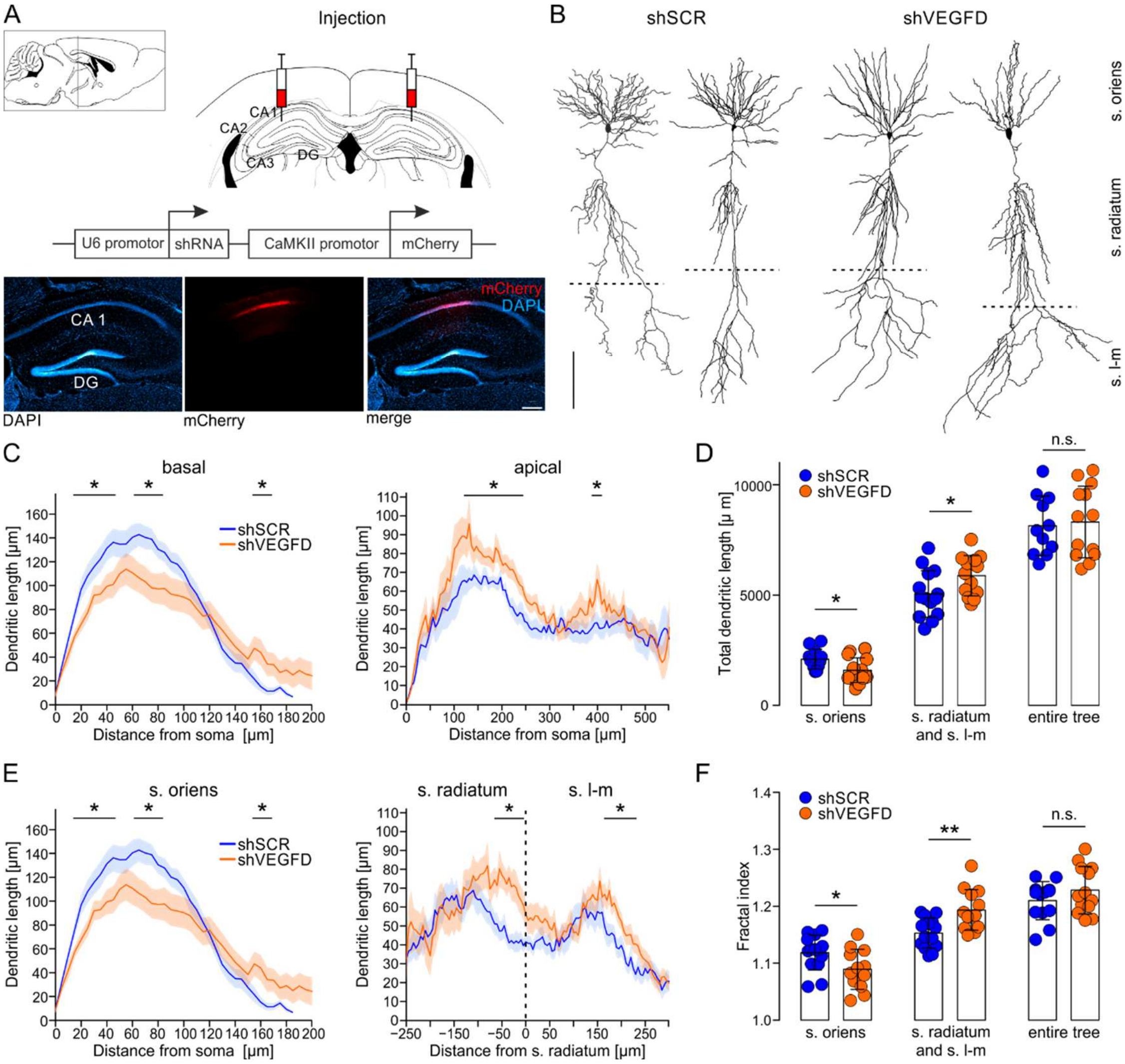

Figure 3-1. **VEGFD downregulation causes a decrease of length and complexity of basal dendrites and increase of length and complexity of apical dendrites in CA1 pyramidal cells.** **(A)** Schematic representation of the side of injection into the hippocampus of both hemispheres and rAAV vector used for shRNA expression. The images show representative mCherry expression of one hemisphere. In the left panel are the nuclei of cells visualized by DAPI staining shown. In the middle panel is the mCherry fluorescence shown and in the right panel the merged images. Scale bar 300 µm. **(B)** Representative reconstructions of CA1 pyramidal neurons of the control group (shSCR) and the shVEGFD group. The dashed line indicates the individual border between s. radiatum and s. lacunosum-moleculare, which was used for normalization. Scale bar = 100µm. **(C)** Quantification of dendritic length as a function of distance from soma of basal and apical dendritic trees by Sholl analysis. Thick lines represent mean±SEM. Multiple Student`s t-test. **(D)** Analysis of the total dendritic length by Sholl analysis for basal, apical and the entire dendritic trees. Bar plots represent mean±SD. Unpaired Student`s t-test. **(E)** Quantification of dendritic length as a function of distance to soma for basal dendrites (same plot as in D) and as a function of distance to s. radiatum border for apical dendrites. Thick lines represent mean±SEM. **(F)** Quantification of dendritic complexity by the fractal index for basal, apical and the entire dendritic trees. Bar plots represent mean±SD. Unpaired Student`s t-test, n.s. = not significant, $* < 0.05$, $** < 0.01$, shVEGFD: $n_{\text{cells}} = 15$, $n_{\text{animals}} = 9$; shSCR: $n_{\text{cells}} = 15$, $n_{\text{animals}} = 8$

The Sholl analysis of the apical dendritic tree revealed the opposite result. After VEGFD knockdown, apical dendrites branching into s. radiatum and s. lacunosum-moleculare exhibited longer dendrites. Apical dendritic trees showed for both groups the typical bimodal structure for CA1 pyramidal cells, validating the intact basic properties of the dendritic tree. The Sholl analysis as a function of distance to the soma showed a specific increase in length around 100 – 250 µm and around 375 – 425 µm away from the soma (Figure 3-1,C). Furthermore, the total apical dendritic arbor increased in length in shVEGFD neurons (mean shSCR = 5052,16 µm, shVEGFD = 5878,72 µm, Figure 3-1,D). The analysis of the fractal index for the apical dendrites showed an increase in complexity following VEGFD downregulation (mean shSCR = 1.15, mean shVEGFD = 1.19, Figure 3-1,F).

The examination of the length of entire dendritic tree, meaning basal and apical dendrites together, revealed no significant difference in the total length (mean shSCR = 8139 µm, mean shVEGFD = 8311 µm, Figure 3-1,D). This was confirmed by the fractal index analysis, which showed no difference in complexity among groups (mean shSCR = 1.21, mean VEGFD = 1.22, Figure 3-1,F). The total width of the hippocampal layers in the slices were not significantly differences between animals, proving that the effect is not due to a bias by distinct layer widths (Figure 2-4,B).

Sholl analysis can be used to investigate the length of basal dendrites, however, it can cause false results for the apical tree as explained in Figure 2-4. To confirm the results for the apical tree from the Sholl analysis, the values were analyzed starting from the s. radiatum to s. lacunosum-moleculare boarder (Section 2.8.1). This validated the results shown in Figure 3-1,D since it showed an elongation of dendrites in the s. radiatum (from 0 µm to -250 µm) and s. lacunosum-moleculare (from 0 µm to +250 µm, Figure 3-1,E).

In summary, following RNAi mediated VEGFD downregulation in CA1 pyramidal neurons, basal dendrites became shorter and less complex. These results validated the findings from Mauceri et al. (2011). The apical dendrites showed an opposing effect. Apical dendrites increased in length and were more complex in VEGFD knockdown cells, especially in areas with high synaptic input in s. radiatum and in s. lacunosum-moleculare.

3.1.2 Spine Density after VEGFD Downregulation

Spines provide the location for excitatory synapses and they arise along the dendrites of pyramidal cells. Since dendritic length was altered after VEGFD downregulation, dendritic density could be affected as well. Further, dendritic spine loss has been shown to be closely associated with cognitive decline in animal models (Scheff et al. 2006). Thus dendritic spine loss could correlate with the long-term memory deficit in VEGFD knockdown mice (D Mauceri et al. 2011). To analyze spine density, Biocytin filled cells were stained with a Streptavidin-Alexa488 antibody. This step was included in the protocol before the DAB staining. Since the Avidin-Biocytin binding is stronger in the DAB staining than the binding in the fluorescence staining it is possible to do both stainings. This strategy allows investigating dendritic morphology, spine density, and functional properties via patch clamp recordings (Section 3.1.3) within the very same neuron.

Z-stack images were acquired in the s. oriens for basal dendritic spines, s. radiatum for proximal, apical dendritic spines and s. lacunosum-moleculare for distal, apical dendritic spines. A minimum of eight dendritic segments of second or third-order oblige dendrites were imaged (Figure 3-2,A). Representative dendritic branches from the three areas of interest are depicted in Figure 3-2,B. The spine density was calculated for 20 µm dendritic length. The quantification of total spine density for s. oriens (mean shSCR = 31.3 No./20 µm, mean shVEGFD = 24.7 No./20 µm), s. radiatum (mean shSCR = 31.2 No./20 µm, mean shVEGFD = 26.5 No./20 µm) and s. lacunosum-moleculare (mean shSCR = 20 No./20 µm, mean shVEGFD = 18.5 No./20 µm) revealed no significant changes between the two groups (Figure 3-2,C).

Furthermore, spines were classified into three distinct groups and the density was calculated in all three layers of interest (Figure 3-2,D). The small and thin spines were classified by a head/neck ratio of < 1.1 and a length/head ratio < 2.5. This spine type showed no difference between shSCR and shVEGFD cells in s. oriens (mean shSCR = 9.5 No./20 µm, mean shVEGFD = 9 No./20 µm), s. radiatum (mean shSCR = 8.6 No./20 µm, mean shVEGFD = 8.7 No./20 µm) and s. lacunosum-moleculare (mean shSCR = 6.6 No./20 µm, mean shVEGFD = 5.6 No./20 µm). Thin, but longer spines were characterized by a head/neck ratio of > 1.1 and a length/neck ratio of > 2.5. The data indicated no effect of VEGFD downregulation on this spine class in s. oriens (mean shSCR = 14.5 No./20 µm, mean shVEGFD = 10.1 No./20 µm), s. radiatum (mean shSCR = 13.5 No./20 µm, mean shVEGFD = 9.9 No./20 µm) and s. lacunosum-moleculare (mean shSCR = 7.2 No./20 µm, mean shVEGFD = 7.7 No./20 µm). The third spine class was characterized by a big head diameter (head Ø > 0.35 µm). The spine density was not affected by VEGFD downregulation in s. oriens (mean shSCR = 6.5 No./20 µm, mean shVEGFD = 5.1 No./20 µm), s. radiatum (mean shSCR = 8.8 No./20 µm, mean shVEGFD = 7.5 No./20 µm) and s. lacunosum-moleculare (mean shSCR = 6.0 No./20 µm, mean shVEGFD = 4.6 No./20 µm.

In summary, the total spine density along basal and apical dendrites was not affected by VEGFD knockdown (Figure 3-2,C). This result confirmed the finding from Mauceri et al. (2011). Furthermore, the density of distinct spine types, classified according to the head diameter, the ratio of Head/Neck and the ratio of Length/Neck, revealed no significant difference in all three classes when shVEGFD neurons were compared to shSCR neurons (Figure 3-2,D).

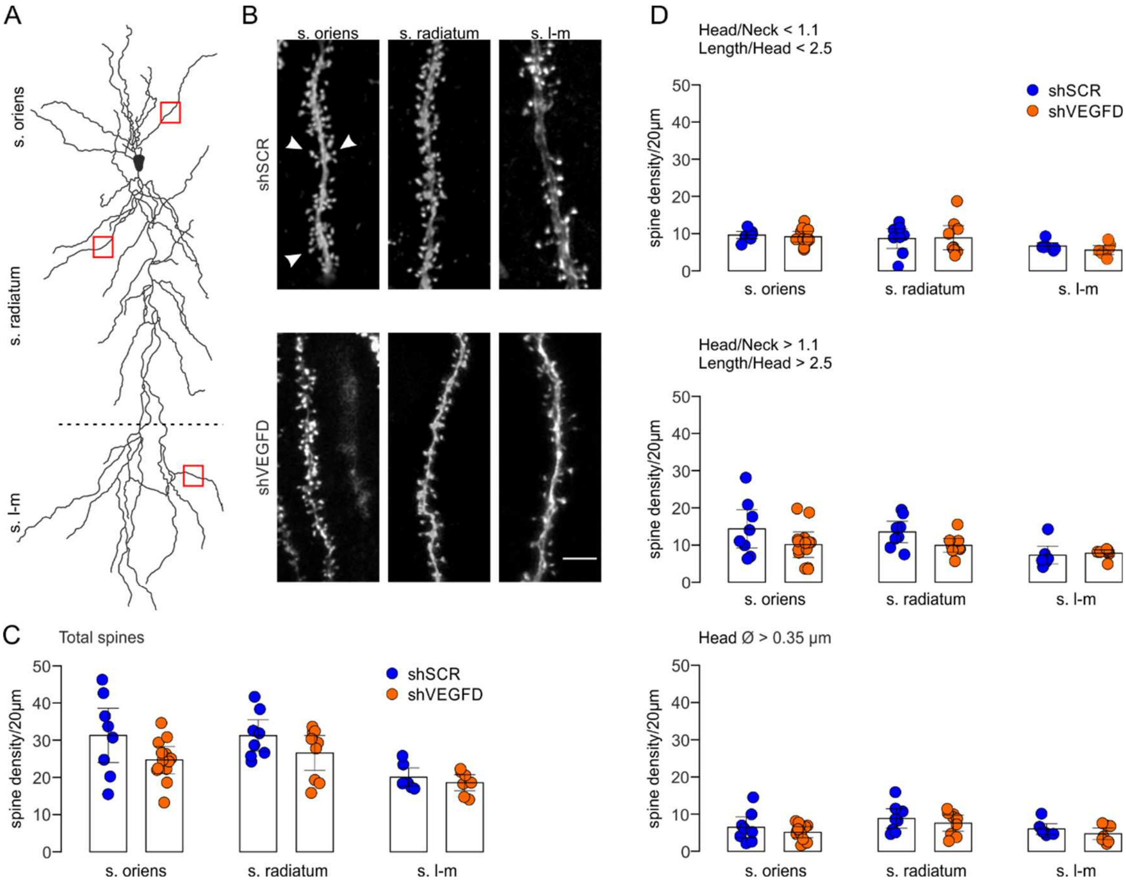

Figure 3-2. **Spine density is not altered by VEGFD downregulation. (A)** Schematic representation of a CA1 pyramidal cell. The dashed line indicates the border between stratum radiatum and stratum lacunosum-moleculare. The red squares indicate the oblige dendrite position, where spines were imaged. **(B)** Representative dendritic branches imaged in stratum oriens, stratum radiatum, and stratum lacunosum-moleculare by confocal microscopy for the control group (shSCR) and shVEGFD group. Spines are indicated by arrowheads. Scale bar = 3 µm. **(C)** Quantification of spine density per 20 µm dendritic length. Bar plots represent mean±SD. **(D)** Spine classification was performed by using the parameters indicated in every panel. Bar plots represent mean±SD. Unpaired Student`s t-test, n.s. = not significant, shVEGFD n = 12 cells, shSCR n = 8 cells.

3.1.3 Passive and Active Functional Single Cell Properties *in vitro* Following VEGFD Knockdown

The output of a neuron, the action potential, is the result of the synaptic integration of signals arriving at different compartments along its dendrites. Synaptic integration and action potential firing depend on resting and active properties of the membrane. Dendritic morphology influences the active and passive electrical properties of neurons. Therefore, functional properties of single cells after RNAi mediated VEGFD knockdown were recorded in whole cell configuration in current clamp (Figure 3-3,A). By injecting first hyperpolarizing and then depolarizing current steps via the patch pipette, the voltage response of the cell and thus passive and active properties were measured.

Resting Membrane Properties. The capacitance of a cell is defined as how much electrical charge (Q) can be stored at a given potential (U) on their surface (Equation 3-1). Therefore, the membrane capacitance is proportional to the cell surface area and is commonly used as an estimation of cell size. Following VEGFD downregulation in CA1 pyramidal neurons, an altered dendritic morphology was observed that could affect the cell capacitance.

$$C = \frac{Q}{U} \qquad \text{Equation 3-1}$$

The membrane capacitance was calculated in current clamp (section 2.8.1). This method was shown to be more precise compared to the measurement in voltage clamp (Golowasch et al. 2009). The comparison between capacitances of shSCR (median: 144.3 pF) and shVEGFD cells (median: 139.15 pF) revealed no significant difference (Figure 3-3,C). Thus, it confirms the result of the fractal index and Sholl method for the entire neurons, which did not show a difference in dendritic complexity or length (Figure 3-1,D and E).

The input resistance of neurons is defined as how much current flows across the membrane at a certain voltage. Thus, the input resistance of a neuron defines the impact of synaptic input currents onto the resting membrane potential. Since leaky dendrites loos current, they show a smaller voltage response as dense membranes. The calculation of the input resistance of shVEGFD neurons revealed a significantly higher resistance in shVEGFD neurons compared to the control (shSCR) group. (median SCR: 106.1 mOhm, median VEGFD: 132.4 mOhm; Figure 3-3,D).

Sag Amplitude Ratio. HCN 1 and 2 channels are non-selective cation channels that carry a current called I_h. As the name implicates, the channels become activated by hyperpolarizing currents and cause a depolarization, thus reducing input impedance and depolarizing the membrane potential. HCN 1 and 2 channels expression is particularly enriched in distal apical dendrites of CA1 pyramidal cells. Since an elongation of distal, apical dendrites in s. lacunosum-moleculare was found after VEGFD downregulation, it could result in more HCN 1 and 2 channels and thus a higher I_h. The channels were activated by hyperpolarizing current steps and the somatic voltage sag was measured (Figure 3-3,E and section 2.8.1). The ratio of V_{min} (maximum peak of voltage sag response; Figure 3-3,B) and V_{sag} was computed by calculating the slope of the regression line (Figure 3-3,E). The slope is not significantly different among groups and thus the voltage sag was not significantly altered in neurons following VEGFD knockdown (median slope: SCR: 0.287, median slope: VEGFD: 0.293; Figure 3-3,E).

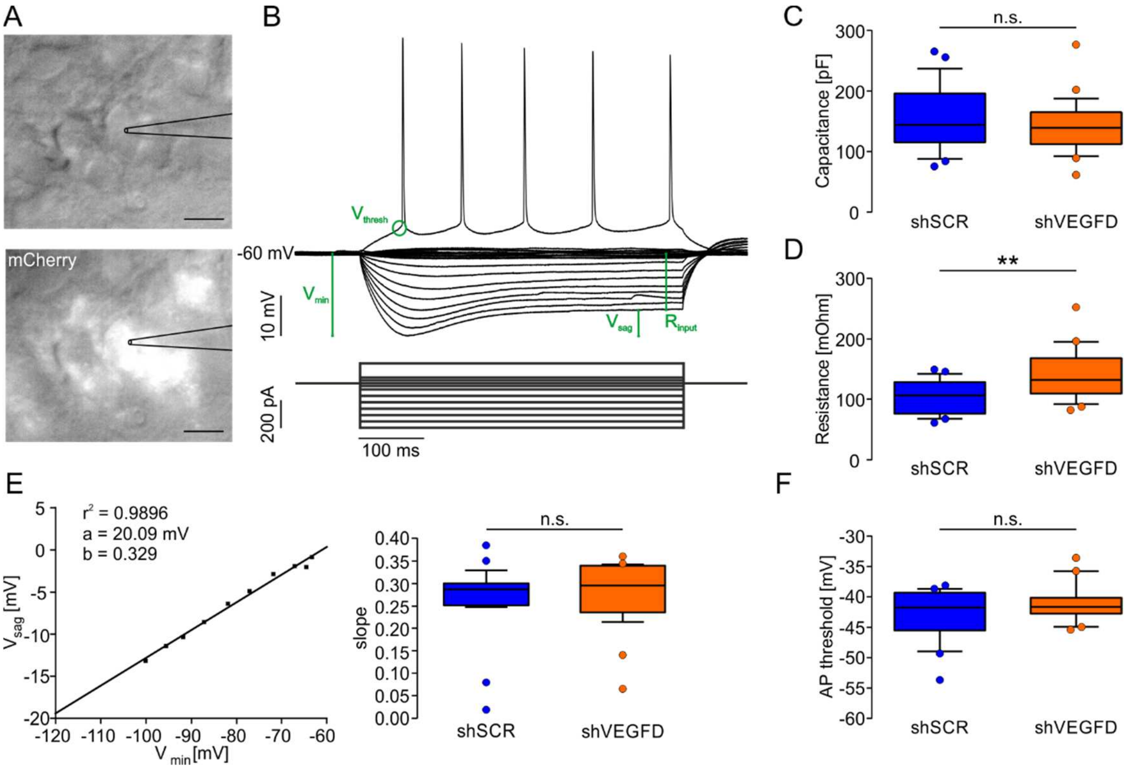

Figure 3-3. **Passive and active membrane properties of shSCR and shVEGFD expressing neurons.** **(A)** Example image of a soma of a CA1 pyramidal cell with a patch pipette. Upper panel is imaged with a Dodt gradient contrast optic. The lower panel image shows mCherry expressing somata. Scale bar = 10 µm. **(B)** Representative voltage trace recorded during somatic current injection of varying strength**.** This was used to determine passive and active properties as indicated in the representative voltage trace. Capacitance shown in **(C)**, sag amplitude shown in **(E)** and AP firing threshold shown in **(F)** were not significantly different between the two groups. The input resistance depicted in **(D)** was increased in shVEGFD cells. Unpaired Student`s t-test, ** < 0.01, shVEGFD: n_{cells} = 23, shSCR: n_{cells} = 25. Boxplots represent median, 25 % and 75 % percentiles (boxes) and 10 % and 90 % percentile (whiskers). (R_{input} = Input resistance, V_{sag} = Sag amplitude**,** V_{min} = Maximum peak of voltage sag response, V_{thresh} = Voltage threshold, AP = Action potential).

Active Properties. The action potential is the major output signal of a neuron, which is generated at the axon initial segment and can be generated as a single or a train of action potentials. Spikes are usually triggered by excitatory postsynaptic potentials that arrive at different dendritic compartments and propagate to the soma (Bean 2007, Spruston 2008). The shorter basal and longer apical dendrites of VEGFD downregulated CA1 pyramidal neurons might influence the relative dendritic inputs or the input integration between the compartments and hence the output of the cell. For induction of an action potential, depolarizing current of increasing steps were injected into the soma (Figure 3-3,B and section 2.5.2) and the membrane potential at which the action potential was initiated was calculated (Section 2.8.1). To avoid bias due to sodium channels activation/inactivation by faster/slower depolarization, we analyzed only the first action potential that was triggered. The analysis revealed no significant difference in action potential firing threshold for shVEGFD cells (median: -41.64 mV) compared to control cells (median: -42.71 mV) as depicted in Figure 3-3,F.

Taken together, the dendritic geometry analysis revealed shorter basal and longer apical dendrites following RNAi mediated VEGFD knockdown. However, the length of the whole dendritic length (basal + apical) did not change. Spine analysis showed no significant difference in spine density in the s. oriens, s. radiatum and s. lacunosum-moleculare. The functional analysis of basic and active single cell properties exhibited no changes in membrane capacitance, sag amplitude, and action potential firing threshold, although input resistance was increased in VEGFD downregulated neurons. Though electrical properties of neurons were similar between VEGFD knockdown and control cells, the changes in dendritic geometry potentially have functional consequences on the neuronal network. Therefore, network oscillations, like theta, gamma, and SPW-R in CA1 under distinct vigilance states were analyzed in the following steps.

3.2 Recordings of Network Oscillations *in vivo*

Dendritic morphology has a strong influence on synaptic integration, propagation of potentials and output generation (Häusser, Spruston, and Stuart 2000; Spruston 2008). Changes in geometry can be physiological or pathophysiological. Indeed, morphological changes are phenomenons often linked to neurodegenerative diseases (e.g. Alzheimer`s disease or memory impairments; Šišková et al. 2014). Mauceri et al. showed cognitive impairments in mice following VEGFD downregulation in the hippocmpus (D Mauceri et al. 2011).

As shown in section 3.1.1 an abnormal change in dendritic length and complexity of basal and apical dendrites in CA1 pyramidal cells was observed following RNAi mediated VEGFD downregulation. To investigate CA1 layer specific correlation between dendritic morphology and function *in vivo*, depth profiles of different network oscillations along the somatodendritic axis at defined vigilance states were recorded. Additionally, two distinct CA1 inputs (commissural fibers and temporoammonic pathway) were stimulated and the evoked potentials analyzed. Table 3-1 summarizes the network oscillations and assocciated vigilance states that have been investigated.

Table 3-1. **Summary of *in vivo* recordings.**

Setup	Vigilance state	Analyzed parameters
Head-fixed	Running	Theta, Gamma oscillations, evoked potentials
	Immobility	SPW-R oscillations, evoked potentials
Homecage	REM sleep	Theta, Gamma oscillations
	nonREM sleep	SPW-R oscillations

To investigate local field potentials (LFPs) and synaptic input along the somatodendritic axis of the CA1 area in VEGFD downregulated mice and control mice (shSCR), a 16-Channel silicon probe was implanted two weeks after virus injection (Figure 2-2,A). The position of the shank electrode was verified during surgery by eliciting typically evoked potentials in response to temporoammonic pathway stimulation and by histology after experiment completion (Figure 2-2,B; section 2.1.1; J Brankack, Stewart, and Fox 1993). The colocalization of the electrode with mCherry expression was verified by light microscopy as shown in Figure 2-2,C.

To compare recordings from the same layers between different animals, the channels were aligned by the pyramidale layer (section 2.8.4). From the channel located in s. pyramidale two more channels in the direction of the alveus were used for s. oriens analysis and four channels in the direction of the fissure for analysis of s. radiatum and s. lacunosum-moleculare. Data from all animals were structured starting from the deepest channel (s. oriens) towards the superficial channels (s. lacunosum-moleculare).

3.2.1 LFP and CSD Depth Profiles of Theta and Gamma Oscillations in VEGFD Knockdown Mice *in vivo*

In order to investigate the effect of shorter dendrites in the s. oriens and longer dendrites in s. radiatum and s. lacunosum-moleculare, theta and gamma voltage profiles were recorded and a current source density (CSD) analysis was performed. Theta waves (4-10 Hz) are most consistently present in REM sleep (Jouvet 1969) and active behavior, described as voluntary, preparatory, orienting and exploratory (Vanderwolf 1969). Gamma oscillations (frequency bands: section 3.2.2) are faster waves nested on the slower theta waves (Bragin et al. 1995). This section addresses theta and gamma oscillations during voluntary running on a treadmill under head-fixed condition and REM sleep in control (shSCR) and VEGFD downregulated (shVEGFD) mice. The behavior was staged using the criteria described in chapter 2.8.4.

During running and REM sleep, the typical theta nested gamma oscillations were observed in control mice as well as in VEGFD downregulated mice (Figure 3-4 andFigure 3-5,C). Theta traces showed, consistently with previous studies, a gradual increase in amplitude along the somatodendritic axis, with a maximum amplitude in s. lacunosum-moleculare. Further, the typical theta phase shift as a function of depth and the phase reversal at s. pyramidale was detected as indicated by the dotted lines in Figure 3-4 andFigure 3-5,C and D (J Brankack, Stewart, and Fox 1993; G. Buzsáki et al. 1986). Gamma oscillations (35-70 Hz) were superimposed on theta waves. Gamma amplitude increased as well as a phase shift occurred with depth. The theta waves in s. oriens and s. pyramidale exhibited a fast upstroke (with positive polarity) and a slower downstroke. Gamma waves were superimposed on the downstroke. However, in s. radiatum and s. lacunosum-moleculare the fast component has a negative polarity and on the slower upstroke are gamma waves present (G. Buzsáki et al. 2003). In conclusion, VEGFD knockdown and control groups showed no differences in theta nested gamma waves during running and REM sleep (Figure 3-4 andFigure 3-5).

This qualitative description of the theta waves was further confirmed by a quantitative analysis of both animal groups (Figure 3-4 andFigure 3-5,D). For analysis of theta oscillations, data was filtered at 4-10 Hz. A minimum of 50 theta cycles/channel were aligned and averaged (section 2.8.4). Two copies of the filtered and averaged theta cycle are plotted for continuity (Figure 3-4 andFigure 3-5,D left panel). Cool colors represent relatively negative values and warm colors represent relatively positive values in the contour map. The relatively negative values during REM sleep showed a peak in s. oriens in both animal groups (shSCR mean = -96 µV, shVEGFD mean = -80 µV). The peaks during REM sleep of the relatively positive values occurred in the s. lacunosum-moleculare (shSCR mean = 412 µV, shVEGFD mean = 401 µV). During running the theta voltage depth profile revealed in both groups a gradual increase with depth and a peak in s. lacunosum-moleculare (shSCR mean = 355 µV, shVEGFD mean = 366 µV). Note the theta phase shift along the axis and the phase reversal in s. pyramidale. Group analysis of shSCR and shVEGFD animals revealed no significant difference in theta oscillations during running and REM sleep in the depth profile (Figure 3-4 andFigure 3-5,D right panel).

The calculation of the second spatial derivative of the theta voltage profile was used to localize the trans-membrane current flow patterns. This is called current source density analysis (CSD) and reveals current sources and sinks, measured by extracellular recordings, along the somatodendritic axis of CA1. In the CSD contour map, the cool colors represent relatively negative values corresponding to sinks and warm colors representing relatively positive values to sources. Note the alternating current sources and sinks at distinct depths along the theta profile during running and REM sleep. The large peaks of identifiable sinks and sources corresponded to the following layers: A sink in s. oriens and s. pyramidale (mean values REM sleep: shSCR = -103 µV/µm^2, shVEGFD = -88 µV/µm^2; mean values running: shSCR = -78 µV/µm^2, shVEGFD = -66 µV/µm^2). Followed by a source in s. radiatum (mean values REM sleep: shSCR = 191 µV/µm^2, shVEGFD = 210 µV/µm^2; mean values running:

shSCR = 81 µV/µm^2, shVEGFD = 160 µV/µm^2) and a smaller sink in s. lacunosum-moleculare (mean values REM sleep: shSCR = -60 µV/µm^2, shVEGFD = -45 µV/µm^2; mean values running: shSCR = -59 µV/µm^2, shVEGFD = -121 µV/µm^2). Sinks and sources in the according layers were recorded in both groups and are consistent with the literature (J Brankack, Stewart, and Fox 1993). The analysis of the CSD depth profile of control animals and VEGFD downregulated animals showed no significant difference during both vigilance states (Figure 3-4 andFigure 3-5,D lower panel).

The same analysis was done for gamma oscillations during running and REM sleep. Oscillations were filtered in the gamma range of 35-70 Hz, aligned and averaged. The gamma LFP depth profile revealed a gradual increase in gamma amplitude with depth, reaching a maximum in s. lacunosum-moleculare (mean values REM sleep: shSCR = 77 µV, shVEGFD = 74 µV; mean values running: shSCR = 107 µV, shVEGFD = 85 µV; Figure 3-4 andFigure 3-5,E upper panel). The CSD showed a sink in s. oriens and s. ppyramidale (mean values REM sleep: shSCR = -11 µV/µm^2, shVEGFD = -10 µV/µm^2; running: shSCR = -15 µV/µm^2, shVEGFD = -18 µV/µm^2) a source in s. radiatum and s. lacunosum-moleculare (mean values REM sleep: shSCR = 26 µV/µm^2, shVEGFD = 43 µV/µm^2; mean values running: shSCR = 49 µV/µm^2, shVEGFD = 45 µV/µm^2). The voltage and CSD depth profiles of gamma analysis revealed no difference between VEGFD knockdown and control (shSCR) mice (Figure 3-4 andFigure 3-5,E right panels).

In summary, theta and gamma oscillations were not affected by shorter basal and longer apical dendrites throughout the CA1 layers. LFP recordings and analysis of current sources and sinks revealed no significant differences between VEGFD downregulated animals and controls.

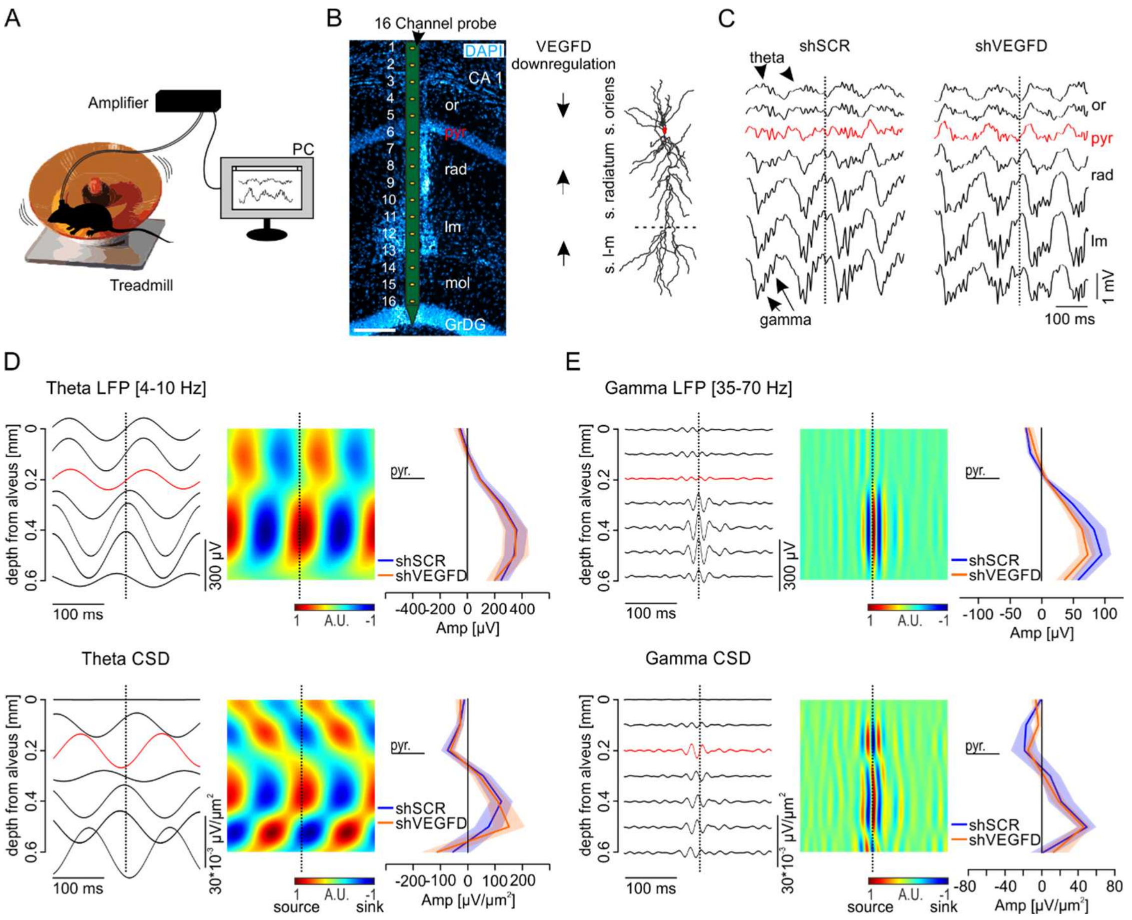

Figure 3-4. **Depth profile of theta and gamma LFP recordings and CSD depth profile during voluntary running on a treadmill reveals no change following VEGFD downregulation.** **(A)** Schematic representation of the head-fixed setup showing a mouse running on a treadmill while recording LFPs. **(B)** 16-Channel probe superimposed on the histologically recovered track in CA1 spanning throughout all CA1 layers (or = stratum oriens, pyr = stratum pyramidale, rad = stratum radiatum, lm = stratum lacunosum-moleculare, CA1 = Cornu ammonis 1, GrDG = Granule cell layer of the dentate gyrus). Scale bar = 150 µm. Recording sides (1-16) are spaced by 100 µm. For reference, the morphological results showing shorter basal dendrites and longer apical dendrites in different strata are schematically depicted (arrows). **(C)** Representative example traces of LFP recordings during running in control (shSCR) and VEGFD downregulated (shVEGFD) mice. Typical theta and gamma oscillations are highlighted by arrowheads and arrows, respectively. Pyramidale is depicted in red. For simplification, only 7 channels spanning through the CA1 region are shown and analyzed. The dotted line indicates the typical phase shift of the theta wave as a function of depth. **(D)** Example mean theta LFP were filtered at 4-10 Hz, averaged from 50 theta cycles and aligned by the positive peak. From the averaged theta cycles derived contour map is depicted next to it. Cool colors represent relatively negative values and warm colors represent relatively positive values (A.U.). Note that two theta cycles are plotted for continuity. Corresponding CSD depth profiles (traces and contour map) are plotted in the lower panel in D. Analyzed data showed no difference in the LFP or CSD depth profile between the two groups. Thick lines represent mean values±SEM. **(E)** shows the same as (D) for gamma oscillations during running. Gamma oscillations were filtered at 35-70 Hz, aligned and averaged. Traces and contour map are shown for LFPs in the upper panel and for CSD analysis in the lower panel. Analyzed data revealed no difference in the LFP or CSD depth profile. Thick lines represent mean values±SEM. shVEGFD n=7, shSCR n=6, Multiple Student`s t-test.

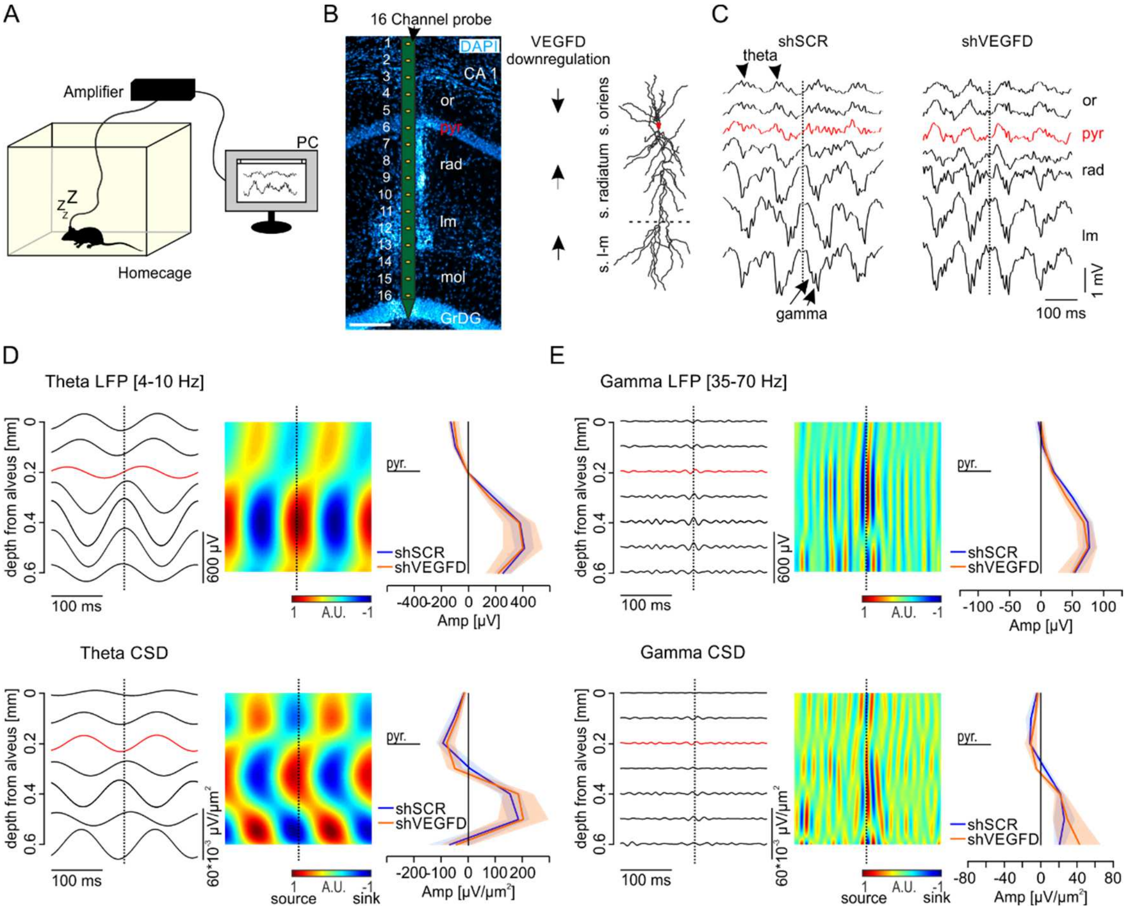

Figure 3-5. **Depth profile of theta and gamma LFP recordings and CSD depth profile during REM sleep reveals no change following VEGFD downregulation.** **(A)** Schematic representation of the homecage setup showing a mouse sleeping while recording LFPs. **(B)** 16-Channel probe superimposed on the histologically recovered track in CA1 spanning throughout all CA1 layers (or = stratum oriens, pyr = stratum pyramidale, rad = stratum radiatum, lm = stratum lacunosum-moleculare, CA1 = Cornu ammonis 1, GrDG = Granule cell layer of the dentate gyrus). Scale bar = 150 µm. For reference, the morphological results showing shorter basal dendrites and longer apical dendrites in different strata are schematically depicted (arrows). **(C)** Representative example traces of LFP recordings during REM sleep in control (shSCR) and VEGFD downregulated (shVEGFD) mice. Typical theta and gamma oscillations are highlighted by arrowheads and arrows, respectively. S. pyramidale is depicted in red. For simplification, only 7 channels spanning through the CA1 region are shown and analyzed. The dotted line indicates the typical phase shift of the theta wave as a function of depth. **(D)** Example mean theta LFP were filtered at 4-10 Hz, averaged from 50 theta cycles and aligned by the positive peak. From the averaged theta cycles derived contour map is depicted next to it. Cool colors represent relatively negative values and warm colors represent relatively positive values (A.U.). Note that two theta cycles are plotted for continuity. Corresponding CSD depth profiles (traces and contour map) are plotted in the lower panel in D. Analyzed data showed no difference in the LFP or CSD depth profile between the two groups. Thick lines represent mean values±SEM. **(E)** shows the same as (D) for gamma oscillations during REM sleep. Gamma oscillations were filtered at 35-70 Hz, aligned and averaged. Traces and contour map are shown for LFPs in the upper panel and for CSD analysis in the lower panel. Analyzed data revealed no difference in the LFP or CSD depth profile. Thick lines represent mean values±SEM. shVEGFD n=6, shSCR n=5,multiple Student`s t-test.

3.2.2 Measurements of Theta and Gamma Oscillatory Strength in VEGFD Knockdown Mice *in vivo*

Theta Power Spectral Density (PSD). In the next section, the PSD distribution of theta was investigated as a function of depth in shSCR and VEGFD downregulated mice, while voluntarily running on a treadmill and during REM sleep periods. The PSD was used as a parameter to analyze the impact on theta oscillation strength of changed dendritic geometry through VEGFD downregulation. As already described in in previous experiments, theta amplitude increases with depth (from s. oriens to s. lacunosum-moleculare) in both vigilance stages, which is also reflected by the PSD (Figure 3-6 andFigure 3-7). PSDs were computed from 30 sec of LFP traces in all seven channels. The PSD revealed a clear theta peak between around 6-8 Hz for both groups during running (Figure 3-6,B) and REM sleep (Figure 3-7,B). Furthermore, the power increased with depth in both groups, consistent with the literature (G. Buzsáki et al. 2003). Theta PSD during REM sleep showed for shSCR (mean = 4.3 $\mu V^2 * 10^4$) and shVEGFD (mean = 5.6 $\mu V^2 * 10^4$) animal groups a peak in s. lacunosum-moleculare. However, group analysis revealed no difference in the PSD depth profile after VEGFD downregulation (Figure 3-7,C). To account for inter-animal theta power variability, PSDs were normalized by a z-score. This revealed no difference between the shSCR and the shVEGFD group, as well (Figure 3-7,C).

Theta PSD during voluntary running on a treadmill showed similar results (Figure 3-6). However, during running the maximal power occurred in deeper layers compared to REM sleep. For the control group (shSCR) the maximum was in s. radiatum (mean shSCR = 7.1 $\mu V^2 * 10^4$) and for VEGFD group the peak was at the border between s. radiatum and s. lacunosum-moleculare (mean shVEGFD = 8.6 $\mu V^2 * 10^4$). The z-scored values, however, showed no difference in the location of the maximum power value. The depth profiles of the absolute values as well as the normalized values showed no significant difference (Figure 3-6,C).

In conclusion, theta PSD during running and REM sleep is not affected by the changed dendritic morphology of CA1 pyramidal cells through loss of VEGFD.

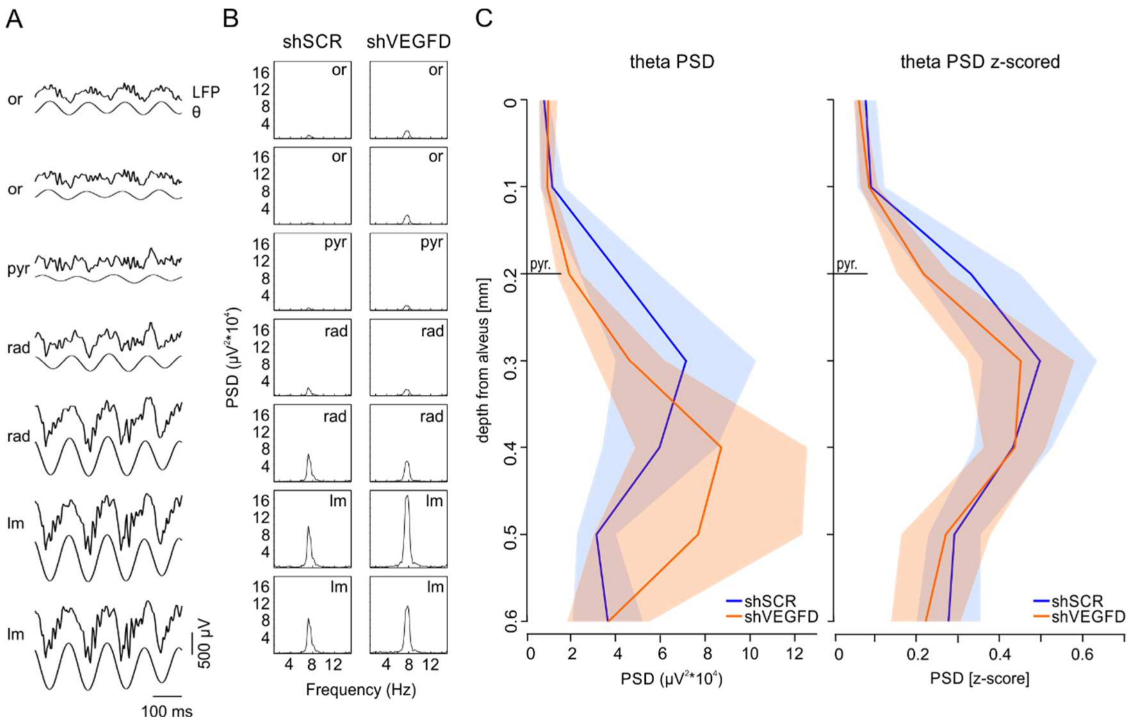

Figure 3-6. **No changes in theta power spectral density (PSD) following VEGFD downregulation during voluntary running on a treadmill. (A)** Representative raw traces of theta oscillations during running in CA1 as depth profiles and corresponding filtered traces (4-10 Hz) starting from superficial (or) to deeper layers (lm) (or = stratum oriens, pyr = stratum pyramidale, rad = stratum radiatum, lm = stratum lacunosum-moleculare). Note the increased amplitude as a function of depth. For simplification, only the 7 Channels spanning through CA1 are shown and analyzed. **(B)** Representative PSD for a shSCR and a shVEGFD mouse computed from 30 sec LFP from each animal. Note the large theta PSD peak at 6-8 Hz and the increasing PSD with depth. **(C)** Mean±SEM depth PSD profile and normalized profile reveal no difference after VEGFD downregulation compared to the control group (SCR). VEGFD n=7, SCR n=6, Student`s multiple t-test.

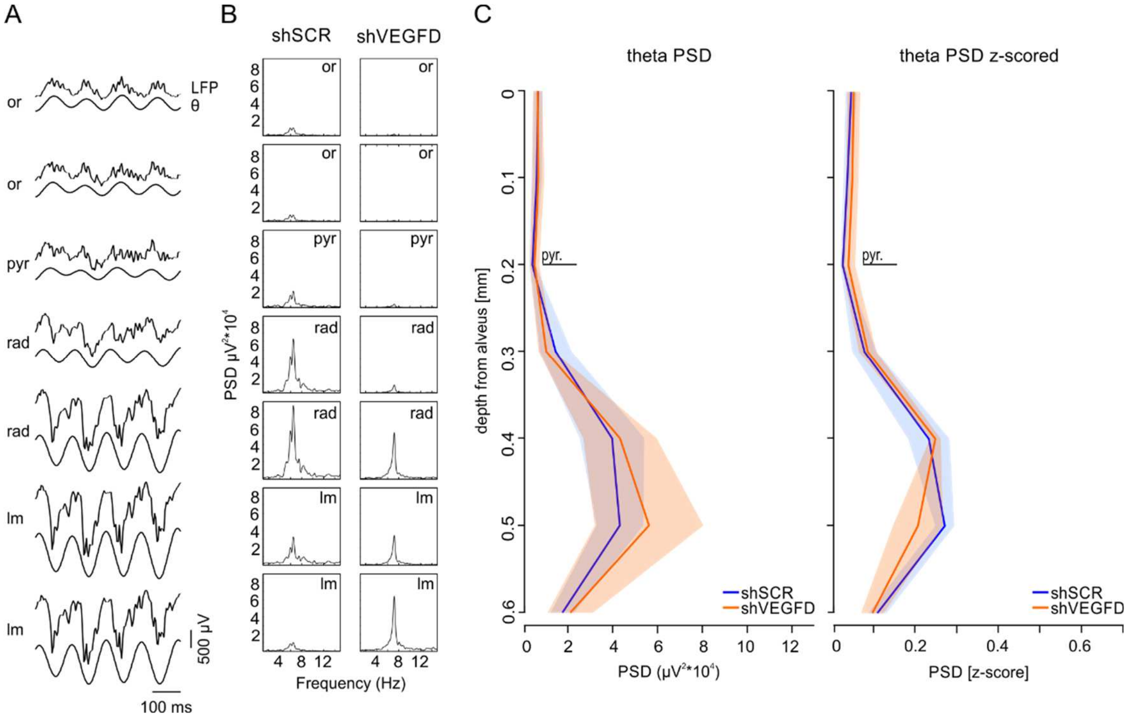

Figure 3-7. **No changes in theta power spectral density (PSD) following VEGFD downregulation during REM sleep. (A)** Representative raw traces of spontaneous oscillations during REM sleep in CA1 as depth profiles starting from superficial (or) to deeper layers (lm) (or = stratum oriens, pyr = stratum pyramidale, rad = stratum radiatum, lm = stratum lacunosum-moleculare). The corresponding bandpass filter was plotted beneath of each trace. The filter was set in the theta range of 4-10 Hz. Note the increased amplitude as a function of depth. **(B)** A large theta PSD peak at 6-8 Hz and an increasing PSD with depth were measured. **(C)** Depth PSD profiles and normalized profiles were plotted. Analysis of the PSD for both groups revealed no significant difference after VEGFD downregulation compared to the control group (SCR). Thick lines represent means and shaded areas represent ±SEM. VEGFD n=6, SCR n=5, Student`s multiple t-test.

Gamma Amplitude. The previous experiments showed the depth profile of gamma in the frequency range of 35-70 Hz as an average of gamma cycles/theta wave in VEGFD downregulated mice as well as control mice (Figure 3-4 andFigure 3-5). Next, the gamma amplitude of three distinct gamma frequency ranges was investigated. Based on the data set, the amplitude of slow-gamma (gamma_s, 35 – 70 Hz), middle-gamma (gamma_m, 70 – 120 Hz) and fast-gamma (gamma_f, 120 – 160 Hz) as a function of depth during running (Figure 3-8) and REM sleep (Figure 3-9) was analyzed. The three gamma bands in CA1 are generated by distinct mechanism and the alterations in the dendritic length of the pyramidal cell by VEGFD downregulation might influence them differentially.

The absolute values of gamma amplitude (Figure 3-8,B) and the z-score normalized values (Figure 3-8,C) during running between the control group (shSCR) and the VEGFD knockdown group were analyzed. Both datasets revealed a maximum of gamma$_s$ amplitude in s. lacunosum-moleculare (shSCR mean = 35 µV, shVEGFD mean = 35 µV, z-score: shSCR mean = 0.11, shVEGFD mean = 0.11), as it is generated by the entorhinal cortex input. Gamma$_s$ showed the highest amplitude values compared to middle- and high-gamma (gamma$_m$ mean values: shSCR = 17 µV, shVEGFD mean = 17 µV; gamma$_f$ mean values: shSCR = 8 µV, shVEGFD mean = 7 µV). However, there was no significant difference between shSCR and VEGFD downregulated groups in low-, middle- and high-gamma amplitude depth profiles detectable (Figure 3-8).

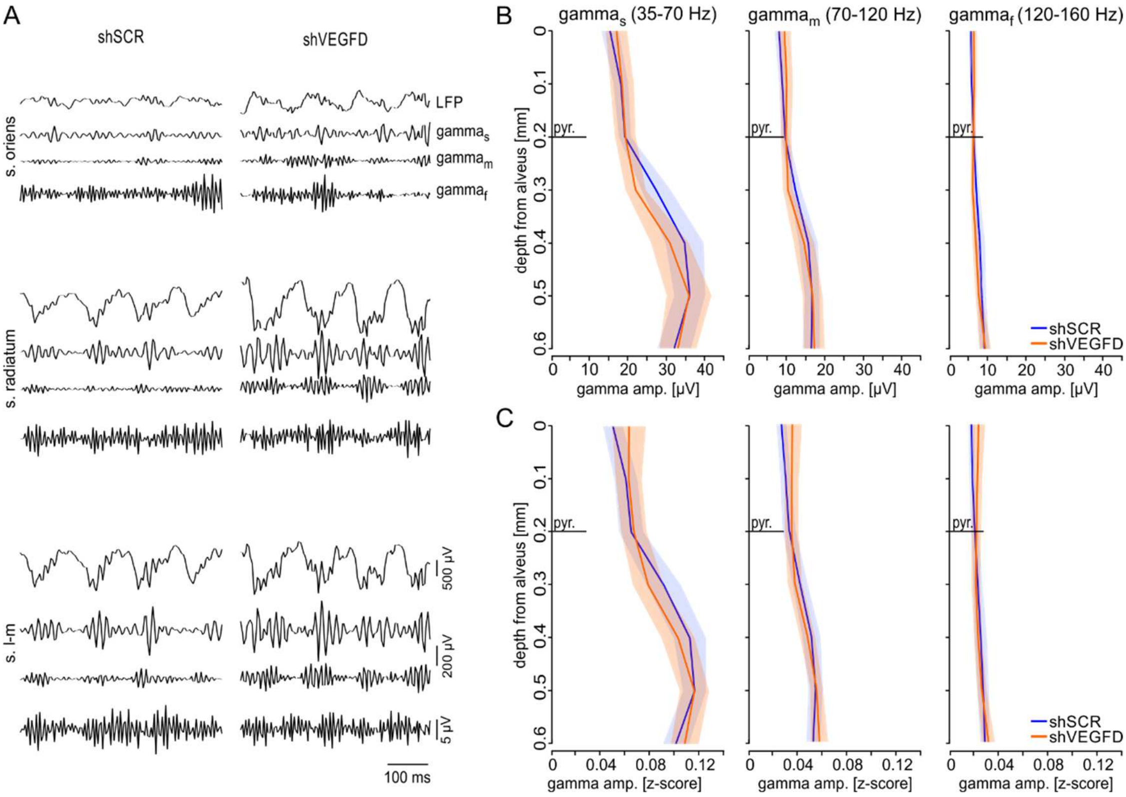

Figure 3-8. **Gamma amplitude during running in VEGFD knockdown mice. (A)** Representative raw traces of theta nested gamma oscillation in s. oriens, s. radiatum and s. l-m with corresponding band-pass filters for a single SCR and a single VEGFD animal. Data was bandpass filtered for slow-gamma at 35-70 Hz, middle-gamma at 70-120 Hz and high-gamma at 120-160 Hz. **(B)** Group analysis of absolute gamma amplitude values revealed no significant difference between shSCR and shVEGFD group in all three gamma bands. **(C)** Values were normalized by a z-score and showed no difference between analyzed groups. Thick lines indicate the mean, shaded areas indicate SEM. shVEGFD n=7, shSCR n=6, multiple Student`s t-test.

Gamma$_s$ during REM sleep showed a maximum amplitude in s. lacunosum-moleculare in absolute and relative values, as well (shSCR mean = 34 µV, shVEGFD mean = 31 µV; z-score shSCR mean = 0.08, shVEGFD mean = 0.08). Likewise, gamma$_s$ during REM revealed the highest amplitude values compared to gamma$_m$ and gamma$_f$ (gamma$_m$ mean values: shSCR = 13 µV, shVEGFD mean = 15 µV; gamma$_f$

mean values: shSCR = 5 µV, shVEGFD mean = 7 µV). The depth profile of amplitude of the three gamma frequency bands was not significantly different for absolute and normalized values (Figure 3-9).

These results suggest, that shorter basal dendrites and longer apical dendrites do not influence gamma amplitude of gamma$_s$, gamma$_m$ and gamma$_f$ in CA1 of the murine hippocampus.

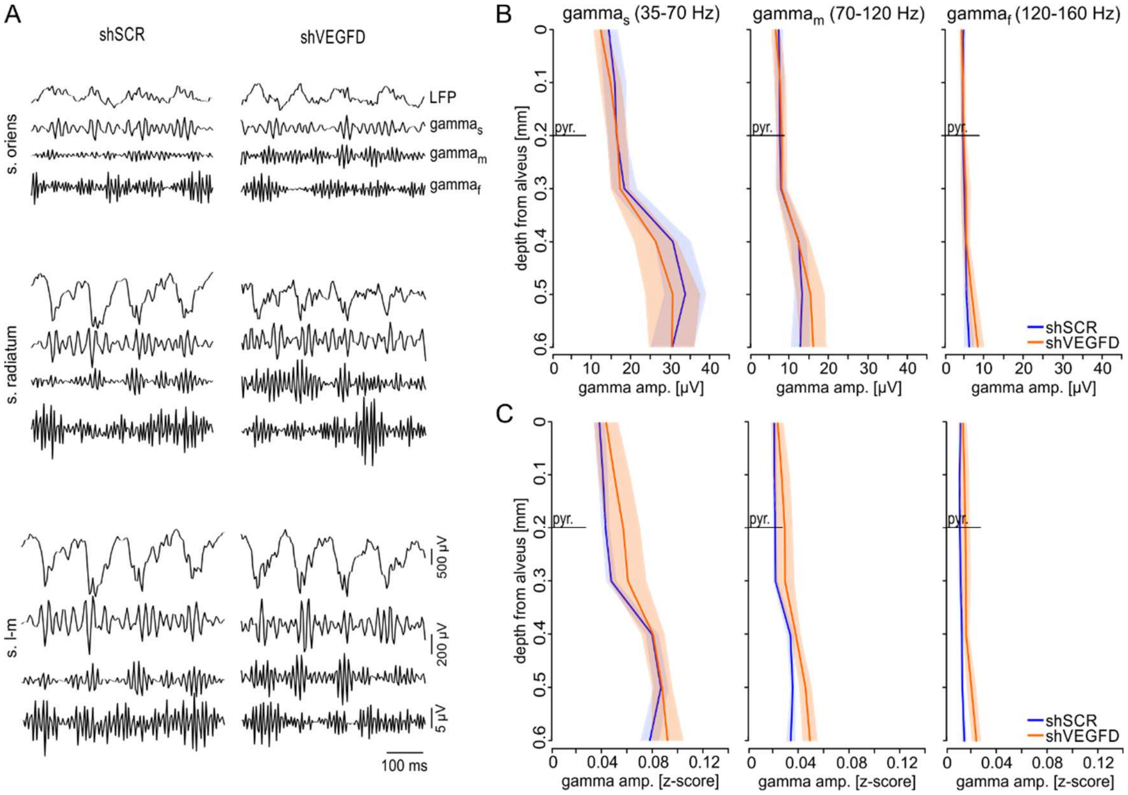

Figure 3-9. **Gamma amplitude during REM sleep in VEGFD knockdown mice. (A)** Representative raw traces of theta nested gamma oscillation in s. oriens, s. radiatum and s. l-m with corresponding band-pass filters for a single shSCR and a single shVEGFD animal. The filter was set for slow-gamma at 35-70 Hz, middle-gamma at 70-120 Hz and high-gamma at 120-160 Hz. **(B)** Group analysis of absolute gamma amplitude values revealed no significant difference between SCR and VEGFD group in all three gamma bands. **(C)** Normalized values were computed by a z-score and showed no difference between analyzed groups. Thick lines indicate the mean, shaded areas indicate SEM. shVEGFD n=6, shSCR n=5, Student`s multiple t-test.

3.2.3 Cross-Frequency Coupling of Theta and Gamma Oscillations in VEGFD Knockdown Mice *in vivo*

Theta and gamma oscillations were analyzed individually in the previous experiments. Neuronal oscillations of different frequencies can also interact with each other. The interaction of rhythms is called cross-frequency coupling (CFC). A particularly well investigated example is the phase-amplitude coupling (CF_{PA}) of theta and gamma in the hippocampus. The amplitude of the faster gamma rhythm is modulated by the slower theta rhythm. Furthermore, the amplitude of a faster oscillation can couple to multiple phases of a slower rhythm ($CF_{P\text{-}PA}$). Since the coupling of brain rhythms reflects a specific interplay of large cell ensembles, it is likely to have an impact on memory processes. Thus, the CFC of VEGFD knockdown mice was measured and compared to controls.

For both animal groups, the coupling strength (CF_{PA}) and coupling angle ($CF_{P\text{-}PA}$) were computed for the interaction of theta with $gamma_s$ and $gamma_f$. For this, depth profile recordings in CA1 during voluntary running on a treadmill and REM sleep were used. Raw and filtered example traces of spontaneous theta nested gamma oscillations for running are shown in Figure 3-12,A and for REM sleep in Figure 3-13,A. For simplification, raw LFPs and filtered signals are only shown for s. oriens (or), s. radiatum (rad) and s. lacunosum-moleculare (lm). However, comodulograms and phase plots are analyzed and shown for all seven channels.

Cross-Frequency Coupling: Phase-Amplitude (CF_{PA}). The strength of the phase-amplitude coupling was computed by the modulation index (MI, section 2.8.4) for VEGFD knockout and control mice. A weak coupling indicates that gamma amplitude is not modulated for theta phases and this is reflected in a small MI and vice versa. The MI of all frequency bands values were plotted in a comodulogram. The cold pseudocolors show weak coupling, whereas warm colors represent strong coupling. The comodulogram maps revealed a prominent coupling of theta-phase and gamma-amplitude in both theta associated vigilance states, running and REM sleep in both animal groups. This is indicated by warm colors, showing that the x-phase modulated the y-amplitude (Figure 3-10 andFigure 3-11,B). More specifically, the comodulation maps revealed a theta-phase coupling with two distinct gamma bands: One band at the frequency range of 35-70 Hz ($gamma_s$) and the fast-gamma $gamma_f$ at 120-160 Hz. Furthermore, different patterns of phase-amplitude coupling along the CA1 depth profile were visible. In s. oriens was a mix of coupling with both gamma bands detected, however, the modulation index was higher for $gamma_s$ during REM sleep (MI mean values $gamma_s$ shSCR = $5.9*10^{-3}$, shVEGFD = $7.7*10^{-3}$, $gamma_f$ shSCR = $2*10^{-3}$, shVEGFD = $3.2*10^{-3}$) and during running (MI mean values $gamma_s$ shSCR = $7.6*10^{-3}$, shVEGFD = $8*10^{-3}$, $gamma_f$ shSCR = $1.3*10^{-3}$, shVEGFD = $1.3*10^{-3}$). Around the pyramidal cell layer (pyr) the modulation indices were weak in both gamma bands and during both vigilance states, going in hand with no gamma inputs in this layer (REM sleep MI mean values $gamma_s$ shSCR = $3.1*10^{-3}$, shVEGFD = $4.8*10^{-3}$, $gamma_f$ shSCR = $2*10^{-3}$, shVEGFD = $2.5*10^{-3}$; running MI mean values $gamma_s$ shSCR = $4.5*10^{-3}$, shVEGFD = $5.2*10^{-3}$, $gamma_f$ shSCR = $2.1*10^{-3}$, shVEGFD = $0.9*10^{-3}$). The modulation indices of $gamma_s$ increased in s. radiatum, compared to the MI measured in s. oriens (REM sleep MI mean values $gamma_s$

shSCR = 11.2*10^{-3}, shVEGFD = 7.5*10^{-3}, gamma$_f$ shSCR = 4.2*10^{-3}, shVEGFD = 3.3*10^{-3}; running MI mean values gamma$_s$ shSCR = 8.5*10^{-3}, shVEGFD = 9.8*10^{-3}, gamma$_f$ shSCR = 2.6*10^{-3}, shVEGFD = 2.1*10^{-3}) and the MI for gamma$_f$ became slightly more prominent in s. radiatum and s. lacunosum-moleculare, as well (REM sleep MI mean values gamma$_s$ shSCR = 13*10^{-3}, shVEGFD = 8.7*10^{-3}, gamma$_f$ shSCR = 4.9*10^{-3}, shVEGFD = 4.8*10^{-3}; running MI mean values gamma$_s$ shSCR = 10.5*10^{-3}, shVEGFD = 8.8*10^{-3}, gamma$_f$ shSCR = 2.5*10^{-3}, shVEGFD = 2.4*10^{-3}). This pattern was visible in both vigilance stages. The analysis of the CFC depth profile for phase-amplitude modulation revealed no differences for both gamma bands during running and REM sleep between VEGFD downregulated and control groups (Figure 3-10 andFigure 3-11,C).

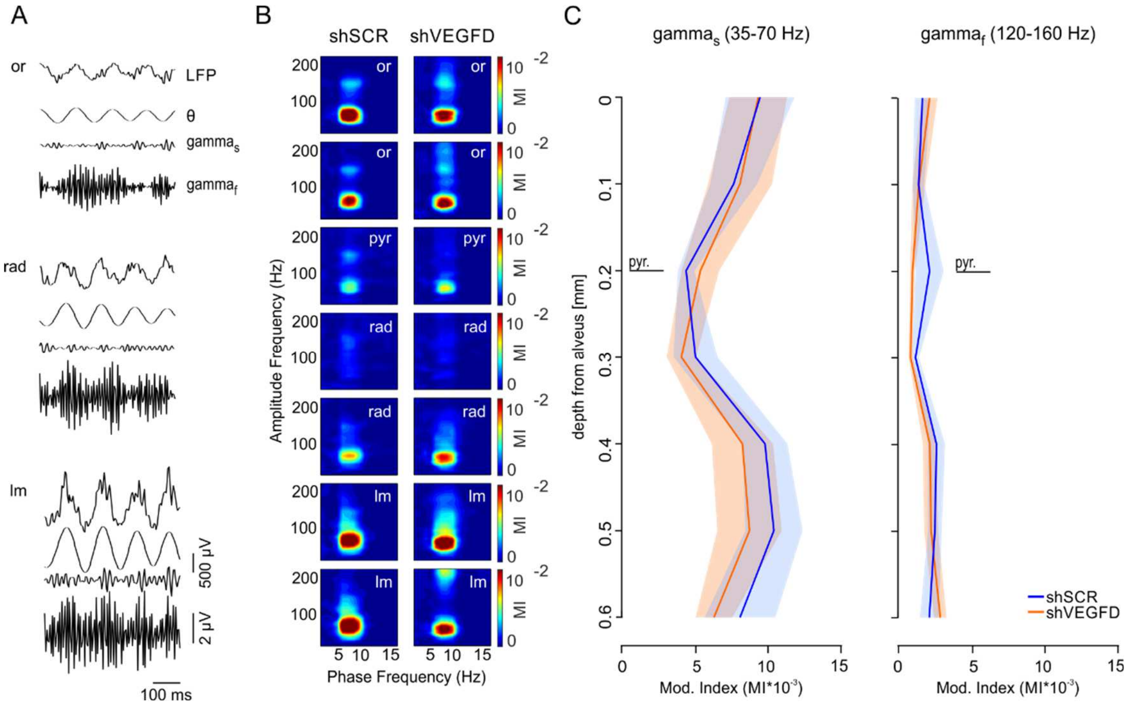

Figure 3-10. **Cross-frequency phase-amplitude coupling of theta and gamma during running.** **(A)** Representative raw and filtered LFP trace as a depth profile in CA1 **(B)** Pseudocolor comodulogram for a control (shSCR) and a VEGFD downregulated mouse as a function of depth derived as mean values from 30 sec of running period/animal. Pseudocolor scale indicates the Modulation Index (MI), where warm colors reflect high modulation of y-amplitude by x-phase and cold colors reflect little coupling. **(C)** Mean±SEM theta and gamma MI showing the modulation strength of theta phase and gamma amplitude for the shSCR and shVEGFD group as a depth profile. The MI is shown for the coupling of theta phase and gamma$_s$ (slow-gamma) amplitude and gamma$_f$ (fast-gamma) amplitude. No significant difference between both groups in both conditions. multiple Student`s t-test. shVEGFD n=7, shSCR n=6 (or = stratum oriens, pyr = stratum pyramidale, rad = stratum radiatum, lm = stratum lacunosum-moleculare, CA1 = Cornu ammonis 1)

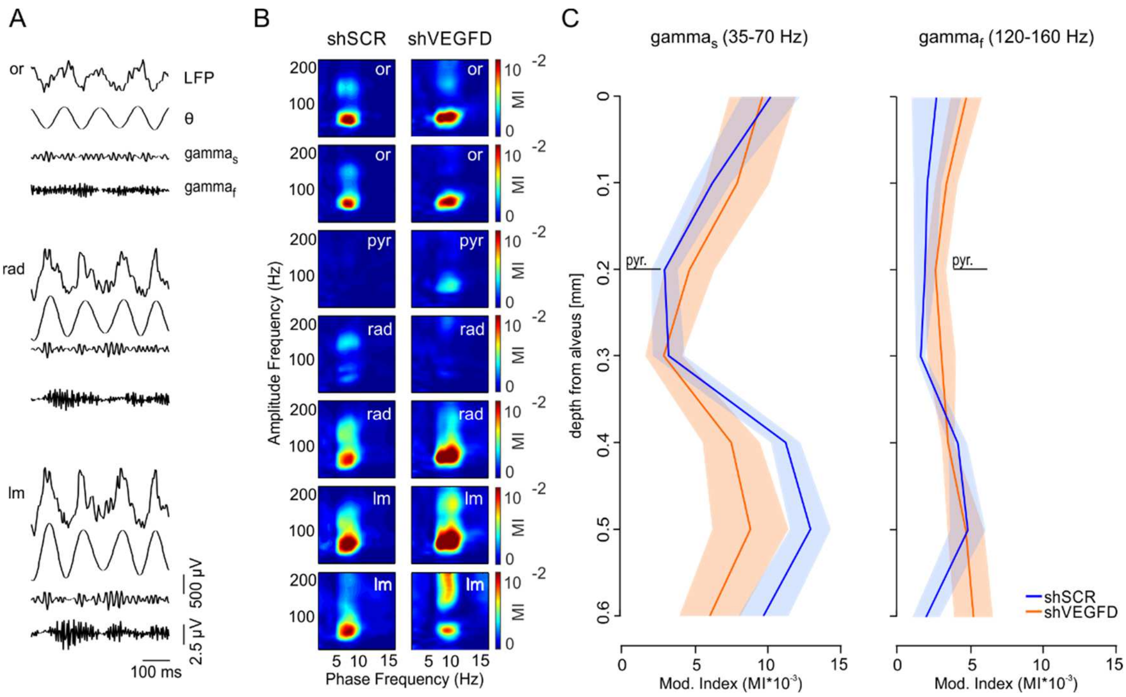

Figure 3-11. **Cross-frequency phase-amplitude coupling of theta and gamma during REM sleep.** **(A)** Representative raw and filtered LFP trace as a depth profile in CA1 **(B)** Pseudocolor comodulogram for a control (shSCR) and a VEGFD downregulated mouse as a function of depth derived as mean values from 30 sec of running period/animal. Pseudocolor scale indicates the Modulation Index (MI), where warm colors reflect high modulation of y-amplitude by x-phase and cold colors reflect little coupling. **(C)** Mean±SEM theta and gamma MI showing the modulation strength of theta phase and gamma amplitude for the shSCR and shVEGFD group as a depth profile. The MI is shown for the coupling of theta phase and gamma$_S$ (slow-gamma) amplitude and gamma$_f$ (fast-gamma) amplitude. No significant difference between both groups in both conditions. Multiple Student`s t-test. shVEGFD n=6, shSCR n=5. (or = stratum oriens, pyr = stratum pyramidale, rad = stratum radiatum, lm = stratum lacunosum-moleculare, CA1 = Cornu ammonis 1)

Cross-Frequency Coupling: Phase-Phase/Amplitude (CF$_{P\text{-}PA}$). In order to investigate the phase-phase/amplitude synchronization of theta and gamma in shSCR and shVEGFD animals, the phase-amplitude distribution of theta and gamma was used in order to compute the mean angle of this distribution. The results for the CF$_{P\text{-}PA}$ coupling indicates on which phase of the theta cycle the largest gamma amplitude occurred. The CF$_{P\text{-}PA}$ was analyzed in CA1 for the layers s. oriens, s. pyramidale, s. radiatum and s. lacunosum-moleculare in control and VEGFD downregulated animals. The grey arrows in the rose plots show individual animals and the colored arrow (blue: SCR, orange: VEGFD) the mean values (Figure 3-12 andFigure 3-13 for running and REM sleep, respectively).

Measuring the CF$_{P\text{-}PA}$ coupling of theta and gamma during running and REM sleep revealed a clear coupling in the deeper strata (s. oriens – s. radiatum). However, in the more superficial layer, most prominent in the last channel (s. lacunosum-moleculare), the coupling was not very strong (uniform distribution of the values indicates no coupling; Figure 3-10 andFigure 3-11,B).

During running the gamma$_s$ amplitude coupled to the descending theta phase in s. oriens, followed by a coupling to the trough in s. pyramidale and moved then to the ascending phase in more superficial layers (e.g. s. radiatum and s. lacunosum-moleculare; Figure 3-12, left panel in B). A similar pattern was observed for gamma$_f$ (Figure 3-12, right panel in B).

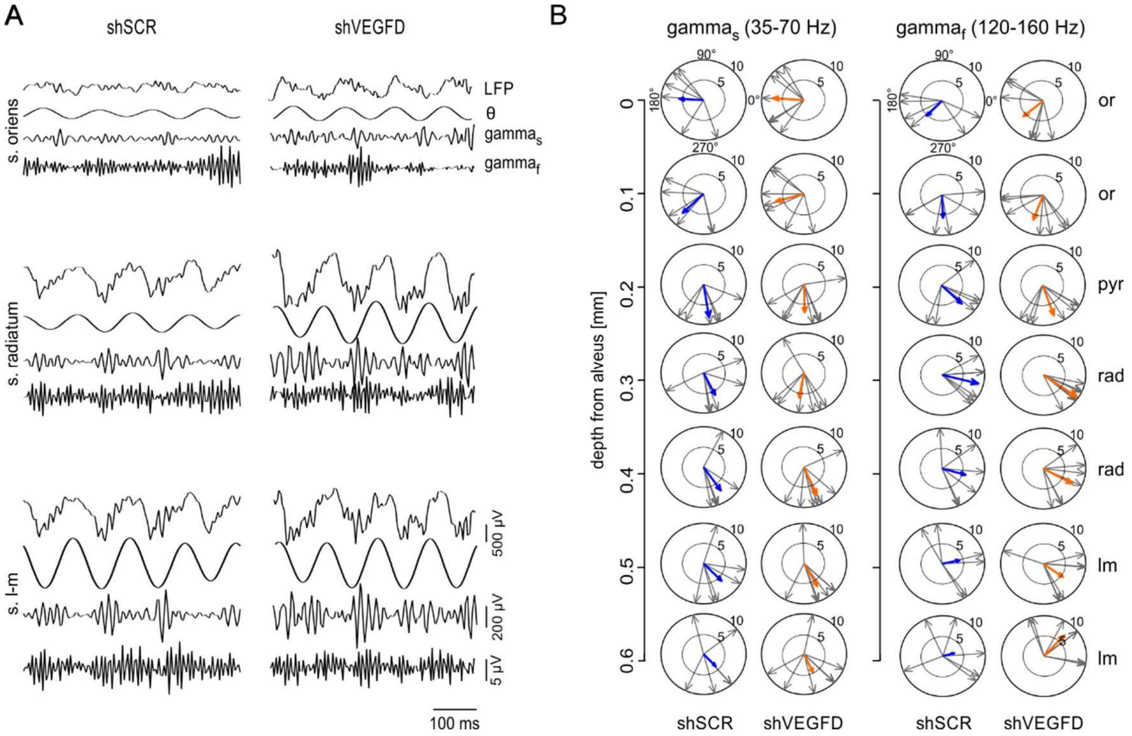

Figure 3-12. **Cross-frequency phase-phase/amplitude coupling of theta and gamma during running. (A)** Representative raw and filtered LFP trace of theta (4-10 Hz) and gamma$_s$ (35-70 Hz) and gamma$_m$ (120-160 Hz) as a depth profile in CA1 **(B)** Rose plots show the phase distribution of gamma bands coupling to the theta phase (0-270°). Cross-frequency phase-phase coupling as depth profile of theta and gamma$_s$ and gamma$_f$ revealed no significant difference between groups and conditions. Vector length statistics, Grey arrows indicate individual animals and colored arrows indicate mean vector length. Blue: shSCR n=6, Orange: shVEGFD n=7. (or = stratum oriens, pyr = stratum pyramidale, rad = stratum radiatum, lm = stratum lacunosum-moleculare, CA1 = Cornu ammonis 1).

In REM sleep, gamma$_s$ coupled to the descending phase of theta in deeper layers (s. oriens), coupled to the end of the descending phase and the trough in s. pyramidale and stayed there or coupled slightly to the ascending phase (Figure 3-13, left panel in B). Gamma$_f$ showed a similar pattern, however, gamma$_f$ showed the tendency to couple in superficial layers (s. radiatum and s. lacunosum-moleculare) to the ascending theta phase (Figure 3-13, right panel in B). In summary, the CF$_{\text{P-PA}}$ did not show a statistically significant difference during both vigilance states among groups (vector length). In summary, the CF$_{PA}$ and CF$_{P\text{-}PA}$ of theta and gamma oscillations were not affected by shorter basal and longer apical dendrites throughout the CA1 layers between VEGFD downregulated animals and controls.

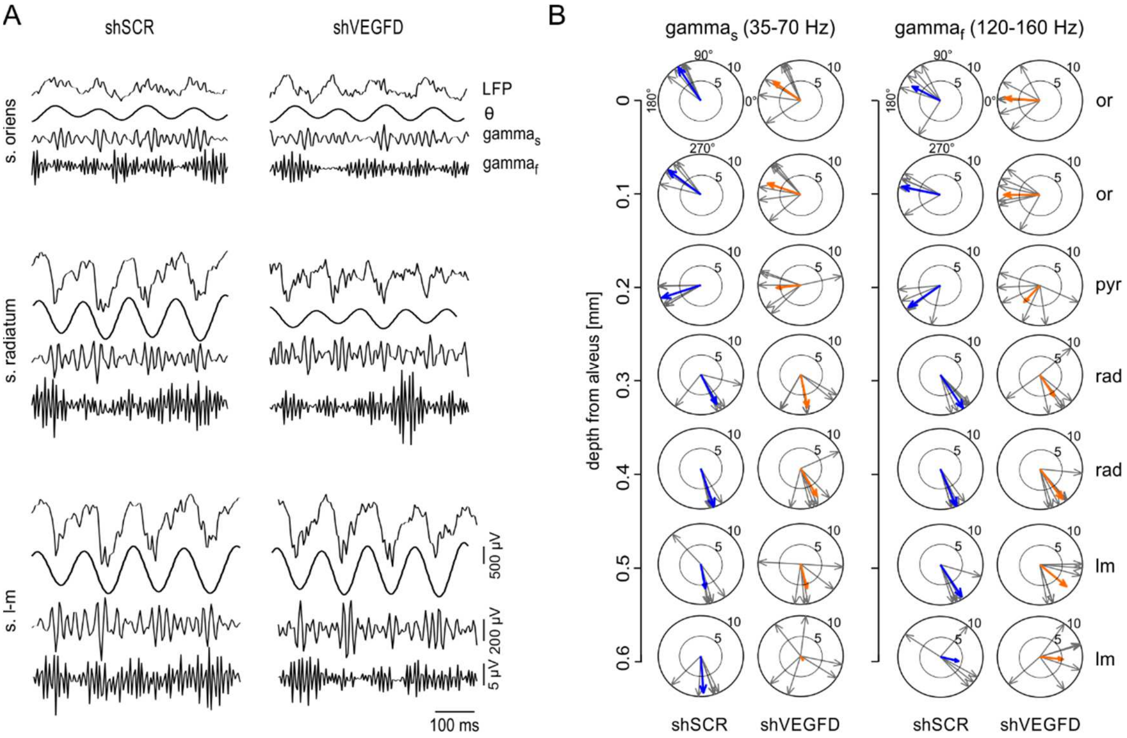

Figure 3-13. **Cross-frequency phase-phase/amplitude coupling of theta and gamma oscillations during REM sleep. (A)** Representative raw and filtered LFP trace of theta (4-10 Hz) and gamma$_s$ (35-70 Hz) and gamma$_m$ (120-160 Hz) as a depth profile in CA1 **(B)** Rose plots show the phase distribution of gamma bands coupling to the theta phase (0-270°). Cross-frequency phase-phase coupling as depth profile of theta and gamma$_s$ and gamma$_f$ revealed no significant difference between groups and conditions. Vector length statistics, Grey arrows indicate individual animals and colored arrows indicate mean vector length. Blue: shSCR n=5, Orange: shVEGFD n=6. (or = stratum oriens, pyr = stratum pyramidale, rad = stratum radiatum, lm = stratum lacunosum-moleculare, CA1 = Cornu ammonis 1).

3.2.4 Sharp Wave-Ripple Analysis in VEGFD Knockdown Mice *in vivo*

Sharp waves (SPW) are present during consummatory behaviors like immobility and slow-wave sleep. In the s. radiatum of CA1 SPWs reflect transient depolarization of pyramidal cell dendrites by a synchronous discharging CA3 network (G Buzsáki, Leung, and Vanderwolf 1983; Csicsvari et al. 2000). Simultaneous with the slow dendritic SPW event, a ultra-fast oscillation (“ripple”) is present in the CA1 pyramidal layer (O’keefe and Nadel 1978; G Buzsáki et al. 1992). Both together are described as sharp-wave ripple events (SPW-R). They are suggested to be involved in memory consolidation.

During the replay of SPW-R events pre-existing and newly acquired information are combined to influence decisions, plans, and thoughts (György Buzsáki 2015). Mauceri et al. (2011) showed a long-term deficit after VEGFD downregulation in both hippocampi of mice. By investigating SPW-R events in VEGFD knockdown mice *in vivo* it could be possible to reveal mechanisms that cause the long-term memory deficit.

Ripples were detected from 30 sec LFP traces during immobility (Figure 3-14) and nonREM sleep (Figure 3-15) and analyzed in s. pyramidale of shSCR and shVEGFD animals. A bandpass filter of 120-250 Hz revealed the ripple events. For group analysis ripples were aligned by the troughs and averaged (Figure 3-14 andFigure 3-15,A). The incidence of a SPW was measured as the number of SPW/second and revealed no significant difference in shVEGFD animals compare to control animals (immobility: shSCR median = 0.41 No/sec, shVEGFD median = 0.48 No/sec; nonREM: shSCR median = 0.54 No/sec, shVEGFD median = 0.45 No/sec). Furthermore, the number of ripple cycles/SPW was not affected by VEGFD knockdown in CA1 (immobility: shSCR median = 3 No/SPW, shVEGFD median = 4 No/SPW; nonREM: shSCR median = 3 No/SPW, shVEGFD median = 3.5 No/SPW). Last, the ripple cycle energy was compared between shVEGFD and shSCR animals and revealed no differences between groups during running and nonREM sleep (immobility: shSCR median = 53 μV^2, shVEGFD median = 165 μV^2; nonREM: shSCR median = 42 μV^2, shVEGFD median = 62 μV^2; Figure 3-14 andFigure 3-15,B).

Further, the depth profile of the SPW-R LFP and CSD along the somatodendritic axis in CA1 was compared between VEGFD deficient mice and controls. The ripples are detected as a negative peak at the s. pyramidale layer in the voltage depth profile. However, the amplitude was not different between groups in both stages (immobility mean values: shSCR = -95 µV, shVEGFD = -150 µV; nonREM mean values: shSCR = -109 µV, shVEGFD = -96 µV; Figure 3-14 andFigure 3-15,C respectively).

The current source density (CSD) analysis of the ripple LFP identified a sink in s. pyramidale, reflecting the ripple events (immobility mean values: shSCR = -7 $\mu V/\mu m^2$, shVEGFD = -14 $\mu V/\mu m^2$; nonREM mean values: shSCR = -11 $\mu V/\mu m^2$, shVEGFD = -7 $\mu V/\mu m^2$). Further, associated to the sink in s. pyramdiale, smaller passive sources in s. oriens (immobility mean values: shSCR = 3 $\mu V/\mu m^2$, shVEGFD = 1 $\mu V/\mu m^2$; nonREM mean values: shSCR = 3 $\mu V/\mu m^2$, shVEGFD = 0.2 $\mu V/\mu m^2$) and s. radiatum (immobility mean values: shSCR = 2 $\mu V/\mu m^2$, shVEGFD = 2 $\mu V/\mu m^2$; nonREM mean values: shSCR = 0.7 $\mu V/\mu m^2$, shVEGFD = 1.4 $\mu V/\mu m^2$), in both animal group in both vigilance stages were detected (Figure 3-14 andFigure 3-15,D). The sinks and sources were not significantly different during both vigilance states in VEGFD downregulated mice. To sum up, these results indicate that SPW-R are not altered in VEGFD knockdown mice.

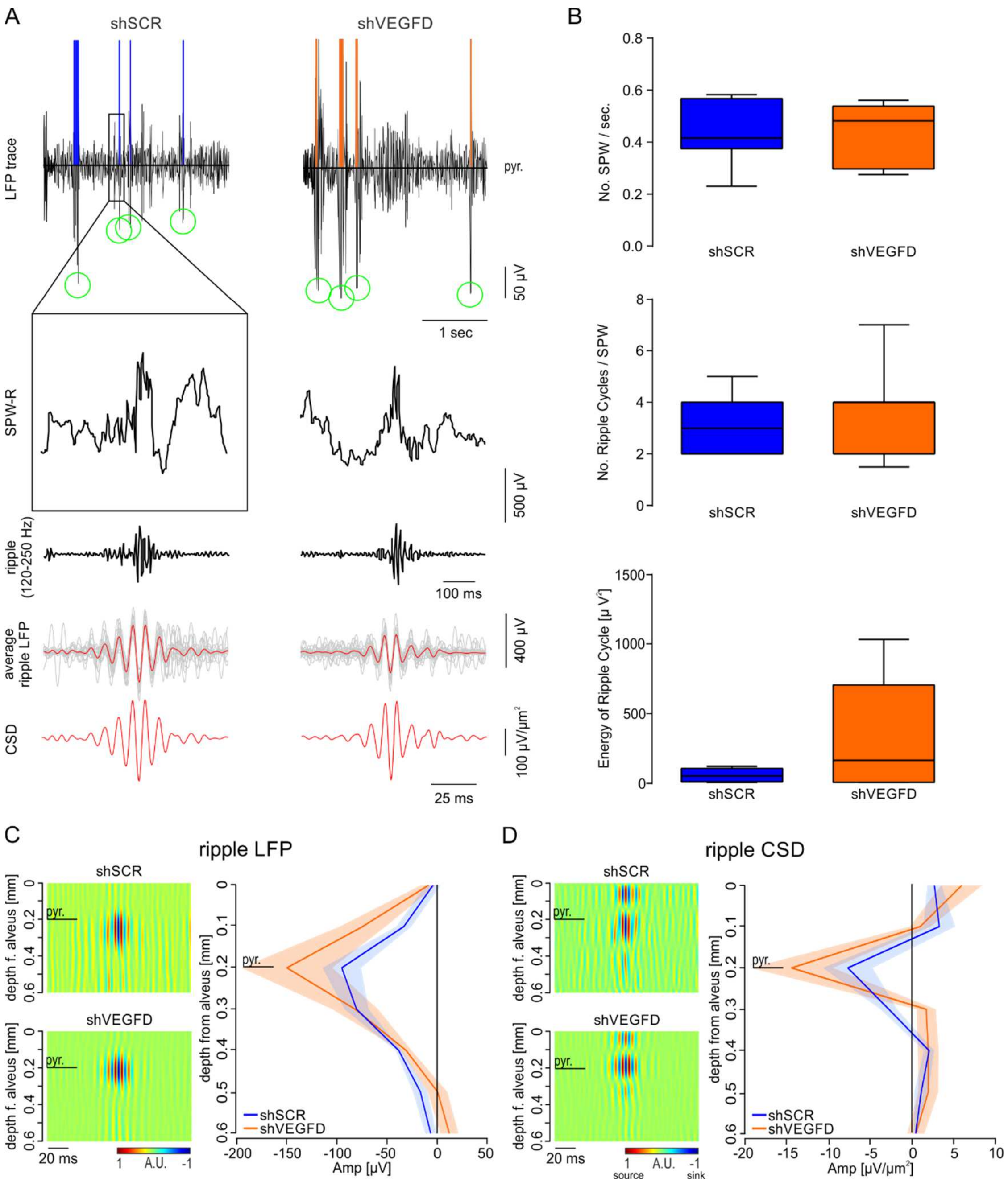

Figure 3-14. **Sharp-wave ripple analysis during voluntary immobility under head-restrained condition *in vivo*.** **(A)** Representative local field potential (LFP) recordings during immobility in CA1 stratum pyramidale (pyr) for shSCR (blue) and shVEGFD (orange). The colored line and the green circle indicate detected ripple events. Magnification shows a single sharp wave-ripple (SPW-R) event in s.pyr. Ripples extracted from the LFP by a bandpass filter at 120-250 Hz. Averaged ripple events from one recording session form one animal is shown in red and single events in grey. The corresponding CSD is depicted below. **(B)** Group analysis results for the number of SPW/second, number of ripple cycles/second and ripple energy show no difference between control (SCR) and VEGFD downregulated animals (unpaired Student`s t-test). **(C)** Voltage depth profile of the recorded ripples in shSCR and shVEGFD animals. **(D)** Corresponding current source density analysis (CSD) of the ripple LFP as a function of depth. Both profiles reveal a large sink in stratum pyramidale (pyr), corresponding to the ripples. shVEGFD and shSCR n=7, multiple Student`s t-test.

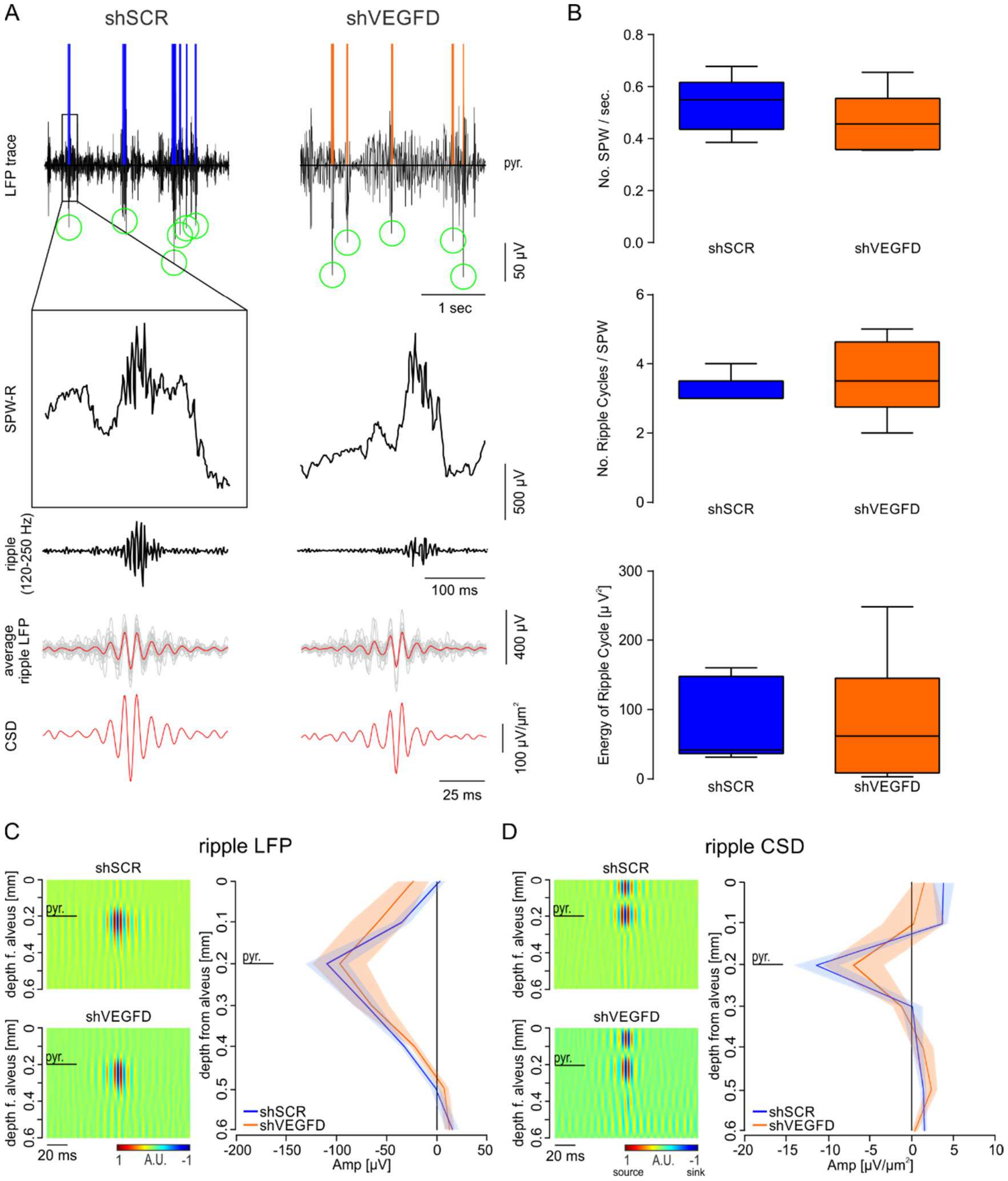

Figure 3-15. **Sharp-wave ripple analysis during nonREM sleep *in vivo*. (A)** Representative local field potential (LFP) recordings during nonREM sleep in CA1 stratum pyramidale (pyr) for shSCR (blue) and shVEGFD (orange). The colored line and the green circle indicate detected ripple events. Magnification shows a single sharp wave-ripple (SPW-R) event in s.pyr. Ripples were extracted with a 120-250 Hz bandpass filter. Averaged ripple events from one recording session form one animal is shown in red and single events in grey. Ripple- triggered average of the corresponding CSD is depicted below. **(B)** Group analysis results for the number of SPW/second, number of ripple cycles/second and ripple energy reveal no difference between shSCR and shVEGFD animals (unpaired Student`s t-test). **(C)** Voltage depth profile of the recorded ripples in shSCR and shVEGFD animals. **(D)** Corresponding current source density analysis (CSD) of the ripple LFP as a function of depth. Both profiles reveal a big sink in stratum pyramidale (pyr), corresponding to the ripples. shVEGFD and shSCR n=6, multiple Student`s t-test.

3.2.5 Current Source Density Analysis of Evoked Potentials in VEGFD Knockdown Mice *in vivo*

VEGFD downregulation in CA1 pyramidal cells caused changes in the length and complexity of basal and apical dendrites and no difference in spine density (Section 3.1.1 and 3.1.2). A possible effect on synaptic input strength onto sublayers in CA1 was analyzed by electrical stimulation of the commissural fibers and the temporoammonic pathway fibers. Coming from the contralateral hippocampus, commissural fibers innervate CA3, and through these basal and proximal apical CA1 pyramidal cell dendrites in s. oriens and s. radiatum. Temporoammonic pathway fibers, terminating in s. lacunosum-moleculare in CA1, originate in entorhinal cortex layer III (section 1.1.2). By stimulating the two inputs separately, it was possible to investigate synaptic inputs on all sublayers of interest (Figure 3-16,A).

First, postsynaptic potentials were recorded following stimulation of either one of the two pathways while the mouse was voluntarily running or being immobile on a circular treadmill. 50-60 evoked potentials were averaged per recording and per animal. To identify precisely current sources and sinks along the depth profile, the CSD of the averaged evoked potentials was calculated. CSD contour maps of the CA1 depth profile after commissural fiber stimulation during running revealed a sink in s. oriens (shSCR mean= -362 µV/µm^2, shVEGFD mean = -450 µV/µm^2) and s. radiatum (shSCR mean= -1017 µV/µm^2, shVEGFD mean = -1137 µV/µm^2) and a source in s. pyramidale (shSCR mean= 1280 µV/µm^2, shVEGFD mean = 1030 µV/µm^2) and s. lacunosum-moleculare (shSCR mean= 948 µV/µm^2, shVEGFD mean = 633 µV/µm^2; Figure 3-16,B middle panel).

The CSD analysis of the voltage response to commissural fiber stimulation during immobility showed similar results: A sink in s. oriens (shSCR mean= -399 µV/µm^2, shVEGFD mean = -490 µV/µm^2) and s. radiatum (shSCR mean= -1074 µV/µm^2, shVEGFD mean = -1390 µV/µm^2) and a source in s. pyramidale (shSCR mean= 1347 µV/µm^2, shVEGFD mean = 1349 µV/µm^2) and s. lacunosum-moleculare (shSCR mean= 1022 µV/µm^2, shVEGFD mean = 761 µV/µm^2; Figure 3-16, B left right) was observed. The pattern of current sources and sinks along the somatodendritic axis confirmed current literature (J Brankack, Stewart, and Fox 1993). The analysis of the CSD results during running and immobility showed no significant differences in the strength of current sources and sinks when VEGFD knockdown animals were compared to control animals (Figure 3-16,B right panels).

Temporoammonic pathway stimulation during running produced a sink in s. lacunosum-moleculare in shVEGFD and shSCR animals, corresponding to the EC layer III input in this layer (shSCR mean = -175 µV/µm^2, shVEGFD mean = -143 µV/µm^2). The sink in s. lacunosum-moleculare during immobility was only slightly stronger (shSCR mean = -257 µV/µm^2, shVEGFD mean = -198 µV/µm^2). Further, a source in s. radiatum occurred during running and immobility in both animal groups, which is passively associated with the sink in s. lacunosum-moleculare (running: shSCR mean = 232 µV/µm^2, shVEGFD mean = 108 µV/µm^2; immobility: shSCR mean = 185 µV/µm^2, shVEGFD mean = 231 µV/µm^2; Figure 3-16,C right panels). The sink and source in s. lacunosum-moleculare and s. radiatum were not significantly different between the control and the VEGFD knockdown animals. However, the analysis of the temporoammonic pathway stimulation revealed in both vigilance stages a difference between sinks and sources in shSCR and shVEGFD in deeper layers (s. oriens and s. radiatum). The shSCR group showed a source in s. radiatum (running: shSCR mean = 135 µV/µm^2, shVEGFD mean = 18 µV/µm^2; immobility: shSCR mean = 143 µV/µm^2, shVEGFD mean = 33 µV/µm^2) and s. oriens (running: shSCR mean = 57 µV/µm^2, shVEGFD mean = -61 µV/µm^2; immobility: shSCR mean = 52 µV/µm^2, shVEGFD mean = -41 µV/µm^2), whereas shVEGFD animals showed in these layers only a weak signal or a small sink. In s. pyramidale a source in shVEGFD animals, but not in shSCR was observed in both vigilance states (running: shSCR mean = -20 µV/µm^2, shVEGFD mean = 69 µV/µm^2; immobility: shSCR mean = -11 µV/µm^2, shVEGFD mean = 59 µV/µm^2). In general, these differences were stronger during running periods, compared to immobility (Figure 3-16,C right panels). Although, this is significantly different it is probably an artefact due to the 16-Channel electrode impedance levels. Additionally, in the left, upper panel of Figure 3-16,C are the sinks and sources visible which were caused by the trisynaptic loop, with some time delay (indicated by the arrowhead). This confirms furthermore the position of the electrode and the stimulation of the direct temporoammonic pathway in the first place.

Summarizing the above results, although basal dendrites became shorter and apical longer following VEGFD downregulation in CA1 pyramidal cells, the recorded evoked potentials in CA1 were not affected in the layers were the stimulated synaptic input arrives.

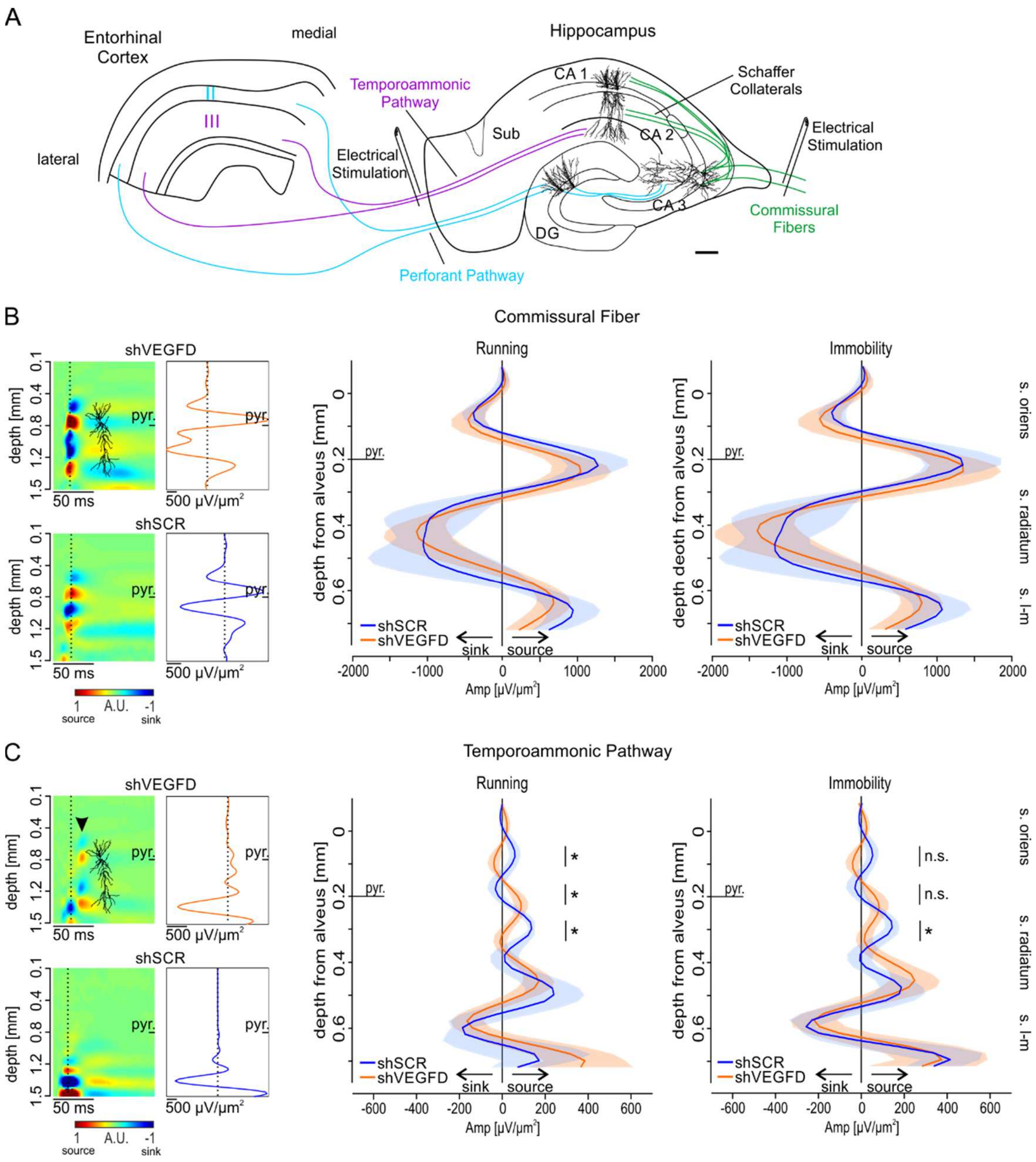

Figure 3-16. **Current source density analysis following electrical stimuli of commissural fibers and temporoammonic pathway fibers *in vivo* reveals no difference in VEGFD knockdown mice. (A)** Scheme of the hippocampus and entorhinal cortex indicating sides of stimulation of temporoammonic pathway fibers and commissural fibers and termination of the two pathways in CA1 (Adapted from Neves et al. 2008). **(B) Left panel:** Representative evoked responses for a shSCR and a shVEGFD animal in response to commissural fiber stimulation recorded in CA1 by a 16-Channel probe (spacing = 100 µm). CSD contour maps and corresponding depth profiles are depicted for a shSCR and a shVEGFD animal. Warm colors and relatively positive values denote current sources and cool colors, and relatively negative values denote current sinks. **Right panel:** Group analysis of CSD as depth profile for shSCR and shVEGFD during running and immobile episodes on the treadmill. **(C)** Same as in (B) for temporoammonic pathway stimulation. Note the evoked response in the CSD contour map occurring after a time delay marked with an arrowhead evoked by the trisynaptic loop. Data are plotted as mean±SEM. shVEGFD n=7 and shSCR n=6**,** multiple Student`s t-test. * = $p < 0.05$ (or = stratum oriens, pyr = stratum pyramidale, rad = stratum radiatum, lm = stratum lacunosum-moleculare, CA 1, 3 = Cornu ammonis 1, 3, DG = Dentate gyrus)

4 Discussion

The morphology of dendritic branches determines the connectivity of neurons and the signal integration and transmission. It has a high impact on the electrical properties of single neurons and the neuronal network. Thus, the regulation of the dendritic arborization is of great importance. This study investigated the effect of the growth factor VEGFD on dendritic morphology in CA1 pyramidal cells in the mouse hippocampus. Further, the functional consequences of VEGFD knockdown on single cell level and network level were investigated in order to potentially gain more insight in the relationship of form and function.

The regulatory effect of VEGFD on basal and apical dendritic arborizations in CA1 pyramidal cells was investigated. Following RNAi mediated knockdown of VEGFD *in vivo*, detailed morphometric analyses revealed an alteration of dendritic length and complexity. Similar to previous findings, basal dendrites became shorter and less complex. Interestingly, apical dendritic length and complexity were increased. Further investigations revealed that the elongation of apical dendrites occurs in areas with a high density of synaptic inputs, in particular, the s. radiatum (input from CA3) and s. lacunosum-moleculare (input from entorhinal cortex layer III). The spine density in all layers of CA1 remained unaltered, indicating a stronger synaptic input in apical dendrites and less input in basal dendrites.

The functional consequences of VEGFD loss were analyzed both on a single cell level and on the level of network oscillations. Following the suppression of VEGFD, and thus manipulating dendritic arborization, single cell recordings in acute hippocampal slices were performed. Passive membrane properties and action potential firing threshold were unchanged, although input resistance increased. The *in vivo* electrical stimulation of the commissural fibers and the temporoammonic fibers, two distinct input pathways to CA1, revealed no changes in the synaptic input. Furthermore, the investigation of network oscillations, including theta, gamma, and SPW-R oscillations during basic behaviors like sleep, running and immobility showed that the basic neuronal network was still intact after dendritic disruption.

In summary, the results showed a shortening and simplification of the basal dendritic tree following VEGFD downregulation, confirming current literature (Mauceri et al. 2011). Further, this study shows the effect of VEGFD on the apical dendritic tree. Thereby it provides new insights about how neurons might regulate their dendrites in a compartment specific manner. By analyzing basic network oscillations, this study provides more information and future directions for the gap between the morphology changes and the long-term memory disruption.

4.1 Morphological Changes of Apical and Basal Dendrites in CA1 Pyramidal Cells after VEGFD Downregulation

Following downregulation of VEGFD in CA1 pyramidal neurons, the cells exhibited shorter and simpler basal dendrites and longer, more complex apical dendrites. The changes in dendritic morphology were particularly prominent in s. oriens, s. radiatum, and s. lacunosum-moleculare, areas where CA1 pyramidal cells receive most of their excitatory input.

These results showed that VEGFD is involved in the *in vivo* regulation of the dendritic arborization of CA1 pyramidal cells, as already suggested by Mauceri et al. (2011). The experiments of Mauceri and colleagues showed an overall shorter and simpler dendritic arbor in cultured neurons. However, cultured neurons do not have a basal-apical dendritic polarity and are not embedded in the extracellular matrix and in highly organized neuronal networks. Due to more extrinsic factors, the regulatory mechanism of VEGFD *in vivo* might be more complex than *in vitro.*

The mechanisms to regulate dendrites are summarized by the term dendritic plasticity. Dendritic plasticity has been observed in the cortex of adult rodents, for example under enriched-environment conditions, sensorimotor learning, chronic exposure to drugs or under pathological conditions. The plasticity of dendrites is important in order to be able to adapt to certain stimuli, but also to maintain the current morphology and the synaptic connections within the network (Hickmott and Ethell 2006).

It has been shown that neurons are able to keep the overall balance of their dendritic trees by homeostatic mechanisms, which can take place on the following dendritic levels: (1) balance between whole dendritic compartments e.g. basal-apical, apical-apical (2) individual trees, originating from the soma and (3) the branches of subtrees (daughters and granddaughters; Samsonovich and Ascoli 2006). Samsonovich and Ascoli concluded that fluctuations in size in a given portion of the neuron (level 1-3) are systematically counter-balanced by the remaining dendrites in the same cell. This suggests further that, a neuron is first interested in keeping the global stability of synaptic input and thus the connectivity in the network. Second, in order to do so, neurons regulate different sub-compartments individually.

Homeostatic mechanisms could be involved in a rearrangement of the dendritic morphology after VEGFD loss. This can result in the shortening of basal dendrites in one compartment, which becomes counter-balanced by longer apical dendrites or vice versa. An unaltered total dendritic length (basal + apical) after VEGFD downregulation supports this theory. The consequence could be the maintenance of the overall synaptic inputs. This hypothesis was confirmed by the stimulation of two input pathways and recording of evoked potentials, which were not altered (Figure 3-16 and section 4.4).

The morphology homeostasis can be influenced and regulated by intrinsic and/or extrinsic factors (Samsonovich and Ascoli 2006). The work by Mauceri et al. and the experiments of this study have identified VEGFD as an intrinsic factor. It is likely that other signal molecules counteract the effects of VEGFD to maintain overall neuronal excitatory status. In particular, the transmembrane protein Lrig1 (leucine-rich repeats and immunoglobulin (Ig)-like domains 1) seems to have complementary effects to VEGFD on dendritic morphology in CA1 pyramidal cells (Alsina et al. 2016). Lrig1 is linked to a tyrosine kinase associated receptor and is able to regulate neurotrophic growth factors like BDNF (Brain-derived neurotrophic factor). Alsina et al. showed an increase in dendritic arborization after knockdown of Lrig1 in cultured neurons. Thus, Lrig1 shows the opposite effect of *in vitro* knockdown of VEGFD. Interestingly, the *in vivo* downregulation of Lrig1 in CA1 hippocampal neurons showed only an increase in length and complexity in apical dendrites and no effect on basal dendrites. The authors concluded a preferential regulation of Lrig1 of apical dendrites. Further, Lrig1 knockdown mice have a social interaction deficit. It is conceivable that signal molecules such as Lrig1 interact with VEGFD to regulate and maintain dendritic complexity in different branch types individually to maintain a stable input level to the cell.

The different effects on basal and apical could also result from a non-uniform distribution of factors or mechanisms involved in VEGFD signaling, thus causing distinct effects on basal and apical dendrites. As a secretory protein, VEGFD depends on the Golgi apparatus. It has been shown that the position of the Golgi apparatus determines the basal-apical polarity of neurons (de Anda et al. 2005). Further, the position of Golgi-outposts in dendrites enhances local secretory trafficking. These mechanisms could be involved in the differential regulation of basal and apical dendrites by VEGFD. This was shown for other proteins like the glycoprotein Reelin or the neurotrophic factor BDNF (Matsuki et al. 2010; Horton and Ehlers 2003).

After secretion of VEGFD in the extracellular space, it acts in an autocrine mechanism through VEGFR-3 (D Mauceri et al. 2011). One possible mechanism to achieve a local regulation of dendritic length could be a different VEGFR-3 expression in a certain compartment. The presence of the VEGFR-3 mRNA and expression in somata of CA1 neurons has been shown by *in situ* hybridization and RT-PCR, respectively (Shin et al. 2008). Furthermore Bhuiyan et al., 2015 showed an increase in VEGFR-3 expression in the soma of CA1 pyramidal neurons and in somata of neurons located in s. radiatum and s. lacunosum-moleculare after ischemia induction. So far, there is no literature about the distribution of VEGFR-3 expression in distinct layers of the CA1 area. Unfortunately, the antibodies for immunostainings of VEGFR-3 are not reliable. The local enrichment of VEGFR-3 seems plausible as other channels and receptors are known to be expressed CA1 layer specific, e.g. HCN 1 and 2 channels, GIRK channels and AMPA receptor (Kupferman et al. 2014).

In cell culture, VEGFD downregulation led to an overall shortening of dendrites (D Mauceri et al. 2011). However, the change in dendritic geometry after the knockdown *in vivo* was layer specific. This could indicate homeostatic effects based on extracellular factors, e.g. laminated incoming fibers. CA3 neurons project their axons via the Schaffer collaterals both to basal and proximal apical dendrites (Ishizuka, Weber, and Amaral 1990; Spruston 2008). A homeostatic mechanism could take place in order to counter-balance the CA3 input to CA1 neurons. Further, the inhibitory network differentially affects basal and apical dendrites of CA1 pyramidal neurons. The changed dendritic morphology of pyramidal neurons could be a mechanism in order to maintain inhibitory input over the complete dendritic branches. The soma and basal dendrites of OLM interneurons are located in the s. oriens and project their axons to the apical dendrites of pyramidal cells in s. lacunosum-moleculare (Klausberger 2009). OLM cells could provide a mechanism for comparison between compartments and provide information for further morphological homeostasis adjustments.

In order to exclude a bias due to natural variabilities in hippocampus size of animals, the widths of single CA1 layers were measured. The comparison showed no difference between animals and groups. Therefore, a bias can be excluded. To exclude further false positive results by Sholl analysis, the starting point of the Sholl spheres was located at the border between s. radiatum und s. lacunosum-moleculare. This confirmed the finding from the conventional Sholl analysis. However, it can not be fully excluded that the differences in apical dendritic length are due to CA1 cell type differences. In order to avoid this in our dataset, the position of the somata within the pyramidal cell layer was verified and showed no difference between cells. A bias from superficial versus deep pyramidal cells can be probably excluded (Figure 2-4). Due to the precise virus injection by stereotactic coordinates, the recorded cells were in a similar location within CA1, since only cells in the center of injection were approached. Allocated cells or cells with cut dendrites were excluded from the experiment. In summary, bias from hippocampal widths, the location of somata with the pyramidal cell layer and within the whole CA1 area was minimized as much as possible.

In summary. the work by Mauceri et al. and the experiments of this study have identified VEGFD as an intrinsic factor for dendritic morphology regulation in adult mice. Mauceri et al. showed an overall shortening of dendrites in cultured neurons, concluding if VEGFD is suppressed dendrites become shorter. The *in vivo* data here adds new information to the VEGFD mechanism. The results showed after VEGFD downregulation basal dendrites were shorter and apical longer, but the overall dendritic tree size did not change. Since the cell *in vivo* still needs to integrate into the network, homeostatic mechanisms could be involved to compensate dendritic size changes.

4.2 No Implications of VEGFD Knockdown on Spine Density

In the hippocampus, the majority of excitatory synapses are located at spines. Hence, spine density can be used as a rough estimation of excitatory input. RNAi mediated VEGFD knockdown in CA1 pyramidal cells, resulted in shorter basal and longer apical dendrites. Since spines arise along the dendritic shaft, the different amount of dendrites could affect the spine density and thus synaptic input. Spines are very dynamic structures and spine plasticity is involved in learning and memory (J. N. Bourne and Harris 2008). Therefore, the total spine density and the density of different spine types in s. oriens, s. radiatum and s. lacunosum-moleculare was investigated. By determining the density of distinct spine types, it was possible to get information on the spine turnover. Short and thin spines are considered to be young spines. Longer, filopodia-like spines are more mature and try to find connections with other spines. The most mature versions are the spines with a bigger head diameter than the neck diameter (Fortin, Srivastava, and Soderling 2012).

The results revealed no differences in the total spine density and the density of different spine types in the three dendritic compartments after VEGFD downregulation (Figure 3-2). A reason for no alteration in spine density could be that VEGFD regulates specifically the dendritic branching and has no direct effect on spines. This hypothesis is in line with the current literature. Although spine density is nuclear calcium signaling dependent, suggesting activity dependent spine plasticity, VEGFD is not the downstream partner of the signaling (D Mauceri et al. 2011). Multiple other genes, regulated by nuclear calcium signaling, could be involved in spine regulation, for example BDNF and the complement factor C1q (Orefice et al. 2013, Simonetti et al. 2013). Especially, the calcium-binding protein parvalbumin seems to regulate the nuclear calcium buffering capacity and thus the transcription of the C1q gene (Daniela Mauceri et al. 2015).

Since spine density remained unchanged but dendritic length was altered after downregulation of VEGFD, the results lead to the conclusion, that the spine numbers in basal dendrites decreased and in apical dendrites increased. Suggesting further less synaptic input in basal dendrites and more in apical dendrites. To test this, two distinct input pathways to the CA1 region were electrically stimulated *in vivo*: (1) The commissural fibers, forming synapses with basal dendrites in the s. oriens and with apical dendrites in s. radiatum and (2) the temporoammonic pathway projecting to the distal apical dendrites in s. lacunosum-moleculare. The most prominent dendritic alterations correlated with no changes in dendritic density in these three dendritic compartments. Stimulation of both pathways revealed no difference in the evoked potentials in CA1 of VEGFD downregulated animals (Figure 3-2). In conclusion, this showed that the synaptic input *in vivo* has not changed after VEGFD downregulation, although spine density indicated more synapses in apical dendrites and less in basal.

These findings suggest that homeostatic mechanisms might be not only counter-balance dendritic morphology but also regulate spine density. Spines are highly plastic structures and can thereby modulate the synaptic inputs to the cell. Several mechanisms could lead to adapted synaptic strength. It is possible that spines carry silent synapses or have a perforated synapse. The synapse itself can also adapt the synaptic strength by changing e.g. channel expression. Through these mechanism, spine plasticity can lead to an overall stable synaptic input strength, although other morphological changes take place, like dendritic morphology changes (Colgan and Yasuda 2014; J. N. Bourne and Harris 2008).

The determination of spine density is however only an indirect reference for excitatory synaptic input and further investigations are needed to clarify spine plasticity mechanisms. The analysis of the type-density revealed no differences, suggesting no alteration of the spine turn-over following VEGFD suppression. However, since spine development is a very dynamic and fast process, more sophisticated methods, like live time-laps imaging, are needed to investigate the spine behavior in more detail.

In summary, these results support the hypothesis that homeostatic processes keep the balance and maintenance of synaptic inputs. Moreover, spine plasticity could lead to a homeostatic effect in order to counter-balance the dendritic changes.

4.3 Functional Effects of VEGFD Knockdown at the Cellular Level

The potential effect of altered dendritic morphology on basic physiological properties in VEGFD deficient CA1 pyramidal neurons was investigated (Figure 3-3). To this end, single cells were recorded in whole cell configuration. The capacitance of VEGFD downregulated cells was not altered compared to control cells confirming the morphological findings. Although basal and apical dendrites showed abnormal changes in length and complexity, the overall dendritic size did not change and this is reflected in the membrane capacitance. This supports the hypothesis of the involvement of homeostatic mechanisms. Further, the result is in line with the current literature. Hemstedt et al. (2017) reported also no difference in membrane capacitance values in VEGFD downregulated cells. However, the values measured by Hemstedt and colleagues are smaller compared to our results (shSCR median: 144.3 pF; shVEGFD cells median: 139.15 pF, Hemstedt et al.: shSCR mean: 84 pF; shVEGFD cells mean: 80 pF). We determined the membrane capacitance in current clamp (section 2.8.1). It was shown, that this method yields higher capacitance values than measurements in voltage clamp (Golowasch et al. 2009), which was used by Hemstedt et al. . This explains the different values obtained in the two studies. Besides, both methods were developed for equipotential model systems, which is not the case for biological neurons and can lead to incorrect measurements of the capacitance particularly in dendritic compartments that are further away from the soma. Mauceri et al. (2011) showed a decreased membrane capacitance in cultured VEGFD downregulated neurons, which is in line with the lower dendritic surface area observed *in vitro*. However, in the experiments carried out in hippocampal slices presented here, it was not possible to confirm this observation. One possible reason might be that cultured neurons do not have a polarity (basal/apical) and any laminated structure and therefore the homeostatic effect from external factors do not apply.

This study observed a significant increase of input resistance after VEGFD downregulated neurons from acute hippocampal slices. The input resistance is inversely proportional to the membrane surface area. Since a balance between basal and apical dendritic length was observed and membrane capacitance was therefore not altered, changes in input resistance were not expected. However, it is possible that basal dendrites have a higher impact on the input resistance since they are directly connected to the soma. Because basal dendrites are shorter in VEGFD downregulated cells this can cause a higher input resistance. The experiments from Mauceri et al. (2011) in cultured VEGFD knockdown cells revealed a slight increase of the input resistance, confirming the shortening of all dendrites.

Through shorter basal dendrites and a higher input resistance caused by VEGFD downregulation, it is possible that synaptic currents at the basal dendrites could be translated more efficiently into postsynaptic potentials and somatic depolarization. In turn, this could lead to increased action potential output after basal dendritic input (Johnston et al. 1996). To test this, the action potential firing threshold was determined for VEGFD downregulated cells. The firing threshold was not different, which indicates no higher excitability of shVEGFD cells. However, further parameters need to be investigated to gain a better understanding of the excitability of these cells, for example firing frequency or firing mode and more. The action potential firing threshold and excitability of cells determine strongly the integration of a neuron into neuronal networks. Since this is crucial for the single cell as well as neuronal networks, strong homeostatic mechanism have been proposed to control the action-potential threshold and excitability (Beck and Yaari 2008). Buzsaki, for example, reported homeostatic mechanisms regulating the neuronal excitability by bursting discharge in order to maintain synaptic strength and subsequent firing rate (Buzsaki 2002). A higher excitability of the cells due to changed dendritic morphology could lead to abnormal circuit synchronization and thus cognitive dysfunction, as shown for e.g. Alzheimer's disease (Palop et al. 2007).

Dendritic ion channels regulate excitability and information integration. They can influence the degree of the attenuation of EPSPs propagating along dendrites. In this study, possible changes of the h-current (I_h) in VEGFD downregulated cells was hypothesized. The I_h current is mediated through HCN channels 1 and 2, which are increasingly expressed as a function of distance to soma in the apical dendrite (Lörincz et al. 2002). I_h in dendrites causes an attenuation of EPSP summation and contributes to the separation of dendritic compartments (Magee 1998). It has been shown, that a downregulation of I_h in CA1 pyramidal cells causes a hyperpolarizing resting membrane potential, a higher input resistance and an increase in EPSP summation (Shah et al. 2004; Jung et al. 2007). Further, it has been shown that HCN-1 null mutant mice have motor learning and memory deficits (Nolan et al. 2003). An increase in I_h was hypothesized since VEGFD downregulated cells exhibit longer and more complex apical dendrites and thus potentially more HCN 1 and 2 channels. The sag amplitude was measured as a parameter for I_h current. However, the sag amplitude did not change after VEGFD downregulation. This indicates that less HCN 1 and 2 channels are expressed due to intrinsic plasticity processes, in order to keep the I_h constant. Several mechanisms could underlie this process. Different rates of expression and insertion influences the density of channels and changes in mRNA and protein levels have been shown for HCN channels (Shah et al. 2004). Additionally, the channels could be modulated by tyrosine-kinase mediated phosphorylation, which can be trigger by changed stimulation patterns (Hoffman and Johnston 1998). The mechanism underlying intrinsic plasticity are not well understood and need further investigation. The fact that VEGFD downregulated cells do not show a difference in the sag amplitude, could also be due to technical issues. The cells were recorded at the soma in whole-cell configuration, while I_h current is mediated through HCN channels expressed away from the soma. Due to space clamp issues, the recording of the sag amplitude might be inaccurate.

4.4 Functional Effects of VEGFD Knockdown on Network Oscillations

Changes in dendritic length and complexity are expected not only to impact the performance of single cells but also impact the computational power of neuronal network and thus the signatures of the network oscillations (Häusser, Spruston, and Stuart 2000). It has been shown that dendritic structural degeneration in a murine Alzheimer's model causes cellular hyperexcitability, underlying network dysfunction (Šišková et al. 2014). Also, the findings from Mauceri et al. (2011) support such a link between dendritic morphology and cognitive performance. The authors reported a long-term memory deficit in mice with altered branching of basal dendrites, mediated by VEGFD downregulation in the hippocampus. Results shown here revealed additional information about dendritic morphology changes in apical dendrites suggesting a change in the connectivity of neurons. Different network connections might cause a shift in inputs and their integration and further influence the hippocampal oscillations. In this study, three prominent hippocampal network oscillations, which are involved in learning and memory processing, were recorded in order to investigate whether changes in dendritic structure influences oscillations leading to long-term memory impairments.

Theta. Theta oscillations (4-10 Hz) have been proposed to provide a temporal framework for spike timing (phase precession) and a global synchronization mechanism of brain areas. Thus, hippocampal theta is highly involved in learning and memory processes (O Jensen and Lisman 1996 and 2000). The generation of theta in CA1 depends on excitatory and inhibitory drive arriving at distinct dendritic compartments (section 1.3.1; György Buzsáki 2002). The excitatory and inhibitory inputs at different locations along the CA1 pyramidal neurons cause current diploes across the layers leading to the amplitude and phase depth profile (section 1.3.1; Leung 1984). Consequently, a change in the morphology of dendrites of pyramidal neurons could affect theta oscillations due to altered synaptic input balance or integration in distinct dendritic compartments. Therefore, theta oscillation as a function of depth along the CA1 area was investigated. Theta oscillation power, LFP and CSD depth profiles along the somatodendritic axis were not altered by the morphological changes caused by VEGFD downregulation. No changes were detected neither during running or REM sleep periods (sections 3.2.1 and 3.2.2). In conclusion, theta oscillations in CA1 are not influenced by dendritic morphology changes and VEGFD knockdown.

Gamma. Three distinct gamma bands in CA1 after VEGFD downregulation were analyzed: slow-gamma (gamma$_s$, 35 – 70 Hz), middle-gamma (gamma$_m$, 70 – 120 Hz) and fast-gamma (gamma$_f$, 120 – 160 Hz). Gamma oscillations are generated by distinct inputs on pyramidal neurons arriving in different layers of CA1 (Schomburg et al. 2014) and are important for encoding and retrieval of memory (section 1.3.2). The distinct morphology changes of basal and apical dendrites might influence all gamma bands or only a particular gamma oscillation and thus lead to long-term memory impairments. By analyzing gamma amplitude, LFP and CSD as a function of depth throughout all CA1 layers no difference in any parameters in downregulated versus control mice were observed (sections 3.2.1 and 3.2.2). To conclude, shorter basal dendrites and longer apical dendrites do not affect the three gamma oscillations in CA1.

CFC. The CFC of theta and gamma has been shown to play a role in sequential memory organization, maintenance of working memory and memory recall. Since pyramidal neurons are highly involved in theta and gamma oscillations, the changed dendritic geometry could influence the interaction of the two oscillations. For this study, the influence of theta phase on the gamma amplitude strength (CFC$_{\text{P-A}}$) and the coupling of the gamma amplitude to certain theta phase (CFC$_{\text{P-P/A}}$) was investigated. Both types of CFC were not affected by altered dendritic morphology and downregulated VEGFD. Thus, changes in dendritic morphology do not influence CFC of theta and gamma in CA1 and could not cause a long-term memory deficit (section 3.2.3).

SPW-R. Synchronized bursts of CA3 pyramidal cells depolarize CA1 pyramidal cells via the Schaffer collaterals and thus generate field potentials called sharp waves (SPW). This excites inhibitory neurons in CA1 that triggers the fast “ripple” oscillation which is correlated with the SPW in s. pyramidale and produces the SPW-R complex (section 1.3.4). The analysis of SPW incidence, number of ripple cycles/SPW, the ripple cycle energy and LFP and CSD depth profiles revealed no alterations of any parameters upon VEGFD downregulation during immobility and nonREM sleep (section 3.2.4). This supports our findings, that synaptic input from the Schaffer collaterals is not altered.

Evoked Potentials. The stimulation of distinct input pathways onto different dendritic compartments and layers of CA1 revealed no difference in the synaptic input in CA1 after VEGFD downregulation. The commissural fibers innervate through CA3 and Schaffer collaterals the basal and proximal apical dendrites of CA1 pyramidal cells. The CSD analysis of the voltage profiles showed no effect on the synaptic input to s. oriens and s. radiatum upon altered dendritic morphology. Additionally, the stimulation of the direct input to CA1 from EC layer III via the temporoammonic pathway revealed no changes in the s. lacunosum-moleculare. However, after temporoammonic stimulation, a difference between VEGFD and SCR in the CSD of the synaptic input was detected in deeper layers of CA1. By careful investigation of the raw traces and voltage profiles, we concluded that this is an artefact caused by the different impedance values of the single recording sides of the 16-Channel probes. This artefact has a bigger influence in the recordings of the temporoammonic pathway stimulation because the signal is smaller compared to the potentials evoked by the commissural fiber stimulation. However, an effect caused by feed-forward inhibition cannot be excluded. Further experiments are necessary for clarification. In summary, the direct synaptic input in the expected laminae (s. oriens, s. radiatum, and s. lacunosum-moleculare) are not affected by VEGFD downregulation.

The interesting observation that network oscillations were not affected by altered dendritic geometry could have several reasons. The homeostatic effect by mechanisms mentioned in section 4.1 - 4.3 might influence network oscillations. The dendritic morphological homeostasis, the synaptic plasticity, and intrinsic plasticity mechanisms led all to an overall balance of dendritic geometry, spine density and intrinsic properties within the cell. These cellular properties underlie the network activity in CA1 and thus these homeostatic mechanisms could stabilize network oscillations as well.

In general, the brain has to keep an equilibrium between stability, necessary to maintain the basic connection as well as plasticity, necessary for adaption and learning processes. The experiments presented in this study showed stable basic network oscillations during vigilance states like sleeping, running, and immobility, even after the downregulation of VEGFD and subsequent changes in dendritic morphology. This indicates that basic network properties are maintained by compensatory mechanisms. However, the adult brain still needs to adapt to ongoing processes, e.g. during learning or consolidation of new memories. VEGFD downregulation might only lead to detectable changes in network oscillations and memory deficits if the animal is actually performing a memory task. Long-term memory deficits in VEGFD deficient mice were reported, when the mouse had to learn where the hidden platform in the Morris water maze is or while the mouse was exposed to a fear conditioning or fear extinction paradigm. The normal behavior and short-term memory were not affected (D Mauceri et al. 2011; Hemstedt et al. 2017). Therefore, it is necessary to record network oscillations in VEGFD knockdown animals, while the mouse performs a specific task.

Pyramidal neurons are able to detect coincident inputs to proximal and distal dendritic regions, providing a cellular associative mechanism for combining feedforward and feedback information (Larkum 2013). In the hippocampus, this mechanism could be relevant for memory consolidation, a task that presumably requires the association of various experiences such that one thought leads to another (Rolls 2010). The decrease in basal dendritic length and increase in apical dendrites of CA1 pyramidal neurons could cause a disruption of the associative function. As shown in this study, the spine density did not change after VEGFD downregulation. However, due to the changed dendritic length, this could lead to a decreased total spine number in basal dendrites and an increased total spine number in apical dendrites. Although the synaptic input was unaltered, the change in relative spine number in basal versus apical could cause a mismatch between the association of dendritic inputs. An incorrect association strength of basal versus apical input might lead to a long-term memory deficit.

Another reason why no effect of VEGFD downregulation on network oscillations was detected might be the variability between animals. Herreras and colleagues showed that certain principal components of an oscillation, e.g. the pattern of the theta generator originating in CA3, can be found in any animals and are comparable between animals. However, they report also a high variability between animals. Therefore, it is suggested to record oscillations before and after a treatment in individual animals and to compare only relative values between animals (Makarova et al. 2011, Herreras, Makarova, and Makarov 2015). In our case, potential differences might be averaged out between different animals, because differences are too variable or too small. Thus, recordings of network oscillations before and after VEGFD downregulation within the same animal could reveal more information. Furthermore, these recordings would give more information about the changes over time.

Further, it cannot be neglected that the local oscillations in CA1 are not only influenced by active sources but also by passive sources. Volume conductance is the passive propagation of an electric field. Thus, neighboring brain areas influence each other not only by active interaction but also passively (Peraza et al. 2012). Since VEGFD was only downregulated in CA1 and not in the whole hippocampus in order to prevent any upstream effects, the other areas of the hippocampus formation are still intact. Hence, they can passively influence the LFPs recorded in CA1. Since no strong effects of VEGFD downregulation on the local CA1 networks were detected, possible smaller effects could be hidden by passive sources like volume conductance. Simultaneous recordings in two brain areas could help to determine volume conductance components (Dzirasa et al. 2011).

4.5 Outlook

Taken together, by using detailed morphometric analyses, whole-cell patch clamp recordings and *in vivo* network recordings the consequences of VEGFD downregulation on the dendritic morphology of CA1 pyramidal cells were demonstrated. A compartment specific decrease of the dendritic length of basal dendrites, confirming current literature, and an increase of apical dendrites, adding more information for apical dendritic branches, was reported. The morphological change did not disrupt basic physiological properties of single CA1 pyramidal neurons and had no effect on theta, gamma, and SPW-R oscillations. Nevertheless, some questions remain open for further investigation.

Dendritic Morphology. A distinct effect on basal and apical dendritic length in CA1 pyramidal cells after VEGFD knockdown was shown. The signaling mechanism seems to be dependent on specialized dendritic compartments and local extrinsic factors, influencing the dendritic length adjusted to certain compartments (section 4.1). Further experiments are needed in order to investigate the signaling pathway of VEGFD and potential local differences. As a first approach, the investigation of the secretory pathway e.g. by tagging VEGFD would reveal exciting information. Additionally, this could be expanded to study the influence on VEGFD of extracellular matrix proteins and their local distribution (e.g. Reelin) and other potential factors, involved in dendritic maintenance, e.g. Lrig1. Another approach in order to gain information of VEGFD signaling and local adaptions would be immunostainings for the receptor in order to see the distribution of the expression under different circumstances: different time points, certain treatment e.g. VEGFD downregulation with and without rescue by administering rVEGFD.

The experiments so far showed a stationary picture from the regulation of dendritic maintenance by nuclear calcium VEGFD signaling, since only one time point in fixed tissue was investigated. *In vivo* live imaging can reveal new insight about the time course of the effect of VEGFD downregulation. It could show that the first effect is the shrinkage of dendrites and secondary effects involve homeostatic mechanisms.

The effects of VEGFD downregulation have been successfully rescued by rVEGFD administration or overexpression (D Mauceri et al. 2011). However, it would be interesting to investigate the effect of VEGFD overexpression in wildtype animals. Do dendrites become longer overall or is there a homeostatic effect as well? Do animals perform better in long-term memory task?

Basic Physiological Properties of Single Cells. For this study, the action potential firing threshold was investigated as an indicator of the general excitability of the VEGFD downregulated neurons. However, the excitability needs further study by the analysis and measurement of more parameters. Additionally, the regulation of I_h through HCN channels in the distal apical dendrites after VEGFD knockdown could be investigated by recording directly the dendrites. The performance of immunostainings of the HCN 1 and 2 channels could reveal further insights on the channel distribution.

GABAergic inputs contribute to the formation of cell assemblies by regulating the excitatory input to pyramidal cells, control the firing rate of pyramidal cells and modulate their spike timing (Klausberger 2009). Thus, recordings of the contribution of local interneurons and their distinct GABAergic input on different dendritic compartments would be of great importance. Interneurons may change their excitability due to morphological changes of CA1 pyramidal cells in order to keep the network synchronized.

Long-Term Memory Deficit. Mauceri et al. (2011) demonstrated a memory deficit in VEGFD knockdown mice in hippocampus depended memory tasks, like the Morris water maze and a fear-conditioning task. However, our recordings revealed no difference in hippocampal network oscillations in VEGFD knockdown mice. Thus, further investigations are needed in order to conclude on mechanisms underlying long-term memory deficits. The use of principle or independent component analysis methods could help to reveal basic differences of theta oscillations between animals. Additionally, since the hippocampus is crucial for processing short-term memory into long-term memory, it would be interesting to record SPW-R complexes not only in the hippocampus but also in the associated cortex areas and then compare the SPW-R between the two areas. Another approach would be to compare SPW-R during awake immobility periods and slow wave sleep periods, while the mouse is learning a specific task e.g. on a linear track or in an M-maze.

In conclusion, the morphology of dendrites has a high impact on the electrical properties and connectivity of neurons, thereby determining signal transmission and integration. It is important to establish a cellular structure-function relationship in order to investigate cognitive functions and dysfunctions. The maintenance of neuronal structural integrity is of great importance, taking into account the close relationship between the alteration of structure, single neuron excitability and network functions in several diseases. It was demonstrated that basal and apical dendritic length of CA1 pyramidal cells is modulated by the growth factor VEGFD and that basic network properties remain intact even after VEGFD knockdown. The general stability of the size of the dendritic tree and the unaltered electrical signatures suggest a homeostatic mechanism, emphasizing the importance of stabilization of the adult mouse hippocampal network even after alterations.

Acknowledgements

I want to express my gratitude to Prof. Dr. Andreas Draguhn for his advice and support during my time in his lab. His broad knowledge and expertise enabled me to conduct my research, while allowing the room for individual development. He gave me the opportunity to learn and apply a broad range of techniques and I acknowledge his support when I participated as a supervisor in the DAAD-RISE program.

I would like to express my gratitude to my second supervisor Prof. Dr. Hilmar Bading for his support and fruitful discussions. Thank you for providing the viruses and vectors and for opening the doors to your lab for me. I always enjoyed the time there.

I want to thank Prof. Dr. Stephan Frings and Prof. Dr. Daniela Mauceri as my defense committee members.

A special thank you goes to Prof. Dr. Daniela Mauceri. I enjoyed the collaboration with you very much. Thank you for your fruitful feedbacks and constructive discussions and for your help with several experiments, e.g. the qPCR, the introduction to confocal microscopy and virus production. Thanks for providing the viruses and vectors for me!

I would like to thank Dr. Martin Both who was my daily supervisor in the lab. Especially, I would like to thank him for his great support with the *in vivo* analysis towards the end of my PhD.

I want to thank the excellence cluster “Cell networks” for the funding of this project and the IZN graduate school for the support throughout my PhD time and for opening the doors to a cooperative and enriching scientific community.

I would like to thank the committee of the DAAD-RISE program for giving me the opportunity to participate in this great program through which I gained a lot experience. Thanks to Ronan McCabe whom I had the honor to supervise and work together.

I wish to thank the committee of the SFB 1134 for awarding and supporting the junior research project called “secret nose project” of Federica Genovese, Antonio Yanez, Martin Kaiser and me. Thanks to Anna Huber who was a great Master student within this project. Thanks to Fede, Antonio and Martin for the great time. I enjoyed the work and fun we had together within this project.

I would like to thank Dr. Eckehard Freitag for teaching me stereotactic injections and fruitful discussions and Dr. Weiping Zhang for help with virus production.

I thank Dr. Ismini Papageorgiou for the introduction to and help with stereology. Further, I would like to thank Justus Schneider for his constant interest and enthusiasm in my project and my wellbeing.

A special thanks goes to Nadine Zuber and Katja Lankisch for their great daily support in the lab. I would like to thank Nadine for her support with the stainings and Katja for her help with the *in vivo* slice preparations. They were always there when I needed them and I appreciated a lot to work with you! Further, I want to thank Lee Embray for his great technical support with broken head stages, amplifiers and more. Thanks to Christian and Federica for commenting on the manuscript.

I would like to thank Susanne Bechtel for her daily support in all administrative issues and beyond.

I had the honor to supervise some students over the years and I always enjoyed it very much and learned a lot from the work with all of them. I would like to emphasize Sonja Krausert, Ronan McCabe, Anna Huber and Lalita Srisawang. It was a pleasure to work with you.

A thank you goes to the current and former lab members of the Draguhn lab for creating such a friendly and welcoming atmosphere. Specially, I would like to thank Antonio for doing this crazy PhD trip from the beginning to the end together. Life is indeed beautiful! Thanks to Azra, Christian, Fabian, Martin K., Jan-Oli, Valandis, Weiwei, Vivan, Greg, André, and all others for the outstanding time.

A special thanks goes to Federica for her friendship, the support and the running times together.

Last, but not least, I would like to thank my family and friends. I owe my deepest gratitude my mum, dad and brother for their constant support. A thank you goes to my aunt and uncle Sigi and Wolle for providing me with many books, especially “Siddhartha”. I want to thank all my dear friends who are spread all over the world, the “Würzburg-friends” and friends from home whom I had the honor to meet and share many memories with. Finally, thank you, Micha that I can rely on you and for all the adventures, we experienced together.

References

Allen, Kevin, J. Nick P. Rawlins, David M. Bannerman, and Jozsef Csicsvari. 2012. “Hippocampal Place Cells Can Encode Multiple Trial-Dependent Features through Rate Remapping.” *Journal of Neuroscience* 32 (42). http://www.jneurosci.org/content/32/42/14752.long.

Alsina, Fernando Cruz, Francisco Javier Hita, Paula Aldana Fontanet, Dolores Irala, Håkan Hedman, Fernanda Ledda, and Gustavo Paratcha. 2016. “Lrig1 Is a Cell-intrinsic Modulator of Hippocampal Dendrite Complexity and BDNF Signaling.” *EMBO Reports* 17 (4): 601–16. doi:10.15252/embr.201541218.

Andersen, Per. 2007. *The Hippocampus Book*. Oxford University Press.

Arikkath, Jyothi. 2012. “Molecular Mechanisms of Dendrite Morphogenesis.” *Frontiers in Cellular Neuroscience* 6. Frontiers: 61. doi:10.3389/fncel.2012.00061.

Bading, H., M. M. Segal, N. J. Sucher, H. Dudek, S. A. Lipton, and M. E. Greenberg. 1995. “N-Methyl-D-Aspartate Receptors Are Critical for Mediating the Effects of Glutamate on Intracellular Calcium Concentration and Immediate Early Gene Expression in Cultured Hippocampal Neurons.” *Neuroscience* 64 (3). Pergamon: 653–64. doi:10.1016/0306-4522(94)00462-E.

Bading, H, D D Ginty, and M E Greenberg. 1993. “Regulation of Gene Expression in Hippocampal Neurons by Distinct Calcium Signaling Pathways.” *Science (New York, N.Y.)* 260 (5105): 181–86. http://www.ncbi.nlm.nih.gov/pubmed/8097060.

Banding, Hilmar, David Ginty, and Michael Greenberg. 2013. “Regulation of Gene Expression in Hippocampal Neurons by Distinct Calcium Signaling Pathways.” *Journal of Chemical Information and Modeling* 53 (9): 1689–99. doi:10.1017/CBO9781107415324.004.

Bean, Bruce P. 2007. “The Action Potential in Mammalian Central Neurons.” *Nature Reviews Neuroscience* 8 (6): 451–65. doi:10.1038/nrn2148.

Beck, Heinz, and Yoel Yaari. 2008. “Plasticity of Intrinsic Neuronal Properties in CNS Disorders.” *Nature Reviews Neuroscience* 9 (5): 357–69. doi:10.1038/nrn2371.

Belluscio, M. A., K. Mizuseki, R. Schmidt, R. Kempter, and G. Buzsaki. 2012. “Cross-Frequency Phase-Phase Coupling between Theta and Gamma Oscillations in the Hippocampus.” *Journal of Neuroscience* 32 (2): 423–35. doi:10.1523/JNEUROSCI.4122-11.2012.

Bengtson, C. Peter, and Hilmar Bading. 2012. “Nuclear Calcium Signaling.” In *Advances in Experimental Medicine and Biology*, 970:377–405. doi:10.1007/978-3-7091-0932-8_17.

Bhuiyan, M.I.H., J.-C. Kim, S.-N. Hwang, M.-Y. Lee, and S.Y. Kim. 2015. “Ischemic

Tolerance Is Associated with VEGF-C and VEGFR-3 Signaling in the Mouse Hippocampus." *Neuroscience* 290: 90–102. doi:10.1016/j.neuroscience.2015.01.025.

Bloodgood, Brenda L, and Bernardo L Sabatini. 2007. "Ca2+ Signaling in Dendritic Spines." *Current Opinion in Neurobiology* 17 (3): 345–51. doi:10.1016/j.conb.2007.04.003.

Bourne, Jennifer, and Kristen M Harris. 2007. "Do Thin Spines Learn to Be Mushroom Spines That Remember?" *Current Opinion in Neurobiology* 17 (3): 381–86. doi:10.1016/j.conb.2007.04.009.

Bourne, Jennifer N, and Kristen M Harris. 2008. "Balancing Structure and Function at Hippocampal Dendritic Spines." *Annual Review of Neuroscience* 31 (1): 47–67. doi:10.1146/annurev.neuro.31.060407.125646.

Bragin, a, G Jandó, Z Nádasdy, J Hetke, K Wise, and G Buzsáki. 1995. "Gamma (40-100 Hz) Oscillation in the Hippocampus of the Behaving Rat." *The Journal of Neuroscience⊠: The Official Journal of the Society for Neuroscience* 15 (1 Pt 1): 47–60. http://www.jneurosci.org/content/15/1/47.long.

Branco, Tiago, and Michael Häusser. 2011. "Synaptic Integration Gradients in Single Cortical Pyramidal Cell Dendrites." *Neuron* 69 (5): 885–92. doi:10.1016/j.neuron.2011.02.006.

Brankack, J, M Stewart, and S E Fox. 1993. "Current Source Density Analysis of the Hippocampal Theta Rhythm: Associated Sustained Potentials and Candidate Synaptic Generators." *Brain Research* 615 (2): 310–27. http://www.ncbi.nlm.nih.gov/pubmed/8364740.

Brankack, Jurij, Valeriy I Kukushka, Alexei L Vyssotski, and Andreas Draguhn. 2010. "EEG Gamma Frequency and Sleep-Wake Scoring in Mice: Comparing Two Types of Supervised Classifiers." *Brain Research* 1322 (March): 59–71. doi:10.1016/j.brainres.2010.01.069.

Bressler, Steven L, and Walter J Freeman. 1980. "Frequency Analysis of Olfactory System EEG in Cat, Rabbit, and Rat." *Electroencephalography and Clinical Neurophysiology* 50 (1–2): 19–24. doi:10.1016/0013-4694(80)90319-3.

Buzsaki, G. 2002. "Homeostatic Maintenance of Neuronal Excitability by Burst Discharges In Vivo." *Cerebral Cortex* 12 (9): 893–99. doi:10.1093/cercor/12.9.893.

Buzsáki, G. 1989. "Two-Stage Model of Memory Trace Formation: A Role for 'noisy' Brain States." *Neuroscience* 31 (3): 551–70. doi:10.1016/0306-4522(89)90423-5.

Buzsáki, G., D.L. Buhl, K.D. Harris, J. Csicsvari, B. Czéh, and A. Morozov. 2003. "Hippocampal Network Patterns of Activity in the Mouse." *Neuroscience* 116 (1): 201–11. doi:10.1016/S0306-4522(02)00669-3.

Buzsáki, G., J. Czopf, I. Kondákor, and L. Kellényi. 1986. "Laminar Distribution of Hippocampal Rhythmic Slow Activity (RSA) in the Behaving Rat: Current-Source

Density Analysis, Effects of Urethane and Atropine." *Brain Research* 365 (1): 125–37. doi:10.1016/0006-8993(86)90729-8.

Buzsaki, G, and A Draguhn. 2004. "Neuronal Oscillations in Cortical Networks." *Science* 304 (5679): 1926–29. doi:10.1126/science.1099745.

Buzsáki, G, Z Horváth, R Urioste, J Hetke, and K Wise. 1992. "High-Frequency Network Oscillation in the Hippocampus." *Science (New York, N.Y.)* 256 (5059): 1025–27. http://www.ncbi.nlm.nih.gov/pubmed/1589772.

Buzsáki, György. 1986. "Hippocampal Sharp Waves: Their Origin and Significance." *Brain Research* 398 (2): 242–52. doi:10.1016/0006-8993(86)91483-6.

Buzsáki, György. 2002. "Theta Oscillations in the Hippocampus." *Neuron* 33 (3): 325–40. doi:10.1016/S0896-6273(02)00586-X.

Buzsáki, György. 2015. "Hippocampal Sharp Wave-Ripple: A Cognitive Biomarker for Episodic Memory and Planning." *Hippocampus* 25 (10): 1073–1188. doi:10.1002/hipo.22488.

Buzsáki, György, Leung Lai-Wo S., and Cornelius H. Vanderwolf. 1983a. "Cellular Bases of Hippocampal EEG in the Behaving Rat." *Brain Research Reviews* 6 (2): 139–71. doi:10.1016/0165-0173(83)90037-1.

Buzsáki, György, Leung Lai-Wo S., and Cornelius H. Vanderwolf. 1983b. "Cellular Bases of Hippocampal EEG in the Behaving Rat." *Brain Research Reviews* 6 (2): 139–71. doi:10.1016/0165-0173(83)90037-1.

Buzsáki, György, and Edvard I Moser. 2013. "Memory, Navigation and Theta Rhythm in the Hippocampal-Entorhinal System." *Nature Neuroscience* 16 (2): 130–38. doi:10.1038/nn.3304.

Buzsáki, György, and Xiao-Jing Wang. 2012. "Mechanisms of Gamma Oscillations." *Annual Review of Neuroscience* 35 (1): 203–25. doi:10.1146/annurev-neuro-062111-150444.

Cameron, Heather A., and Ronald D G Mckay. 2001. "Adult Neurogenesis Produces a Large Pool of New Granule Cells in the Dentate Gyrus." *Journal of Comparative Neurology* 435 (4). John Wiley & Sons, Inc.: 406–17. doi:10.1002/cne.1040.

Cenquizca, Lee A, and Larry W Swanson. 2007. "Spatial Organization of Direct Hippocampal Field CA1 Axonal Projections to the Rest of the Cerebral Cortex." *Brain Research Reviews* 56 (1). NIH Public Access: 1–26. doi:10.1016/j.brainresrev.2007.05.002.

Colgan, Lesley A., and Ryohei Yasuda. 2014. "Plasticity of Dendritic Spines: Subcompartmentalization of Signaling." *Annual Review of Physiology* 76 (1): 365–85. doi:10.1146/annurev-physiol-021113-170400.

Colgin, Laura Lee, Tobias Denninger, Marianne Fyhn, Torkel Hafting, Tora Bonnevie, Ole Jensen, May-Britt Moser, and Edvard I Moser. 2009. "Frequency of Gamma

Oscillations Routes Flow of Information in the Hippocampus." *Nature* 462 (7271): 353–57. doi:10.1038/nature08573.

Csicsvari, Jozsef, Hajime Hirase, András Czurkó, Akira Mamiya, and György Buzsáki. 1999. "Oscillatory Coupling of Hippocampal Pyramidal Cells and Interneurons in the Behaving Rat." *Journal of Neuroscience* 19 (1). http://www.jneurosci.org/content/19/1/274.short.

Csicsvari, Jozsef, Hajime Hirase, Akira Mamiya, and György Buzsáki. 2000. "Ensemble Patterns of Hippocampal CA3-CA1 Neurons during Sharp Wave–Associated Population Events." *Neuron* 28 (2): 585–94. doi:10.1016/S0896-6273(00)00135-5.

Csicsvari, Jozsef, Brian Jamieson, Kensall D. Wise, and György Buzsáki. 2003a. "Mechanisms of Gamma Oscillations in the Hippocampus of the Behaving Rat." *Neuron* 37 (2): 311–22. doi:10.1016/S0896-6273(02)01169-8.

Csicsvari, Jozsef, Brian Jamieson, Kensall D Wise, and György Buzsáki. 2003b. "Mechanisms of Gamma Oscillations in the Hippocampus of the Behaving Rat." *Neuron* 37 (2): 311–22. http://www.ncbi.nlm.nih.gov/pubmed/12546825.

de Anda, Froylan Calderon, Giulia Pollarolo, Jorge Santos Da Silva, Paola G. Camoletto, Fabian Feiguin, and Carlos G. Dotti. 2005. "Centrosome Localization Determines Neuronal Polarity." *Nature* 436 (7051): 704–8. doi:10.1038/nature03811.

Doller, H J, and F F Weight. 1982. "Perforant Pathway Activation of Hippocampal CA1 Stratum Pyramidale Neurons: Electrophysiological Evidence for a Direct Pathway." *Brain Research* 237 (1): 1–13. http://www.ncbi.nlm.nih.gov/pubmed/7074352.

Dragoi, George. 2013. "Internal Operations in the Hippocampus: Single Cell and Ensemble Temporal Coding." *Frontiers in Systems Neuroscience* 7. Frontiers: 46. doi:10.3389/fnsys.2013.00046.

Dzirasa, Kafui, Romulo Fuentes, Sunil Kumar, Juan M Potes, and Miguel A L Nicolelis. 2011. "Chronic in Vivo Multi-Circuit Neurophysiological Recordings in Mice." *Journal of Neuroscience Methods* 195 (1). NIH Public Access: 36–46. doi:10.1016/j.jneumeth.2010.11.014.

English, Daniel F., Adrien Peyrache, Eran Stark, Lisa Roux, Daniela Vallentin, Michael A. Long, and György Buzsáki. 2014. "Excitation and Inhibition Compete to Control Spiking during Hippocampal Ripples: Intracellular Study in Behaving Mice." *Journal of Neuroscience* 34 (49). http://www.jneurosci.org/content/34/49/16509.short.

Fortin, Dale A., Taasin Srivastava, and Thomas R. Soderling. 2012. "Structural Modulation of Dendritic Spines during Synaptic Plasticity." *The Neuroscientist* 18 (4). SAGE PublicationsSage CA: Los Angeles, CA: 326–41. doi:10.1177/1073858411407206.

Fuhrmann, Falko, Daniel Justus, Liudmila Sosulina, Hiroshi Kaneko, Tatjana Beutel, Detlef Friedrichs, Susanne Schoch, Martin Karl Schwarz, Martin Fuhrmann, and Stefan Remy. 2015. “Locomotion, Theta Oscillations, and the Speed-Correlated Firing of Hippocampal Neurons Are Controlled by a Medial Septal Glutamatergic Circuit.” *Neuron* 86 (5): 1253–64. doi:10.1016/j.neuron.2015.05.001.

Girardeau, Gabrielle, and Michaël Zugaro. 2011. “Hippocampal Ripples and Memory Consolidation.” *Current Opinion in Neurobiology* 21 (3): 452–59. doi:10.1016/j.conb.2011.02.005.

Golowasch, Jorge, Gladis Thomas, Adam L. Taylor, Arif Patel, Arlene Pineda, Christopher Khalil, and Farzan Nadim. 2009. “Membrane Capacitance Measurements Revisited: Dependence of Capacitance Value on Measurement Method in Nonisopotential Neurons.” *Journal of Neurophysiology* 102 (4). http://jn.physiology.org/content/102/4/2161.

Hafting, Torkel, Marianne Fyhn, Sturla Molden, May-Britt Moser, and Edvard I. Moser. 2005. “Microstructure of a Spatial Map in the Entorhinal Cortex.” *Nature* 436 (7052): 801–6. doi:10.1038/nature03721.

Hagenston, A. M., and H. Bading. 2011. “Calcium Signaling in Synapse-to-Nucleus Communication.” *Cold Spring Harbor Perspectives in Biology* 3 (11): a004564–a004564. doi:10.1101/cshperspect.a004564.

Hardingham, G E, F J Arnold, and H Bading. 2001. “Nuclear Calcium Signaling Controls CREB-Mediated Gene Expression Triggered by Synaptic Activity.” *Nature Neuroscience* 4 (3): 261–67. doi:10.1038/85109.

Harris, K M, and J K Stevens. 1989. “Dendritic Spines of CA 1 Pyramidal Cells in the Rat Hippocampus: Serial Electron Microscopy with Reference to Their Biophysical Characteristics.” *The Journal of Neuroscience⊠: The Official Journal of the Society for Neuroscience* 9 (8): 2982–97. http://www.ncbi.nlm.nih.gov/pubmed/2769375.

Hasselmo, Michael E. 2005. “What Is the Function of Hippocampal Theta rhythm?—Linking Behavioral Data to Phasic Properties of Field Potential and Unit Recording Data.” *Hippocampus* 15 (7): 936–49. doi:10.1002/hipo.20116.

Häusser, M, N Spruston, and G J Stuart. 2000. “Diversity and Dynamics of Dendritic Signaling.” *Science (New York, N.Y.)* 290 (5492): 739–44. http://www.ncbi.nlm.nih.gov/pubmed/11052929.

Hemstedt, Thekla J, C. Peter Bengtson, Omar Ram?rez, Ana MM Oliveira, and Hilmar Bading. 2017. “Reciprocal Interaction of Dendrite Geometry and Nuclear Calcium-VEGFD Signaling Gates Memory Consolidation and Extinction.” *The Journal of Neuroscience*, June, 2345–16. doi:10.1523/JNEUROSCI.2345-16.2017.

Henze, D A, and G Buzsáki. 2001. “Action Potential Threshold of Hippocampal Pyramidal Cells in Vivo Is Increased by Recent Spiking Activity.” *Neuroscience* 105 (1): 121–30. http://www.ncbi.nlm.nih.gov/pubmed/11483306.

Herreras, O., J. Makarova, and V.A. Makarov. 2015. “New Uses of LFPs: Pathway-Specific Threads Obtained through Spatial Discrimination.” *Neuroscience* 310: 486–503. doi:10.1016/j.neuroscience.2015.09.054.

Hickmott, Peter W., and Iryna M. Ethell. 2006. “Dendritic Plasticity in the Adult Neocortex.” *The Neuroscientist* 12 (1). Sage PublicationsSage CA: Thousand Oaks, CA: 16–28. doi:10.1177/1073858405282417.

Hoffman, D A, and D Johnston. 1998. “Downregulation of Transient K+ Channels in Dendrites of Hippocampal CA1 Pyramidal Neurons by Activation of PKA and PKC.” *The Journal of Neuroscience⊠: The Official Journal of the Society for Neuroscience* 18 (10): 3521–28. http://www.ncbi.nlm.nih.gov/pubmed/9570783.

Holsheimer, J. 1987. “Electrical Conductivity of the Hippocampal CA1 Layers and Application to Current-Source-Density Analysis.” *Experimental Brain Research* 67 (2): 402–10. http://www.ncbi.nlm.nih.gov/pubmed/3622698.

Horton, April C, and Michael D Ehlers. 2003. “Dual Modes of Endoplasmic Reticulum-to-Golgi Transport in Dendrites Revealed by Live-Cell Imaging.” *The Journal of Neuroscience⊠: The Official Journal of the Society for Neuroscience* 23 (15): 6188–99. http://www.ncbi.nlm.nih.gov/pubmed/12867502.

Hutcheon, Bruce, and Yosef Yarom. 2000. “Resonance, Oscillation and the Intrinsic Frequency Preferences of Neurons.” *Trends in Neurosciences* 23 (5): 216–22. doi:10.1016/S0166-2236(00)01547-2.

Jadhav, Shantanu P., Caleb Kemere, P. Walter German, and Loren M. Frank. 2012. “Awake Hippocampal Sharp-Wave Ripples Support Spatial Memory.” *Science* 336 (6087). http://science.sciencemag.org/content/336/6087/1454.full.

Jensen, O, and J E Lisman. 2000. “Position Reconstruction from an Ensemble of Hippocampal Place Cells: Contribution of Theta Phase Coding.” *Journal of Neurophysiology* 83 (5): 2602–9. http://www.ncbi.nlm.nih.gov/pubmed/10805660.

Jensen, Ole, and Laura L. Colgin. 2007. “Cross-Frequency Coupling between Neuronal Oscillations.” *Trends in Cognitive Sciences* 11 (7): 267–69. doi:10.1016/j.tics.2007.05.003.

Jensen, Ole, Jochen Kaiser, and Jean-Philippe Lachaux. 2007. “Human Gamma-Frequency Oscillations Associated with Attention and Memory.” *Trends in Neurosciences* 30 (7): 317–24. doi:10.1016/j.tins.2007.05.001.

Johnston, D, J C Magee, C M Colbert, and B R Cristie. 1996. “Active Properties of Neuronal Dendrites.” *Annual Review of Neuroscience* 19 (1): 165–86. doi:10.1146/annurev.ne.19.030196.001121.

Jouvet, M. 1969. “Biogenic Amines and the States of Sleep.” *Science (New York, N.Y.)* 163 (3862): 32–41. http://www.ncbi.nlm.nih.gov/pubmed/4303225.

Jung, S., T. D. Jones, J. N. Lugo, A. H. Sheerin, J. W. Miller, R. D’Ambrosio, A. E.

Anderson, and N. P. Poolos. 2007. “Progressive Dendritic HCN Channelopathy during Epileptogenesis in the Rat Pilocarpine Model of Epilepsy.” *Journal of Neuroscience* 27 (47): 13012–21. doi:10.1523/JNEUROSCI.3605-07.2007.

Klausberger, Thomas. 2009. “GABAergic Interneurons Targeting Dendrites of Pyramidal Cells in the CA1 Area of the Hippocampus.” *The European Journal of Neuroscience* 30 (6): 947–57. doi:10.1111/j.1460-9568.2009.06913.x.

Klugmann, Matthias, C. Wymond Symes, Claudia B. Leichtlein, Bettina K. Klaussner, Jane Dunning, Dahna Fong, Deborah Young, and Matthew J. During. 2005. “AAV-Mediated Hippocampal Expression of Short and Long Homer 1 Proteins Differentially Affect Cognition and Seizure Activity in Adult Rats.” *Molecular and Cellular Neuroscience* 28 (2): 347–60. doi:10.1016/j.mcn.2004.10.002.

Kohara, Keigo, Michele Pignatelli, Alexander J Rivest, Hae-Yoon Jung, Takashi Kitamura, Junghyup Suh, Dominic Frank, et al. 2014. “Cell Type-Specific Genetic and Optogenetic Tools Reveal Hippocampal CA2 Circuits.” *Nature Neuroscience* 17 (2): 269–79. doi:10.1038/nn.3614.

Koleske, Anthony J. 2013. “Molecular Mechanisms of Dendrite Stability.” *Nature Reviews Neuroscience* 14 (8): 536–50. doi:10.1038/nrn3486.

Kramis, R., C.H. Vanderwolf, and B.H. Bland. 1975. “Two Types of Hippocampal Rhythmical Slow Activity in Both the Rabbit and the Rat: Relations to Behavior and Effects of Atropine, Diethyl Ether, Urethane, and Pentobarbital.” *Experimental Neurology* 49 (1): 58–85. doi:10.1016/0014-4886(75)90195-8.

Kupferman, Justine V, Jayeeta Basu, Marco J Russo, Jenieve Guevarra, Stephanie K Cheung, and Steven A Siegelbaum. 2014. “Reelin Signaling Specifies the Molecular Identity of the Pyramidal Neuron Distal Dendritic Compartment.” *Cell* 158 (6): 1335–47. doi:10.1016/j.cell.2014.07.035.

Larkum, Matthew. 2013. “A Cellular Mechanism for Cortical Associations: An Organizing Principle for the Cerebral Cortex.” *Trends in Neurosciences* 36 (3): 141–51. doi:10.1016/j.tins.2012.11.006.

Lasztóczi, Bálint, and Thomas Klausberger. 2016. “Hippocampal Place Cells Couple to Three Different Gamma Oscillations during Place Field Traversal.” *Neuron.* Vol. 91. doi:10.1016/j.neuron.2016.05.036.

Lau, David, and Hilmar Bading. 2009. “Synaptic Activity-Mediated Suppression of p53 and Induction of Nuclear Calcium-Regulated Neuroprotective Genes Promote Survival through Inhibition of Mitochondrial Permeability Transition.” *The Journal of Neuroscience☒: The Official Journal of the Society for Neuroscience* 29 (14): 4420–29. doi:10.1523/JNEUROSCI.0802-09.2009.

Leão, Richardson N, Sanja Mikulovic, Katarina E Leão, Hermany Munguba, Henrik Gezelius, Anders Enjin, Kalicharan Patra, et al. 2012. “OLM Interneurons Differentially Modulate CA3 and Entorhinal Inputs to Hippocampal CA1

Neurons." *Nature Neuroscience* 15 (11): 1524–30. doi:10.1038/nn.3235.

Leung, L W. 1984. "Model of Gradual Phase Shift of Theta Rhythm in the Rat." *Journal of Neurophysiology* 52 (6): 1051–65. http://www.ncbi.nlm.nih.gov/pubmed/6097652.

Lisman, J E, and M A Idiart. 1995. "Storage of 7 +/- 2 Short-Term Memories in Oscillatory Subcycles." *Science (New York, N.Y.)* 267 (5203): 1512–15. http://www.ncbi.nlm.nih.gov/pubmed/7878473.

Lisman, John. 2005. "The Theta/gamma Discrete Phase Code Occuring during the Hippocampal Phase Precession May Be a More General Brain Coding Scheme." *Hippocampus* 15 (7): 913–22. doi:10.1002/hipo.20121.

Lisman, John. 2015. "The Challenge of Understanding the Brain: Where We Stand in 2015." *Neuron* 86 (4): 864–82. doi:10.1016/j.neuron.2015.03.032.

Lohela, Marja, Maija Bry, Tuomas Tammela, and Kari Alitalo. 2009. "VEGFs and Receptors Involved in Angiogenesis versus Lymphangiogenesis." *Current Opinion in Cell Biology* 21 (2): 154–65. doi:10.1016/j.ceb.2008.12.012.

Lorente de Nó, R. 1934. "Observations on Nystagmus." *Acta Oto-Laryngologica* 21 (4): 416–37. doi:10.3109/00016483409119278.

Lörincz, Andrea, Takuya Notomi, Gábor Tamás, Ryuichi Shigemoto, and Zoltan Nusser. 2002. "Polarized and Compartment-Dependent Distribution of HCN1 in Pyramidal Cell Dendrites." *Nature Neuroscience* 5 (11): 1185–93. doi:10.1038/nn962.

Magee, J C. 1998. "Dendritic Hyperpolarization-Activated Currents Modify the Integrative Properties of Hippocampal CA1 Pyramidal Neurons." *The Journal of Neuroscience⊠: The Official Journal of the Society for Neuroscience* 18 (19): 7613–24. http://www.ncbi.nlm.nih.gov/pubmed/9742133.

Makarova, Julia, Jose M Ibarz, Valeri A Makarov, Nuria Benito, and Oscar Herreras. 2011. "Parallel Readout of Pathway-Specific Inputs to Laminated Brain Structures." *Frontiers in Systems Neuroscience* 5. Frontiers: 77. doi:10.3389/fnsys.2011.00077.

Marx, Manuel, Robert H Günter, Werner Hucko, Gabriele Radnikow, and Dirk Feldmeyer. 2012. "Improved Biocytin Labeling and Neuronal 3D Reconstruction." *Nature Protocols* 7 (2). Nature Publishing Group, a division of Macmillan Publishers Limited. All Rights Reserved.: 394–407. doi:10.1038/nprot.2011.449.

Matsuki, Tohru, Russell T Matthews, Jonathan A Cooper, Marcel P van der Brug, Mark R Cookson, John A Hardy, Eric C Olson, and Brian W Howell. 2010. "Reelin and stk25 Have Opposing Roles in Neuronal Polarization and Dendritic Golgi Deployment." *Cell* 143 (5): 826–36. doi:10.1016/j.cell.2010.10.029.

Mauceri, D, H E Freitag, A M Oliveira, C P Bengtson, and H Bading. 2011. "Nuclear

Calcium-VEGFD Signaling Controls Maintenance of Dendrite Arborization Necessary for Memory Formation." *Neuron* 71 (1): 117–30. doi:10.1016/j.neuron.2011.04.022.

Mauceri, Daniela, Anna M. Hagenston, Kathrin Schramm, Ursula Weiss, and Hilmar Bading. 2015. "Nuclear Calcium Buffering Capacity Shapes Neuronal Architecture." *Journal of Biological Chemistry* 290 (38): 23039–49. doi:10.1074/jbc.M115.654962.

Miltner, W H, C Braun, M Arnold, H Witte, and E Taub. 1999. "Coherence of Gamma-Band EEG Activity as a Basis for Associative Learning." *Nature* 397 (6718): 434–36. doi:10.1038/17126.

Montgomery, Sean M, and György Buzsáki. 2007. "Gamma Oscillations Dynamically Couple Hippocampal CA3 and CA1 Regions during Memory Task Performance." *Proceedings of the National Academy of Sciences of the United States of America* 104 (36). National Academy of Sciences: 14495–500. doi:10.1073/pnas.0701826104.

Moser, Edvard I., Emilio Kropff, and May-Britt Moser. 2008. "Place Cells, Grid Cells, and the Brain's Spatial Representation System." *Annual Review of Neuroscience* 31 (1). Annual Reviews : 69–89. doi:10.1146/annurev.neuro.31.061307.090723.

Moser, M B, M Trommald, and P Andersen. 1994. "An Increase in Dendritic Spine Density on Hippocampal CA1 Pyramidal Cells Following Spatial Learning in Adult Rats Suggests the Formation of New Synapses." *Proceedings of the National Academy of Sciences of the United States of America* 91 (26). National Academy of Sciences: 12673–75. http://www.ncbi.nlm.nih.gov/pubmed/7809099.

Naber, Pieterke A., Fernando H. Lopes da Silva, and Menno P. Witter. 2001. "Reciprocal Connections between the Entorhinal Cortex and Hippocampal Fields CA1 and the Subiculum Are in Register with the Projections from CA1 to the Subiculum." *Hippocampus* 11 (2): 99–104. doi:10.1002/hipo.1028.

Neves, Guilherme, Sam F. Cooke, and Tim V. P. Bliss. 2008. "Synaptic Plasticity, Memory and the Hippocampus: A Neural Network Approach to Causality." *Nature Reviews Neuroscience* 9 (1). Nature Publishing Group: 65–75. doi:10.1038/nrn2303.

Nicholson, C., and J. A. Freeman. 1975. "Theory of Current Source-Density Analysis and Determination of Conductivity Tensor for Anuran Cerebellum." *Journal of Neurophysiology* 38 (2). http://jn.physiology.org/content/38/2/356.short.

Nicholson, Daniel A., Rachel Trana, Yael Katz, William L. Kath, Nelson Spruston, and Yuri Geinisman. 2006. "Distance-Dependent Differences in Synapse Number and AMPA Receptor Expression in Hippocampal CA1 Pyramidal Neurons." *Neuron* 50 (3): 431–42. doi:10.1016/j.neuron.2006.03.022.

Nolan, Matthew F, Gaël Malleret, Ka Hung Lee, Emma Gibbs, Joshua T Dudman, Bina Santoro, Deqi Yin, et al. 2003. "The Hyperpolarization-Activated HCN1 Channel

Is Important for Motor Learning and Neuronal Integration by Cerebellar Purkinje Cells." *Cell* 115 (5): 551–64. http://www.ncbi.nlm.nih.gov/pubmed/14651847.

O'Keefe, J., and J. Dostrovsky. 1971. "The Hippocampus as a Spatial Map. Preliminary Evidence from Unit Activity in the Freely-Moving Rat." *Brain Research* 34 (1): 171–75. doi:10.1016/0006-8993(71)90358-1.

O'keefe, J, and L Nadel. 1978. "The Hippocampus as a Cognitive Map." http://arizona.openrepository.com/arizona/handle/10150/620894.

O'Keefe, John. 1976. "Place Units in the Hippocampus of the Freely Moving Rat." *Experimental Neurology* 51 (1): 78–109. doi:10.1016/0014-4886(76)90055-8.

O'Keefe, John., and Lynn Nadel. 1978. *The Hippocampus as a Cognitive Map.* Clarendon Press. http://arizona.openrepository.com/arizona/handle/10150/620894.

Orefice, Lauren L., Emily G. Waterhouse, John G. Partridge, Rupa R. Lalchandani, Stefano Vicini, and Baoji Xu. 2013. "Distinct Roles for Somatically and Dendritically Synthesized Brain-Derived Neurotrophic Factor in Morphogenesis of Dendritic Spines." *Journal of Neuroscience* 33 (28). http://www.jneurosci.org/content/33/28/11618.short.

Palop, Jorge J., Jeannie Chin, Erik D. Roberson, Jun Wang, Myo T. Thwin, Nga Bien-Ly, Jong Yoo, et al. 2007. "Aberrant Excitatory Neuronal Activity and Compensatory Remodeling of Inhibitory Hippocampal Circuits in Mouse Models of Alzheimer's Disease." *Neuron* 55 (5): 697–711. doi:10.1016/j.neuron.2007.07.025.

Panico, J, and P Sterling. 1995. "Retinal Neurons and Vessels Are Not Fractal but Space-Filling." *The Journal of Comparative Neurology* 361 (3): 479–90. doi:10.1002/cne.903610311.

Paxinos, George, and Keith B. J. Franklin. 2004. *The Mouse Brain in Stereotaxic Coordinates.* Elsevier Academic Press. https://books.google.de/books?hl=de&lr=&id=EHy1QN1xv0gC&oi=fnd&pg=PR9&dq=Paxinos+G,+Franklin+KBJ+(2001)+The+mouse+brain+in+stereotaxic+coordinates.+San+Diego:+Academic.&ots=8-X-zTCHYm&sig=5VgsFFc3aXO_kdxiazLMvlIpAjA#v=onepage&q&f=false.

Peraza, Luis R., Aziz U.R. Asghar, Gary Green, and David M. Halliday. 2012. "Volume Conduction Effects in Brain Network Inference from Electroencephalographic Recordings Using Phase Lag Index." *Journal of Neuroscience Methods* 207 (2): 189–99. doi:10.1016/j.jneumeth.2012.04.007.

Petsche, H., Ch. Stumpf, and G. Gogolak. 1962. "The Significance of the Rabbit's Septum as a Relay Station between the Midbrain and the Hippocampus I. The Control of Hippocampus Arousal Activity by the Septum Cells." *Electroencephalography and Clinical Neurophysiology* 14 (2): 202–11. doi:10.1016/0013-4694(62)90030-5.

Ramón y Cajal, S. 1911. "Histologie Du Systeme Nerveux de L'homme et Des Vertebres." *Maloine (Paris)* 2: 891–942. http://ci.nii.ac.jp/naid/10011413022/.

Rolls, Edmund T. 2010. "A Computational Theory of Episodic Memory Formation in the Hippocampus." *Behavioural Brain Research* 215 (2): 180–96. doi:10.1016/j.bbr.2010.03.027.

Rolls, Edmund T. 2016. "Pattern Separation, Completion, and Categorisation in the Hippocampus and Neocortex." *Neurobiology of Learning and Memory* 129 (March): 4–28. doi:10.1016/j.nlm.2015.07.008.

Samsonovich, Alexei V, and Giorgio A Ascoli. 2006. "Morphological Homeostasis in Cortical Dendrites." *Proceedings of the National Academy of Sciences of the United States of America* 103 (5). National Academy of Sciences: 1569–74. doi:10.1073/pnas.0510057103.

Scheff, Stephen W., Douglas A. Price, Frederick A. Schmitt, and Elliott J. Mufson. 2006. "Hippocampal Synaptic Loss in Early Alzheimer's Disease and Mild Cognitive Impairment." *Neurobiology of Aging* 27 (10): 1372–84. doi:10.1016/j.neurobiolaging.2005.09.012.

Scheffer-Teixeira, Robson, Hindiael Belchior, Fábio V. Caixeta, Bryan C. Souza, Sidarta Ribeiro, and Adriano B. L. Tort. 2012. "Theta Phase Modulates Multiple Layer-Specific Oscillations in the CA1 Region." *Cerebral Cortex* 22 (10). Oxford University Press: 2404–14. doi:10.1093/cercor/bhr319.

Schomburg, Erik W, Antonio Fernández-Ruiz, Kenji Mizuseki, Antal Berényi, Costas A Anastassiou, Christof Koch, and György Buzsáki. 2014. "Theta Phase Segregation of Input-Specific Gamma Patterns in Entorhinal-Hippocampal Networks." *Neuron* 84 (2): 470–85. doi:10.1016/j.neuron.2014.08.051.

Schwaller, B. 2009. "The Continuing Disappearance of 'pure' Ca2+ Buffers." *Cellular and Molecular Life Sciences* 66 (2): 275–300. doi:10.1007/s00018-008-8564-6.

Scoville, W. B., and B. Milner. 1957. "Loss of Recent Memory After Bilateral Hippocampal Lesions." *Journal of Neurology, Neurosurgery & Psychiatry* 20 (1): 11–21. doi:10.1136/jnnp.20.1.11.

Shah, Mala M, Anne E Anderson, Victor Leung, Xiaodi Lin, and Daniel Johnston. 2004. "Seizure-Induced Plasticity of H Channels in Entorhinal Cortical Layer III Pyramidal Neurons." *Neuron* 44 (3): 495–508. doi:10.1016/j.neuron.2004.10.011.

Shin, Yoo-Jin, Jeong-Sun Choi, Ji-Yeon Lee, Jae-Youn Choi, Jung-Ho Cha, Myung-Hoon Chun, and Mun-Yong Lee. 2008. "Differential Regulation of Vascular Endothelial Growth Factor-C and Its Receptor in the Rat Hippocampus Following Transient Forebrain Ischemia." *Acta Neuropathologica* 116 (5). Springer-Verlag: 517–27. doi:10.1007/s00401-008-0423-x.

Sholl, D. a. 1953. "Dendritic Organization in the Neurons of the Visual and Motor Cortices of the Cat." *Journal of Anatomy* 87 (Pt 4). Wiley-Blackwell: 387–406.1.

http://www.pubmedcentral.nih.gov/articlerender.fcgi?artid=1244622&tool=pmcentrez&rendertype=abstract.

Simonetti, Manuela, Anna M Hagenston, Daniel Vardeh, H Eckehard Freitag, Daniela Mauceri, Jianning Lu, Venkata P Satagopam, et al. 2013. “Nuclear Calcium Signaling in Spinal Neurons Drives a Genomic Program Required for Persistent Inflammatory Pain.” *Neuron* 77 (1): 43–57. doi:10.1016/j.neuron.2012.10.037.

Sirota, Anton, Sean Montgomery, Shigeyoshi Fujisawa, Yoshikazu Isomura, Michael Zugaro, and György Buzsáki. 2008. “Entrainment of Neocortical Neurons and Gamma Oscillations by the Hippocampal Theta Rhythm.” *Neuron* 60 (4): 683–97. doi:10.1016/j.neuron.2008.09.014.

Šišková, Zuzana, Daniel Justus, Hiroshi Kaneko, Detlef Friedrichs, Niklas Henneberg, Tatjana Beutel, Julika Pitsch, et al. 2014. “Dendritic Structural Degeneration Is Functionally Linked to Cellular Hyperexcitability in a Mouse Model of Alzheimer’s Disease.” *Neuron* 84 (5): 1023–33. doi:10.1016/j.neuron.2014.10.024.

Spruston, Nelson. 2008. “Pyramidal Neurons: Dendritic Structure and Synaptic Integration.” *Nature Reviews. Neuroscience* 9 (3). Nature Publishing Group: 206–21. doi:10.1038/nrn2286.

Squire, Larry R., Neal J. Cohen, and Joyce A. Zouzounis. 1984. “Preserved Memory in Retrograde Amnesia: Sparing of a Recently Acquired Skill.” *Neuropsychologia* 22 (2): 145–52. doi:10.1016/0028-3932(84)90057-5.

Squire, Larry R, Craig E L Stark, and Robert E Clark. 2004. “The Medial Temporal Lobe.” *Annual Review of Neuroscience* 27 (1): 279–306. doi:10.1146/annurev.neuro.27.070203.144130.

Thome, Christian, Tony Kelly, Antonio Yanez, Christian Schultz, Maren Engelhardt, Sidney B Cambridge, Martin Both, Andreas Draguhn, Heinz Beck, and Alexei V Egorov. 2014. “Axon-Carrying Dendrites Convey Privileged Synaptic Input in Hippocampal Neurons.” *Neuron* 83 (6): 1418–30. doi:10.1016/j.neuron.2014.08.013.

Tort, A. B. L., R. W. Komorowski, J. R. Manns, N. J. Kopell, and H. Eichenbaum. 2009. “Theta-Gamma Coupling Increases during the Learning of Item-Context Associations.” *Proceedings of the National Academy of Sciences* 106 (49): 20942–47. doi:10.1073/pnas.0911331106.

Tort, Adriano B. L., Robert Komorowski, Howard Eichenbaum, and Nancy Kopell. 2010. “Measuring Phase-Amplitude Coupling Between Neuronal Oscillations of Different Frequencies.” *Journal of Neurophysiology* 104 (2). http://jn.physiology.org/content/104/2/1195?ijkey=5d9b8a5d784f7fd3fb6467b97229d36162207920&keytype2=tf_ipsecsha.

Tort, Adriano B L, Mark A Kramer, Catherine Thorn, Daniel J Gibson, Yasuo Kubota, Ann M Graybiel, and Nancy J Kopell. 2008. “Dynamic Cross-Frequency Couplings of Local Field Potential Oscillations in Rat Striatum and Hippocampus during

Performance of a T-Maze Task.” *Proceedings of the National Academy of Sciences of the United States of America* 105 (51): 20517–22. doi:10.1073/pnas.0810524105.

Vanderwolf, C H. 1969. “Hippocampal Electrical Activity and Voluntary Movement in the Rat.” *Electroencephalography and Clinical Neurophysiology* 26 (4): 407–18. http://www.ncbi.nlm.nih.gov/pubmed/4183562.

von Bechterew, W V. 1900. “Demonstration Eines Gehirns Mit Zerstörung Der Vorderen Und Innern Theile Der Hirnrinde Beider Schläfenlappen.” *Neurologisches Centralblatt* 19: 990–91. http://ci.nii.ac.jp/naid/10029853398/.

Wang, Xiao-Jing. 2002. “Pacemaker Neurons for the Theta Rhythm and Their Synchronization in the Septohippocampal Reciprocal Loop.” *Journal of Neurophysiology* 87 (2). http://jn.physiology.org/content/87/2/889.short.

White, J A, M I Banks, R A Pearce, and N J Kopell. 2000. “Networks of Interneurons with Fast and Slow Gamma-Aminobutyric Acid Type A (GABAA) Kinetics Provide Substrate for Mixed Gamma-Theta Rhythm.” *Proceedings of the National Academy of Sciences of the United States of America* 97 (14). National Academy of Sciences: 8128–33. doi:10.1073/pnas.100124097.

Williams, Stephen R., and Greg J. Stuart. 2003. “Role of Dendritic Synapse Location in the Control of Action Potential Output.” *Trends in Neurosciences* 26 (3): 147–54. doi:10.1016/S0166-2236(03)00035-3.

Wulff, Peer, Alexey A Ponomarenko, Marlene Bartos, Tatiana M Korotkova, Elke C Fuchs, Florian Bähner, Martin Both, et al. 2009. “Hippocampal Theta Rhythm and Its Coupling with Gamma Oscillations Require Fast Inhibition onto Parvalbumin-Positive Interneurons.” *Proceedings of the National Academy of Sciences of the United States of America* 106 (9). National Academy of Sciences: 3561–66. doi:10.1073/pnas.0813176106.

Ylinen, A, A Bragin, Z Nádasdy, G Jandó, I Szabó, A Sik, and G Buzsáki. 1995. “Sharp Wave-Associated High-Frequency Oscillation (200 Hz) in the Intact Hippocampus: Network and Intracellular Mechanisms.” *The Journal of Neuroscience : The Official Journal of the Society for Neuroscience* 15 (1 Pt 1): 30–46. http://www.ncbi.nlm.nih.gov/pubmed/7823136.

Yu, Wendou, and Bingwei Lu. 2012. “Synapses and Dendritic Spines as Pathogenic Targets in Alzheimer’s Disease.” *Neural Plasticity* 2012: 1–8. doi:10.1155/2012/247150.